

PL-TR-91-2253

AD-A269 976



2

1

**A SIMPLE DOPPLER WIND LIDAR SENSOR: SIMULATED
MEASUREMENTS AND IMPACTS IN A GLOBAL
ASSIMILATION AND FORECAST SYSTEM**

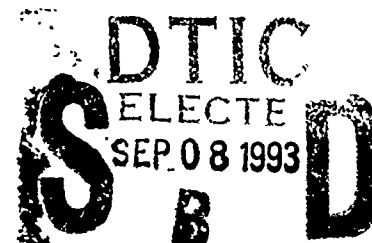
C. Grassotti
R.G. Isaacs
R.N. Hoffman

M. Mickelson
T. Nehr Korn
J.-F. Louis

Atmospheric and Environmental Research, Inc.
840 Memorial Drive
Cambridge, MA 02139

1 October 1991

Scientific Report No. 1



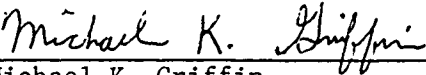
APPROVED FOR PUBLIC RELEASE; DISTRIBUTION UNLIMITED

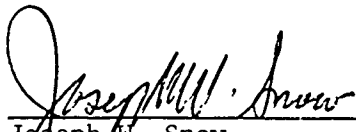
93-20813

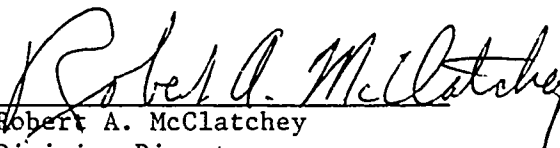


**PHILLIPS LABORATORY
AIR FORCE SYSTEMS COMMAND
HANSCOM AIR FORCE BASE, MASSACHUSETTS 01731-5000**

This technical report has been reviewed and is approved for publication.


Michael K. Griffin
Contract Manager


Joseph W. Snow
Branch Chief


Robert A. McClatchey
Division Director

This document has been reviewed by the ESD Public Affairs Office (PA) and is releasable to the National Technical Information Service (NTIS).

Qualified requestors may obtain additional copies from the Defense Technical Information Center. All others should apply to the National Technical Information Service.

If your address has changed, or if you wish to be removed from the mailing list, or if the addressee is no longer employed by your organization, please notify PL/TSI, Hanscom AFB, MA 01731-5000. This will assist us in maintaining a current mailing list.

Do not return copies of this report unless contractual obligations or notices on a specific document requires that it be returned.

REPORT DOCUMENTATION PAGE		FORM 10-100-100	
REPORT DATE 1 October 1991		REPORT TYPE AND DATES COVERED Scientific Report No. 1	
TITLE A Simple Doppler Wind Lidar Sensor: Simulated Measurements and Impacts in a Global Assimilation and Forecast System		FUNDING NUMBER PE 35160F PR 6670 TA 17 WU AR	
AUTHOR(S) C. Grassotti R.G. Isaacs R.N. Hoffman M. Mickelson T. Nehrkorn J.-F. Louis		CONTRACT NUMBER Contract F19628-89-C-0137	
PERFORMING ORGANIZATION NAME(S) AND ADDRESS(ES) Atmospheric and Environmental Research, Inc. 840 Memorial Drive Cambridge, MA 02139		PERFORMING ORGANIZATION REPORT NUMBER	
SPONSORING AGENCY NAME(S) AND ADDRESS(ES) Phillips Laboratory Hanscom AFB, MA 01731-5000 Contract Manager: Michael Griffin/LYS		SPONSORING MONITORING AGENCY REPORT NUMBER PL-TR-91-2253	
STATEMENT OF WORK Approved for public release; Distribution unlimited		DISTRIBUTION CODE	
<p>We have simulated the wind measurements which might be obtained from a low power doppler wind lidar (DWL) sensor. Wind profiles obtained from such an instrument will not be as complete as those expected from planned higher energy sensors (e.g. LAWS), with measurements only from cirrus cloud, the tops of other clouds, and from marine boundary layer aerosol. The potential impact of such a scaled down DWL system has been assessed by inserting the simulated measurements into the Air Force Geophysics Laboratory (GL)* Global Data Assimilation System (GDAS). Results from the observing system simulation experiment (OSSE) indicate that significant improvement in the analysis and forecast of geopotential height, horizontal wind, and relative humidity may be expected in the southern hemisphere extratropics. Comparison of impacts with those obtained in a previously conducted OSSE which assumed a full blown DWL instrument (WINDSAT) indicate that the low energy lidar yields improvements which are 1/2 to 3/4 the magnitude of improvements with WINDSAT. Thus, if the development cost of a simple lidar is found to be substantially less than a LAWS-type sensor, such an instrument may warrant consideration in the planning of future space-based observing systems.</p> <p>*NOW KNOWN AS PHILLIPS LABORATORY</p>			
SUBJECT TERMS Lidar Doppler lidar Winds		Spaceborne lidar Satellite sensors Meteorological wind assimilation 15 NUMBER OF PAGES 98 16 PRICE CODE	
SECURITY CLASSIFICATION OF THIS PAGE Unclassified		SECURITY CLASSIFICATION OF ABSTRACT Unclassified 20 LIMITATION OF ABSTRACT SAR	

Contents

1	INTRODUCTION	1
2	BACKGROUND	1
3	TECHNICAL APPROACH	4
3.1	Lidar Measurement	4
3.2	Doppler Wind Lidar Sensors	4
3.3	NWP Related Lidar Instrument Characteristics	6
4	OSSE DESIGN	7
4.1	The Nature Run	7
4.2	The Simulated Observing Systems	7
4.3	The 4D Assimilation System	13
4.4	Comparison Methodology	14
5	LIDAR DATA SIMULATION METHODOLOGY	16
5.1	Data Sampling	16
5.2	Cloud and Aerosol Diagnosis	18
5.3	Measurement Error	24
6	IMPACT RESULTS	32
6.1	Synoptic Maps	32
6.2	Analysis and Forecast Error as a Function of Time	51
6.3	Analysis and Forecast Error as a Function of Pressure	59
6.4	Averaged Forecast Errors	70
6.5	Comparison with WINDSAT	80
7	CONCLUSIONS	81
	REFERENCES	85

Accession For	
NTIS GRA&I	<input checked="" type="checkbox"/>
DTIC TAB	<input type="checkbox"/>
Unannounced	<input type="checkbox"/>
Justification	
By	
Distribution/	
Availability Codes	
Dist	Avail and/or Special
A-1	

List of Figures

Figure 1	Distribution of CDW pressures.	10
Figure 2	Horizontal correlations for low level (1000-600 mb) CDWs. Shown are correlations for the background field evaluated at the CDW locations (top), original CDW errors (middle) and filtered CDW errors (bottom) for u (left) and v (right) wind components.	11
Figure 3	Horizontal correlations for high level (600-100 mb) CDWs. Same as Fig. 2.	12
Figure 4	RMS height errors at 500 hPa for STATSAT (solid) and CONTROL (dotted) assimilation experiments.	17
Figure 5	Comparison of cirrus occurrence determined from SAGE data vs. that obtained in current OSSE. SAGE results valid for September, October, November time period. AER results valid for 18 November 1979, 06 UTC.	20
Figure 6	Locations of lidar measurements at 850 mb on 19 November 1979, 12 UTC.	23
Figure 7	Modeled cirrus extinction (km^{-1}) as a function of temperature.	26
Figure 8	Modeled cirrus backscatter ($\text{km}^{-1}\text{sr}^{-1}$) as a function of temperature.	27
Figure 9	Schematic diagram of lidar wind measurement.	29
Figure 10	Error amplification factor in terms of distance to satellite subtrack.	31
Figure 11	Nature 500 hPa geopotential height valid 00 UTC 23 November 1979. (a) Northern hemisphere, (b) Southern hemisphere. Contour interval is 80 m.	33

Figure 12	500 hPa geopotential height analysis valid 00 UTC 23 November 1979. (a),(b) CONTROL analysis and analysis error, (c),(d) LIDAR analysis and analysis error for the northern hemisphere. Corresponding southern hemisphere plots are in (e)-(h), respectively. Contour interval is 80 m for analyses, and 40 m for analysis errors.	34
Figure 13	500 hPa 48 hour geopotential height analysis valid 00 UTC 23 November 1979. (a),(b) CONTROL analysis and analysis error, (c),(d) LIDAR analysis and analysis error for the northern hemisphere. Corresponding southern hemisphere plots are in (e)-(h), respectively. Contour interval is 80 m for analyses, and 40 m for analysis errors.	38
Figure 14	850 hPa global horizontal wind speed analysis and vector wind error magnitude fields valid 00 UTC 23 November 1979. (a),(b) CONTROL analysis and analysis error, (c),(d) LIDAR analysis and analysis error. Corresponding 48 h forecast maps valid at the same time are in (e)-(h). Contour interval is 5 ms^{-1} starting at 10 ms^{-1} for wind speed, and starting at 5 ms^{-1} for the error maps.	43
Figure 15	850 hPa global horizontal wind vector analysis and analysis error valid 00 UTC 23 November 1979. (a),(b) CONTROL analysis and analysis error, (c),(d) LIDAR analysis and analysis error. Corresponding 48 h forecast maps valid at the same time are in (e)-(h).	47
Figure 16	850 hPa global relative humidity analysis error and 48 h forecast error valid 00 UTC 23 November 1979. (a),(b) CONTROL analysis and forecast error, (c),(d) LIDAR analysis error and forecast error. Contour interval is 25 percent with zero line omitted. Negative values are dashed.	52
Figure 17	500 hPa geopotential height analysis and forecast errors averaged horizontally. (a) Global, (b) Northern hemisphere, (c) Tropics, (d) Southern hemisphere. Shown are CONTROL (dot), LIDAR (solid), SATSAT (dash), and WINDSAT (dash-dot-dot-dot).	54

Figure 18	850 hPa u component wind analysis and forecast errors averaged horizontally. (a) Global, (b) Northern hemisphere, (c) Tropics, (d) Southern hemisphere. Shown are CONTROL (dot), LIDAR (solid), STATSAT (dash), and WINDSAT (dash-dot-dot-dot).	57
Figure 19	200 hPa u component wind analysis and forecast errors averaged horizontally. (a) Global, (b) Northern hemisphere, (c) Tropics, (d) Southern hemisphere. Shown are CONTROL (dot), LIDAR (solid), STATSAT (dash), and WINDSAT (dash-dot-dot-dot).	60
Figure 20	850 hPa relative humidity analysis and forecast errors averaged horizontally. (a) Global, (b) Northern hemisphere, (c) Tropics, (d) Southern hemisphere. Shown are CONTROL (dot), LIDAR (solid), STATSAT (dash), and WINDSAT (dash-dot-dot-dot).	61
Figure 21	Geopotential height analysis error vs. pressure averaged horizontally and over the last 5 days of the assimilation period. (a) Global, (b) Northern hemisphere, (c) Tropics, (d) Southern hemisphere. Shown are CONTROL (dot), LIDAR (solid), STATSAT (dash), and WINDSAT (dash-dot-dot-dot).	64
Figure 22	Vector wind analysis error vs. pressure averaged horizontally and over the last 5 days of the assimilation period. (a) Northern hemisphere, (b) Tropics, (c) Southern hemisphere. Shown are CONTROL (dot), LIDAR (solid), STATSAT (dash), and WINDSAT (dash-dot-dot-dot).	66
Figure 23	Relative humidity analysis error vs. pressure averaged horizontally and over the last 5 days of the assimilation period. (a) Northern hemisphere, (b) Tropics, (c) Southern hemisphere. Shown are CONTROL (dot), LIDAR (solid), STATSAT (dash), and WINDSAT (dash-dot-dot-dot).	67
Figure 24	Temperature analysis error vs. pressure averaged horizontally and over the last 5 days of the assimilation period. (a) Global, (b) Northern hemisphere, (c) Tropics, (d) Southern hemisphere. Shown are CONTROL (dot), LIDAR (solid), STATSAT (dash), and WINDSAT (dash-dot-dot-dot).	68

Figure 25	Number of lidar returns as a function of model sigma level for 12 UTC 19 November 1979. A sigma value of 1 corresponds to the surface level.	71
Figure 26	500 hPa height forecast errors as a function of time averaged over the day 3, 5, and 7 forecasts. (a) Global, (b) Northern Hemisphere, (c) Tropics, (d) Southern Hemisphere. Experiments shown are LIDAR (solid), CONTROL (dot), STATSAT (dash), and WINDSAT (dash-dot-dot-dot). Figs. 27 through 29 have the same format.	72
Figure 27	850 hPa zonal wind forecast error as a function of time averaged over the day 3, 5, and 7 forecasts. See fig. 26 for format and labelling.	74
Figure 28	200 hPa zonal wind forecast errors as a function of time averaged over the day 3, 5, and 7 forecasts. See fig. 26 for format and labelling.	76
Figure 29	850 hPa relative humidity forecast errors as a function of time averaged over the day 3, 5, and 7 forecasts. See fig. 26 for format and labelling.	78

List of Tables

Table 1	OSSE Data Usage.	14
Table 2	Number of Radiosonde Observations at the Top of the First Four Sigma Layers for 1200 UTC 21 November 1979.	15
Table 3	Critical RH Values for Cirrus Cloud.	19
Table 4	Latitude Dependent Tropopause Pressure used in Cirrus Diagnosis.	19
Table 5	Lidar Return Totals by Type and Level for 6 Hour Period.	22
Table 6	Lidar System Parameters.	25
Table 7	Amplification in Radial Wind Error vs. Distance to Subtrack for current OSSE.	30

1. INTRODUCTION

This report summarizes our efforts to assess the usefulness of a doppler wind lidar (DWL) instrument for numerical weather prediction. Recently, a great deal of attention has been focused on the remote sensing of winds from space (Curran and others, 1988). The proposed Laser Atmospheric Wind Sounder (LAWS) instrument would allow the retrieval of wind profiles down to cloud tops globally. However, LAWS has very significant energy requirements. In this study we consider the impact of a low energy DWL instrument. Such an instrument will not be able to retrieve winds in clear air but will obtain winds from cirrus layers, the marine planetary boundary layer and from cloud tops. We evaluated the impact of such an instrument by simulating its data coverage and accuracy, and performing an observing system simulation experiment (OSSE) in which all data are simulated and inserted into the Air Force Geophysics Laboratory (GL) Global Data Assimilation System (GDAS). Resulting analyses and forecasts are compared to those in a control scenario in which lidar data is withheld to determine impact of the DWL data.

This report summarizes the results of this experiment. Following the introduction, a short background of the problem is discussed in section 2. This includes a brief historical perspective, recent developments, as well as the motivation for the present study. The general technical approach is discussed in section 3, followed by the specific design of the OSSE in section 4. The simulation methodology for the DWL data is covered in detail in section 5. Section 6 contains a discussion of the data impacts in the analyses and forecasts. Finally, section 7 contains summary conclusions and suggestions for future work.

2. BACKGROUND

Since the advent of meteorological satellites a quarter of a century ago, our space-based perspective of the earth's atmosphere-ocean system has been acquired almost exclusively employing passive imagers and sounders. From the earliest single channel cloud imagers to contemporary multispectral scanners and sounders, passive sensor systems have undergone continuous evolution with each succeeding generation of instrument resulting in higher spectral resolution, narrower fields-of-view, and improved detector sensitivity. These advances have been manifested in more accurate and spatially resolved measurements of desired meteorological fields such as those of cloud, temperature, moisture and winds. To date, passive systems have been the key components of the deployed meteorological sensor complement of the Defense Meteorological Satellite Program (DMSP). While af-

fording certain advantages characteristic of a mature technology regarding weight, power, reliability, and cost, passive sensors are not without their inherent instrumental deficiencies. Among these are intrinsic physical limitations on attainable accuracy and vertical resolution and the inability to provide operationally useful measurements of some desired observables.

In order to effectively fulfill its global mission, the Department of Defense (DoD) has established specific observational requirements for the acquisition of high quality geophysical and meteorological data. Among the stated specifications for each desired parameter are coverage area, horizontal and vertical resolutions, mapping accuracy, and the range, accuracy, and precision of the measurement. Temporal specifications include the data refresh period or frequency and the measurement's timeliness. While extant satellite-borne passive sensors partially satisfy some of these needs, remaining gaps in operational observational capabilities make it prudent to consider alternative remote sensing technologies. Active remote sensor systems known as lidars have the potential to bridge some of these gaps, particularly those due to the inability to measure a given parameter using passive means or deficiencies in accuracy and resolution. Thus, the development of space qualified laser-based sensor systems for actively probing the atmosphere promises to significantly enhance the state-of-the-art of satellite remote sensing.

Numerical weather prediction (NWP) technology and practice have also evolved significantly since their operational beginnings in the 1950s and 1960s. Inferences of atmospheric temperature and moisture, clouds, precipitation, winds, and surface properties are currently made from a variety of passive visible, infrared, and microwave satellite sensors. For global NWP it is primarily the retrieved temperature profile and wind data which are used. The usefulness of other geophysical parameters for NWP is not well established and is largely untested, although a great many retrieval methods have been proposed or developed for a variety of potentially interesting parameters. Moisture variables - that is, specific humidity, clouds and precipitation - are retrievable and are potentially very useful, but are not easily assimilated by current methods. It is theoretically possible to retrieve specific humidity profiles by using methods analogous to those used to retrieve temperatures. However, results to date with available sensors have not been wholly satisfactory. A variety of other meteorological parameters which may be used for NWP are retrievable. These include winds at the surface from microwave sensors and cloud drift winds aloft, as well as other surface properties, such as soil moisture, albedo, snow cover, temperature, and fluxes. Positive impact of current satellite observing systems on global NWP has been demonstrated, especially in the southern hemisphere where conventional data sources are lim-

ited. Increasing the accuracy and vertical resolution of the sensors and improving the retrieval and assimilation systems should lead to better forecasts. We believe, nevertheless, that only a small part of the potential usefulness of satellite remote sensing for global NWP has been realized and that lidar sensor systems may play a significant role in this evolution. For example, previous OSSEs with the GL GDAS (Hoffman *et al.*, 1990) using a DWL system which returns complete wind profiles (WINDSAT) have shown significant positive impact upon analyses and forecasts of both height and wind relative to control experiments. Other investigators using different assimilation systems have also found WINDSAT data useful to varying degrees (Arnold *et al.*, 1985; Atlas *et al.*, 1985; Dey *et al.*, 1985).

Currently, NASA is in the process of defining the instrument and platform characteristics of the Laser Atmospheric Wind Sounder (LAWS) as part of the Earth Observing System (EOS) initiative. As presently defined (Curran, 1989) the LAWS instrument would be a relatively high power active DWL sensor (10 J pulse) operating at $9\text{ }\mu\text{m}$, potentially capable of returning complete profiles of horizontal wind from the top of the troposphere to cloud top with a vertical resolution of approximately 1 km and a horizontal resolution of 100 km. Anticipated accuracies are on the order of $1\text{--}3\text{ ms}^{-1}$ rms. The baseline plan has LAWS on board a polar orbiting satellite, but other scenarios are under study (Atlas, pers. comm.).

However, there are legitimate concerns regarding the weight and power requirements of an instrument such as LAWS. Secondly, the ability of the instrument to obtain complete vertical profiles of wind through the troposphere is critically dependent upon the presence of sufficient backscattering aerosol. Data from the Global Backscatter Experiment (GLOBE) should help resolve this, but the answer is far from certain. Finally, the size, weight and power of the instrument are all directly proportional to its ultimate development cost. In this regard, it has recently been determined that LAWS will not be included in the instrument package slated to fly aboard the Japanese Polar Orbiting Platform (JPOP) due to its "high risk" nature.

The approach adopted for this study is to assess the NWP utility of a down-scaled (i.e. lower power and weight) DWL instrument which addresses these concerns (note that the primary LAWS objective is global change monitoring). The scaled back instrument would be smaller, operate at lower power levels (1 J pulse), and work at a near-infrared wavelength (see Table 6). These characteristics would lower the cost, decrease demands upon the host platform, and, relative to a comparable infrared lidar, increase the backscatter signal. Since the instrument is operating at lower power, we assume that viable returns will only occur at or near

"hard" targets where backscattered signal is sufficient. These targets are cirrus cloud, the tops of other clouds and marine boundary layer aerosol.

Finally, we note that range gating of the laser pulse itself can allow fairly accurate estimation of the target height. Although not utilized in the experiments conducted here this could be used to infer cloud top height which might also be incorporated into a data assimilation system.

3. TECHNICAL APPROACH

3.1 Lidar Measurement

The basic principle of lidar techniques is that information about the physical state of the atmosphere or hard target can be inferred from the way in which the laser signal is backscattered and attenuated by atmospheric constituents. The theoretical expression relating the measured signal to the state of the atmosphere is the lidar equation:

$$E_r(\nu', R) = E_t(\nu) \tau_o(\nu') \tau_f(\nu') \tau^2(\nu, \nu', R) \cdot (A/R^2) \cdot \{ [\beta_a(\nu, \nu', R) + \beta_m(\nu, \nu', R)] \Delta R \} \quad (3.1)$$

where ν_n and ν' are the transmitted and received frequencies, respectively. E_t is the transmitted energy and E_r is the energy received from a range cell of thickness ΔR centered at a distance ΔR , τ_o and τ_f are the system parameters for optical transmission and filter transmittance, A is the receiver area, τ^2 is the two-way atmospheric transmittance, β_a and β_m are aerosol and molecular backscatter coefficients respectively. For hard target measurements, the term in brackets containing the backscatter quantities is replaced by surface reflectivity or albedo. With the exception of winds, information on the state of the atmosphere is contained in the terms β_a , β_m and τ^2 . Wind fields can be derived by measuring the Doppler shift of the backscatter signal from tracer aerosol particles: $\Delta\nu = \nu' - \nu = 2\nu v/c$ where ν is the component of wind velocity along the sensor line of sight.

3.2 Doppler Wind Lidar Sensors

Aerosols suspended in the atmosphere can serve as wind tracers for lidar measurements. A photon backscattered by an aerosol particle moving at a wind velocity (ν) in the line-of-sight will experience a Doppler shift in frequency of magnitude $(\Delta\nu/\nu) = (2v/c)$, where c is the speed of light. Photons scattered by particles moving toward the observer in the line-of-sight will experience

an increase in frequency, while those scattered by particles receding from the observer will display a decrease in frequency. The Doppler shift caused by aerosol backscatter of a highly stable quasi-monochromatic laser beam could be spectrally analyzed to yield the line-of-sight component of wind velocity. In practice, measuring winds by this method is very difficult because of several facts:

- The Doppler shift is extremely small: a 1 ms^{-1} wind (line-of-sight) results in a $-3 \times 10^{-1} \text{ nm}$ shift at $0.5 \mu\text{m}$, or $-6 \times 10^{-5} \text{ nm}$ at $10 \mu\text{m}$.
- The spacecraft velocity, which is about 8 km s^{-1} , also contributes to the Doppler shift. The contribution of this velocity along the line-of-sight of the measurement must be determined to a high accuracy. This places stringent requirements on instrument pointing knowledge and spacecraft attitude.
- The aerosol backscattered signal is often quite small (particularly in the altitude range of 5-12 km where winds are very important) and at some frequencies is dwarfed by the much stronger molecular backscattering which acts to broaden the original signal.

There are two major techniques using coherent and incoherent detection, to determine wind velocity in this way. The coherent method uses heterodyne detection; mixing the backscattered signal with a local oscillator to yield a beat frequency proportional to the Doppler shift. The incoherent technique measures spectral shifts using a Fabry-Perot interferometer with an array-type detector. The relative advantages and disadvantages of the two systems are discussed by Salvetti (1987), and Baker and Curran (1985). These three works also summarize potential implementations of DWLs. It is now considered technically feasible to measure wind profiles from space by measuring the Doppler shift of a transmitted laser pulse (Salvetti, 1987; Curran and others, 1988). With a strong enough signal the reflected pulse may be range gated to yield vertical resolution of 1 km or better. The strength of the reflected signal depends principally on the energy transmitted and the reflectivity of the atmospheric volume being sampled. Since the laser may be focused to a very fine solid angle, horizontal resolution as fine as desired (down to scales of meters) may be obtained. Further, the lidar measurements are a direct measure of the line of sight (or radial) velocity. Thus if the reflected signal strengths are sufficient any reasonable desired accuracy might be obtained by this technique. Two measurements of the same atmospheric volume from different viewing angles, along with the assumption that vertical velocities are negligible, are required to infer the u and v wind components. The simplest method of accomplishing this is to use a conical scan pattern (cf. Fig. 19 of Curran *et al.* (1988)). The global distribution of aerosol is not well known. Since the aerosol concentration directly effects the atmospheric reflectivity to the lidar

signal, the relationship of the DWL errors to the transmitted energy cannot be reliably predicted. However, in the experiments conducted here, we obtained an estimate of measurement error by assuming several aerosol and cloud drop size distribution scenarios. In particular, we assume sufficient aerosol particles in the marine boundary layer to enable a measurement to be made.

3.3 NWP Related Lidar Instrument Characteristics

From the point of view of numerical weather prediction (NWP), the most important characteristics of any proposed remote sensing system are its geographical coverage, horizontal and vertical resolution and its error characteristics. In a simulation study these characteristics must be properly accounted for. These considerations lead immediately to a number of issues which bear on simulation experiments.

1. Lidar coverage depends on cloudiness. Since the lidar pulse penetrates the cloud only weakly and since multiple scattering from the topmost part of the cloud contaminates any signal received from below, it is impossible to retrieve wind profiles below clouds. In the present experiments, there will be no lidar data at points below large scale cloudiness. This is perhaps pessimistic, since on-board shot management might find holes in some of the cloud formations.
2. For NWP, it is not just accuracy of the measurement which is important, the measurement must be representative as well. NWP is really concerned with the spatially and temporally smoothed behavior of the atmosphere. That is variations on the scale of meters and seconds, in fact on the scale of kilometers and minutes, are generally considered to be averaged over and are parameterized within the model. Consequently, that part of the measured signal attributable to these scales is considered to be noise from the NWP point of view. This source of error can in some cases be predominant. The representativeness issue is of some importance to lidar measurements. Lidars naturally average in the vertical. This is good for NWP, however, this average is weighted by the vertical profile of aerosol concentration. Our concern lies in the horizontal shot pattern. Since the atmospheric volume sampled may be only meters across and there is no temporal averaging, lidar measurements will contain large errors of representativeness. Averaging many shots would overcome this error source, but shot patterns which have been proposed have a typical separation between neighboring shots of 100 km.
3. Spatially correlated errors are difficult for an analysis scheme to remove, because the data tend to corroborate each other. Real data tend to have correlated errors. Even for radiosondes, significant vertical error correlations

are present. DWL data errors might be strongly correlated, for example, if they are due to an error in the estimate of spacecraft velocity.

4. OSSE DESIGN

The OSSE which was conducted is composed of four components: (i) the nature run, a simulation of the atmosphere, (ii) a simulation of the observing system, (iii) a quasi-operational global NWP 4D assimilation and forecast system, and (iv) a comparison methodology. Many aspects of these components have been described at length in previous reports and publications (Hoffman *et al.*, 1990; Louis *et al.*, 1989) and are only briefly discussed here.

4.1 The Nature Run

The nature run is the data set from which simulated data are extracted. Ideally the nature run would be a detailed history of the real atmosphere. Unfortunately, any series of analyses of the atmosphere contains substantial errors due to observational errors, analysis methodology errors, forecast model, and initialization errors. Because of this, OSSEs require a simulated nature run. This model should be different from the model used in the 4D assimilation to avoid the identical twin problem in which the simulated analyses are unrealistically similar to the nature run. This model must also have high resolution, sophisticated physics, and a reasonable climatology.

In this study, the nature run is a 20 day ECMWF forecast beginning at 00 UTC 10 November 1979 from the Global Weather Experiment (GWE) IIb analysis produced at the European Center for Medium Range Weather Forecasting (ECMWF) (Bengtsson *et al.*, 1982). The model used in the nature run forecast was a version of the 15 layer, 1.875 degree gridpoint model (Hollingsworth *et al.*, 1980). This model included fairly complete physics (Tiedtke *et al.*, 1979) with a diurnal cycle. We used the archived forecast fields which were available every 12 hours, interpolated to 2.5 degree resolution. Since the nature run is relatively smooth, this slightly degraded resolution is a satisfactory representation.

4.2 The Simulated Observing Systems

The simulated observing systems should be as sophisticated as possible with reasonable computation constraints. Characteristics of all observations and their errors must be treated. In particular, with respect to the lidar data, the clouds and aerosols predicted by the nature model should be used in determining the spatial distribution of the data and its overall accuracy. Note that the most interesting

meteorology is often associated with clouds. The horizontal and vertical sampling characteristics of the wind sensor must be properly modeled. Here we briefly describe the other simulated data which were used in the OSSEs. Details of the lidar simulation methodology are contained in the next section.

With the exception of the lidar observations, all data were simulated at the National Meteorological Center (NMC) by replacing nearly all valid GWE level IIb observations obtained during the special observing periods with simulated observations at the same locations. The observing systems include conventional observations such as raobs and aireps, as well as satellite cloud drift winds (CDW), and satellite temperature soundings (TOVS). The simulated standard data were created by interpolating nature data to the GWE observation and adding a random observing error. This procedure yields quite reasonable data coverage and quality control in the simulated data. However, certain discrepancies are possible: for example, cloud drift winds may be present where there are no clouds in the nature run. With regard to the CDWs, these simulated observations were treated differently from the CDWs used in previous OSSEs. The errors of these observations were modified to be more representative of real CDW measurements, as described below.

4.2.1 Filtering of CDW Errors

The CDWs simulated by Dey *et al.* (1985) have random error only, whereas we know a sizeable fraction of the error is due to height assignment errors (McPherson, 1984). Further sources of error are the fact that cloud base, not the cloud top, may be the best level for assigning the winds and the deviations from unit emissivity for the cloud. These errors, especially the height errors, tend to be very well correlated (at least at a particular synoptic time) for a particular data producer. The cause of the height assignment errors is fundamental. Generally two approaches to height assignment have been used:

1. The climatological approach. For example, assigning all low level wind to 900 mb or assigning all high level wind to the climatological tropopause.
2. IR radiance approach. In this technique the observed IR cloud radiance is used to deduce a cloud top temperature, which is then matched to a temperature profile specified from a recent analysis or short term forecast.

The CDWs simulated by Dey *et al.* essentially used an error free temperature profile for height assignment. We could reassign the pressures by adding an ad hoc error to the CDW pressures directly, or by assuming an ad hoc temperature error and reassigning the pressure by comparing the "observed" temperature to

the nature run. These errors would have to be fairly large. These approaches would indirectly create horizontally correlated errors.

We have chosen to more directly induce correlated errors in the CDW data by spatially filtering the errors in the simulated data. We divided the data into high and low winds and filtered the u and v wind components for each group separately. As seen in figure 1 the distribution of observing pressures has two major modes and we chose 600 mb as the dividing pressure. The data are for 12 UTC, 21 November 1979; there were a total of 1935 CDWs. The filter we use is a weighted average followed by an amplification step. The averaging reduces the amplitudes of the original errors, while inducing correlations. The amplification step multiplies all weighted average errors by a constant factor to restore the original amplitude of the error variance. This constant is equal to the variance of the original errors divided by the variance of the filtered errors. The weighted average operator is equivalent to the first pass of a Barnes filter (Koch *et al.*, 1983). The weights, w , are given in terms of the distances, d , between the point to be filtered and the nearby points, according to $w = \exp(-(d/d_0)^2)$. Here d_0 is the scale of the filter and all points within $2 \times d_0$ are included in the weighted average. After filtering a random error field, correlations drop to approximately 0.5 at a separation distance of d_0 . We chose d_0 to be 0.1 earth radii or approximately 637 km.

The results of the filter on the horizontal correlations of the CDW errors is shown in figures 2 and 3 for the low and high wind groups. For reference the correlation of the nature run evaluated at the same data locations is presented in the upper row of plots. Correlations of the original errors are displayed in the center row and correlations of the filtered errors are displayed in the lower row of plots. As indicated the results for the u and v wind components are displayed in the left and right columns respectively. Note that the errors are treated by the filter as if they were all at a single level (separately for high and low winds). On the other hand, the nature data used for the correlations are at a variety of pressure levels. The synoptic scale is clearly evident in the v correlations from the nature run. This is not obvious in the u correlations because of the strong zonal component, especially at higher levels.

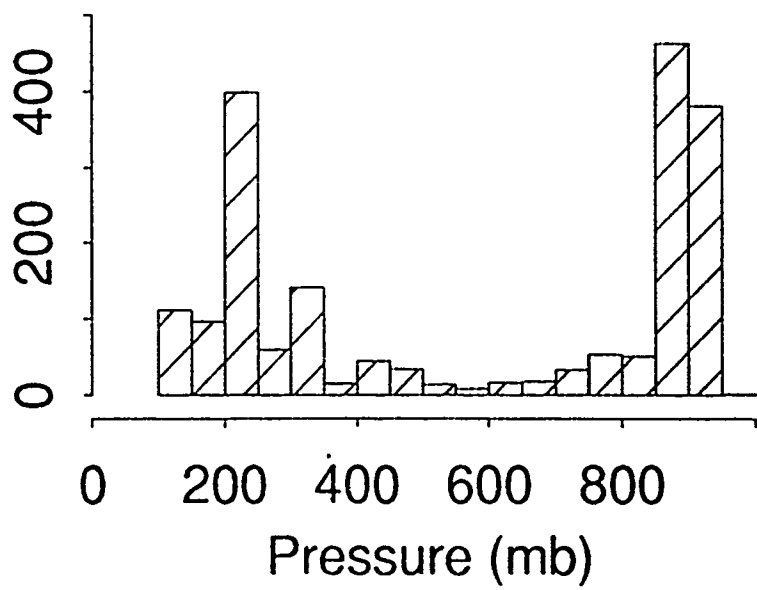


Figure 1. Distribution of CDW press res.

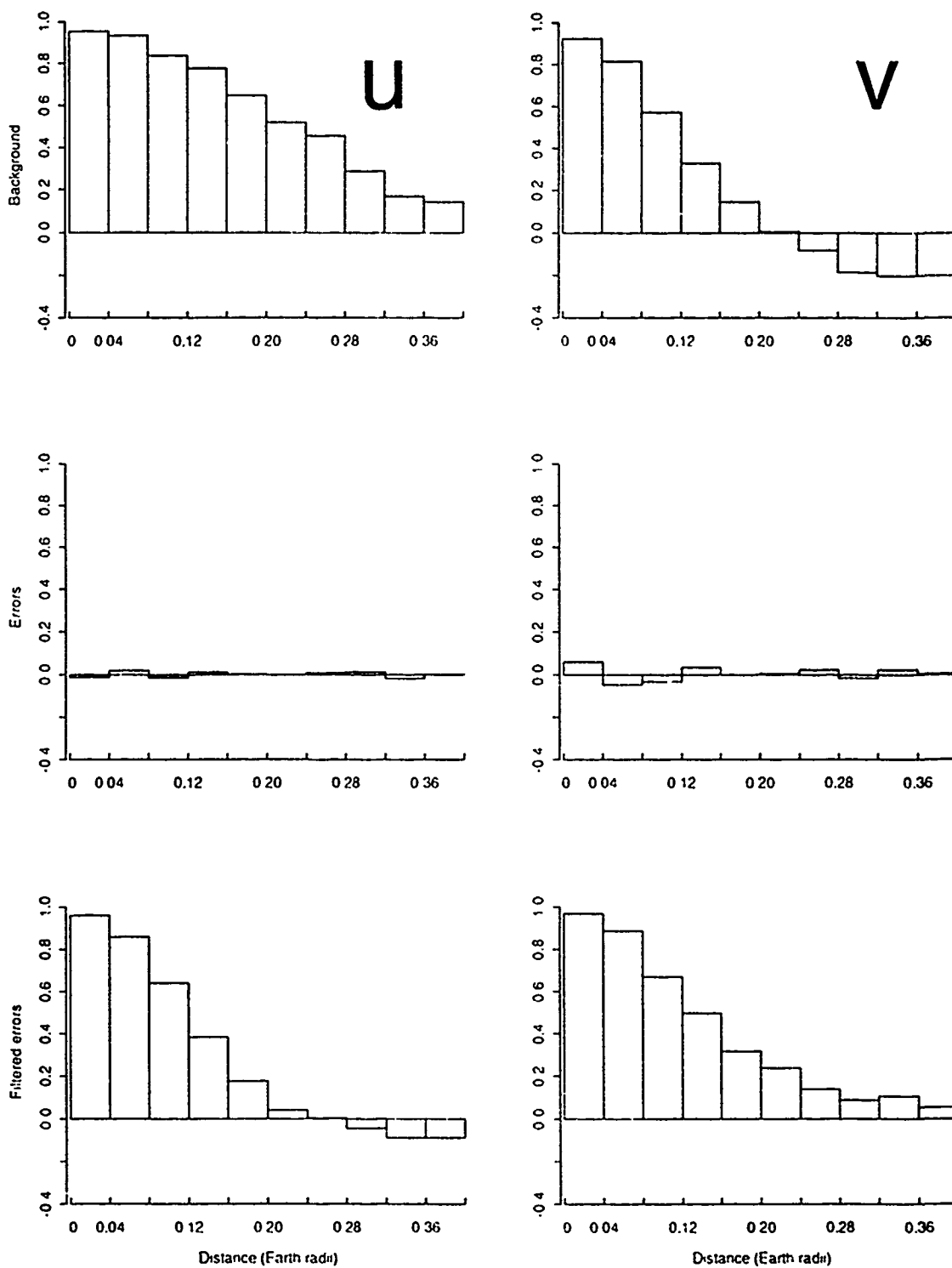


Figure 2. Horizontal correlations for low level (1000-600 mb) CDWs. Shown are correlations for the background field evaluated at the CDW locations (top), original CDW errors (middle) and filtered CDW errors (bottom) for u (left) and v (right) wind components.

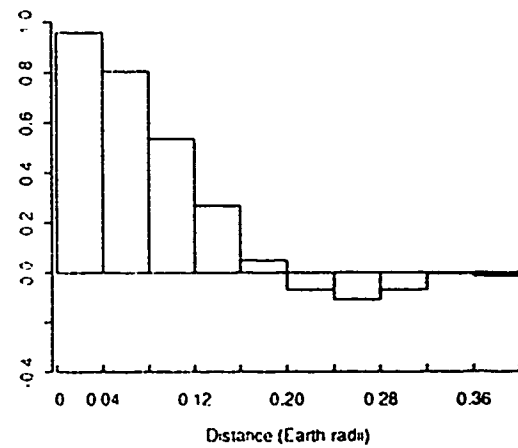
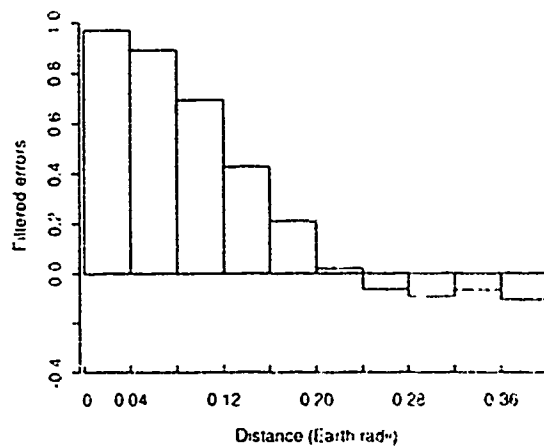
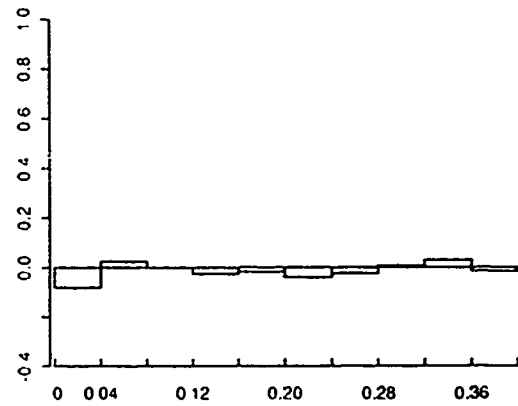
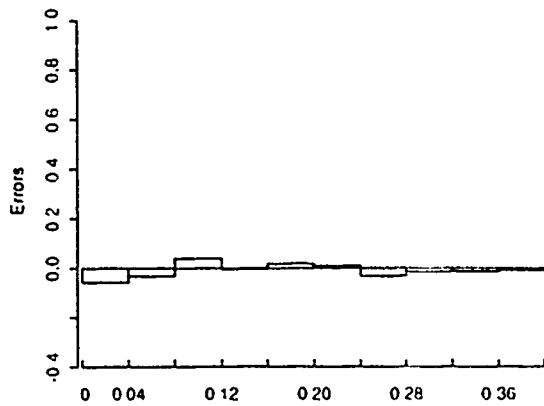
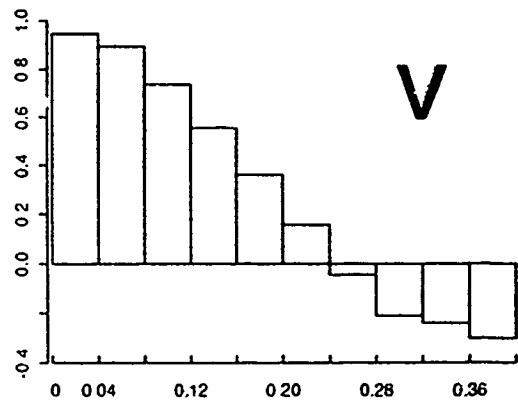
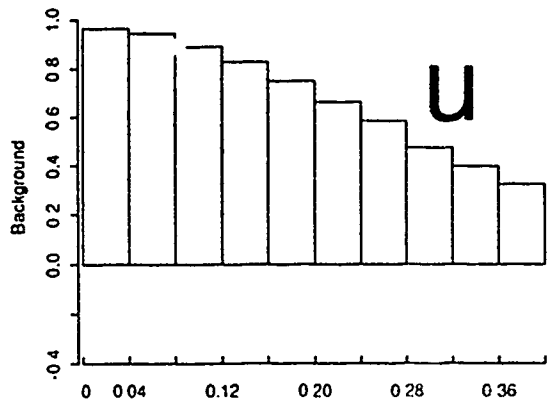


Figure 3. Horizontal correlations for high level (600-100 mb) CDWs. Same as Fig. 2.

4.3 The 4D Assimilation System

Each simulated data assimilation experiment consists of one assimilation run from 00 UTC 18 November through 00 UTC 25 November 1979 and three 96-hour forecasts from 00 UTC 21, 23, and 25 November. Each assimilation run consists of a series of assimilation cycles, and each cycle in turn is made up of a 6-hour forecast that serves as the background or first guess field for the analysis, an optimal interpolation analysis that combines the first guess fields with the observations, and a nonlinear normal mode initialization of the analysis. The initialized analysis is the starting point for the next 6-hour forecast, which again serves as the first guess field for the subsequent analysis.

The AFGL Statistical Analysis Program (ASAP) (Norquist, 1986; Norquist, 1988) was developed from the NMC multivariate optimal interpolation (OI) procedure as described by Bergman (1979) and by McPherson *et al.* (1979). The OI is a multivariate analysis of height and wind components and a univariate analysis of relative humidity. The corrections for an analysis grid point are weighted sums of surrounding observation-minus first-guess residuals. Equatorward of 70 degrees, these weights are calculated as described by Dey and Morone (1985). In the polar regions, the Bergman (1979) formulation is used. The analysis is performed in the sigma coordinates of the model on a Gaussian grid of 62 x 61 latitude-longitude points. Recent changes to the OI and documentation are discussed below.

The GL normal mode initialization (NMI) is based on the NMC NMI (Ballish, 1980). The GL global spectral model is based on the NMC GSM designed by Sela (1980). For the version used here, the physics routines, taken almost intact from NMC (circa 1983), include surface exchanges of heat, moisture, and momentum over the ocean; surface exchanges of momentum over land; a dry adiabatic adjustment; large scale supersaturation precipitation; and a Kuo convection scheme. The hydrodynamics; i.e., the adiabatic, inviscid dynamics including vertical and horizontal advection, time stepping, and transformations between spectral and physical space; were redesigned, as documented by Brenner *et al.* (1982;1984).

The spectral resolution of the forecast model itself is defined by a rhomboidal truncation at wave number 30. The Gaussian grid of the forecast model contains 76 x 96 latitude-longitude points. There are 12 vertical layers, the top 5 of which have no moisture.

4.4 Comparison Methodology

To determine possible impact of the lidar observing system, output from the GDAS is examined for cases run with (LIDAR) and without (CONTROL) the inclusion of the DWL data. Table 1 summarizes data usage for the CONTROL and LIDAR experiments. Subjective evaluations are made by looking at the standard meteorological variables (e.g. horizontal wind, geopotential height, and relative humidity) on synoptic charts. More objective comparisons are also made using calculations of global and regional error statistics.

Table 1. OSSE Data Usage.

	Conventional	CDW	TOVS	DWL
CONTROL	X	X	X	
LIDAR	X	X	X	X

The CONTROL experiment represents a new baseline case which was run to measure the DWL impact. It differs from the original baseline experiment known as STATSAT used in earlier OSSEs, (Hoffman *et al.*, 1990) in that it features more realistic CDWs (see above) and a modified OI.

Essentially, changes to the analysis system were made in three main areas:

- **Variable resolution**

A series of changes were made to the analysis codes (ASAP and MASAP) and their associated pre- and postprocessors to allow for variable resolution. The changes to the analysis codes were made as a series of small changes, so that the results of the initial code with small errors could be reproduced, the source of which could be clearly identified. Significant changes have been reflected in the new documentation for ASAP (August 1989). Note that all common blocks are now "included" and are the same whenever they are used. The constants for LOWTMP (the Flattery algorithm) are calculated once at the start of ASAP, since these constants depend on the vertical structure. The code is now strictly standard FORTRAN. The largest differences during this series of modifications are due to the calculation of the LOWTMP constants to full machine precision instead of specifying them on a DATA statement to 9 or 10 digits. Modifications for MASAP paralleled those for ASAP. In particular all commons are now "included". Previously the first guess error growth rates on the model sigma structure were hardwired in the code. Now these rates are

stored at mandatory levels and interpolated to the sigma structure. This was the one change which produced errors detectable at the $O(10^{-3} \text{ g kg}^{-1})$ level. The pre- and postprocessors (PPPs) were completely redesigned, in a modular fashion. Since the GSM PPPs already exist in variable resolution format, we only implemented our design for the PPPs for the OI.

- **Surface pressure analysis**

The surface pressure update was reformulated. The previous update was described by Norquist (1986, pp. 122-123) and involved extrapolating the heights at the top of the lowest three layers for both the background and analysis to the $\sigma = 1$. The new formulation uses the lowest and underground layer height increments to estimate the height increment at $\sigma = 1$, which is then converted hydrostatically to a pressure increment. This approach is similar to that used by the ECMWF.

- **Use of RAOB heights**

The radiosonde heights interpolated to the sigma levels are now used directly as observations. Previously, these data were used only for thicknesses; they were differenced hydrostatically to obtain layer temperatures which were then anchored to the first guess heights (usually at the top of layer 1) or to the model topography. The latter case would only hold if the raob profile started below the model topography, while in the former case the first height datum would be at the top of the layer above the anchoring level (normally layer 2). Consequently, this change increased the number of raobs at the lowest levels as indicated in table 2 below.

Table 2. Number of Radiosonde Observations at the Top of the First Four Sigma Layers for 1200 UTC 21 November 1979.

σ Level	1	2	3	4
STATSAT	250	435	671	672
CONTROL	439	673	690	679

The use of absolute heights is probably more important than the increase in the number of low level observations.

These changes were incorporated incrementally to isolate the relative impacts of each, and to determine the effect of machine word length on the analyses (testing was done both on the GL Cyber and the AER Alliant). All the above modifications have been described at length in the contract quarterly status reports (no. 2, no. 3, and no. 4; GL Contract F19628-89-C-0044).

In Figure 4 rms height errors are shown for both CONTROL and STATSAT assimilation runs. These indicate a substantial reduction in analysis error of approximately 10 m for CONTROL.

5. LIDAR DATA SIMULATION METHODOLOGY

The methodology used to simulate the lidar data includes a sampling strategy (i.e. where to locate potential measurements), a cloud and aerosol diagnosis (since these determine the vertical and horizontal distribution of viable lidar returns), and measurement errors (which are a function of instrumental characteristics, scanning geometry, and assumed cloud/aerosol backscatter characteristics).

5.1 Data Sampling

As noted above, an extended 20 day forecast of the ECMWF grid point model serves as our ground truth for verification and cloud diagnosis. This is the same nature run used in previous OSSEs (Hoffman *et al.*, 1990). The data (wind, temperature, and relative humidity) on a 2.5 degree resolution grid are interpolated in space and time to the horizontal location of the anticipated lidar measurement.

The actual locations of the lidar measurements have been determined using the orbital parameters of the DMSP polar orbiting platform and the instrumental scan parameters of the cross-tracking Special Sensor Microwave temperature (SSM/T) sounder (Isaacs *et al.*, 1985). In practice the lidar instrument will be conically scanning with each of these prescribed locations the result of intersecting fore- and aft-looking shots (line of sight measurements) binned in a grid like that of the SSM/T instrument. Thus, the important geometric features of the conically scanning lidar may be deduced from the observation locations. The scanning geometry, in turn, affects the nature of the measurement errors, which are discussed below.

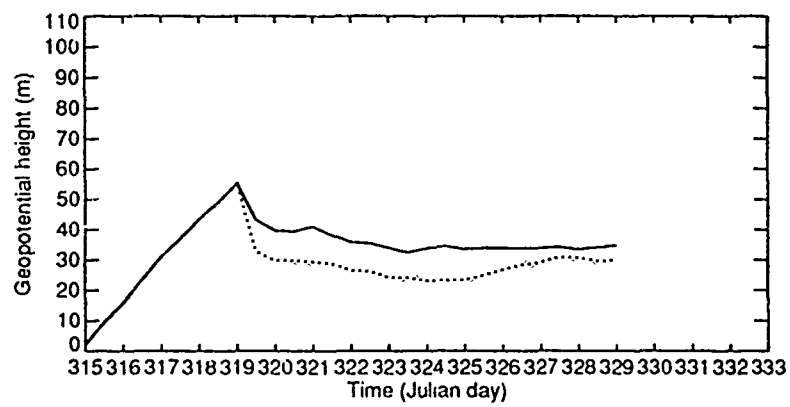


Figure 4 RMS height errors at 500 hPa for STATSAT (solid) and CONTROL (dotted) assimilation experiments.

5.2 Cloud and Aerosol Diagnosis

In our simulations three types of lidar returns are allowed for: (1) liquid water cloud, (2) cirrus cloud, and (3) marine boundary layer aerosol.

5.2.1 Liquid Water Cloud

Liquid water clouds are diagnosed using the Geleyn scheme. In this formulation the cloud fraction at each nature run moist level is parameterized in terms of the actual relative humidity and a predefined critical relative humidity at that level as:

$$CC(k) = \left[\frac{RH(k) - RH_c(k)}{100. - RH_c(k)} \right]^2 \quad (5.1)$$

where $RH(k)$ is the relative humidity at level k , $RH_c(k)$ is the critical relative humidity at level k , and $CC(k)$ is the computed cloud fraction at level k . RH_c is itself a function of pressure and we have used the same values that were used in the cloud parameterization scheme during the forward integration of the nature run. Values of RH_c at the six pressure levels from 1000 mb to 300 mb are: 100.0, 59.0, 50.0, 60.3, 72.5. Note that this diagnosed cloudiness is only the large scale, non-convective amount.

5.2.2 Cirrus Cloud

Cirrus clouds are diagnosed from both the relative humidity (RH) and temperature (T) at the observing location. We have adopted a simple thresholding approach such that a cirrus/ice cloud is present whenever both the T and RH fall below and above their critical values, respectively. The critical T has been fixed throughout at 253 K, although a dependence on latitude and level might be considered. A latitude-dependent critical RH was used to simulate this feature of published cirrus climatologies. Values of critical RH were tuned to approximate the fall time period zonal climatology derived from Stratospheric Aerosol and Gas Experiment (SAGE) data shown by Woodbury and McCormick (1986). These values are shown below.

Table 3. Critical RH Values for Cirrus Cloud.

Latitude (deg.)	RH _c (%)
-20 → +20	60.
± 20 → ± 40	80.
± 40 → ± 70	70.
± 70 → ± 90	85.

Comparison with the SAGE-derived climatology is shown in figure 5. These results correspond to one six hour interval during the 7 day assimilation period, but are generally representative of other times during the period as well.

Since the nature run data only contains moisture information up to 300 mb we need to allow for the occurrence of cirrus at higher levels. To do this we assume that any time cirrus is diagnosed at 300 mb it extends all the way up to the tropopause level. The tropopause level is a fixed function of latitude ranging from 100 mb in the tropics to 300 mb in the polar regions as indicated in Table 4 below. No attempt is made to deduce a cirrus cloud fraction or cloud opacity from the nature run.

Table 4. Latitude Dependent Tropopause Pressure used in Cirrus Diagnosis.

Latitude (degrees)	P _{tropopause} (mb)
± 70 → ± 90	300.
± 50 → ± 70	250.
± 30 → ± 50	200.
± 10 → ± 30	150.
0 → ± 90	100.

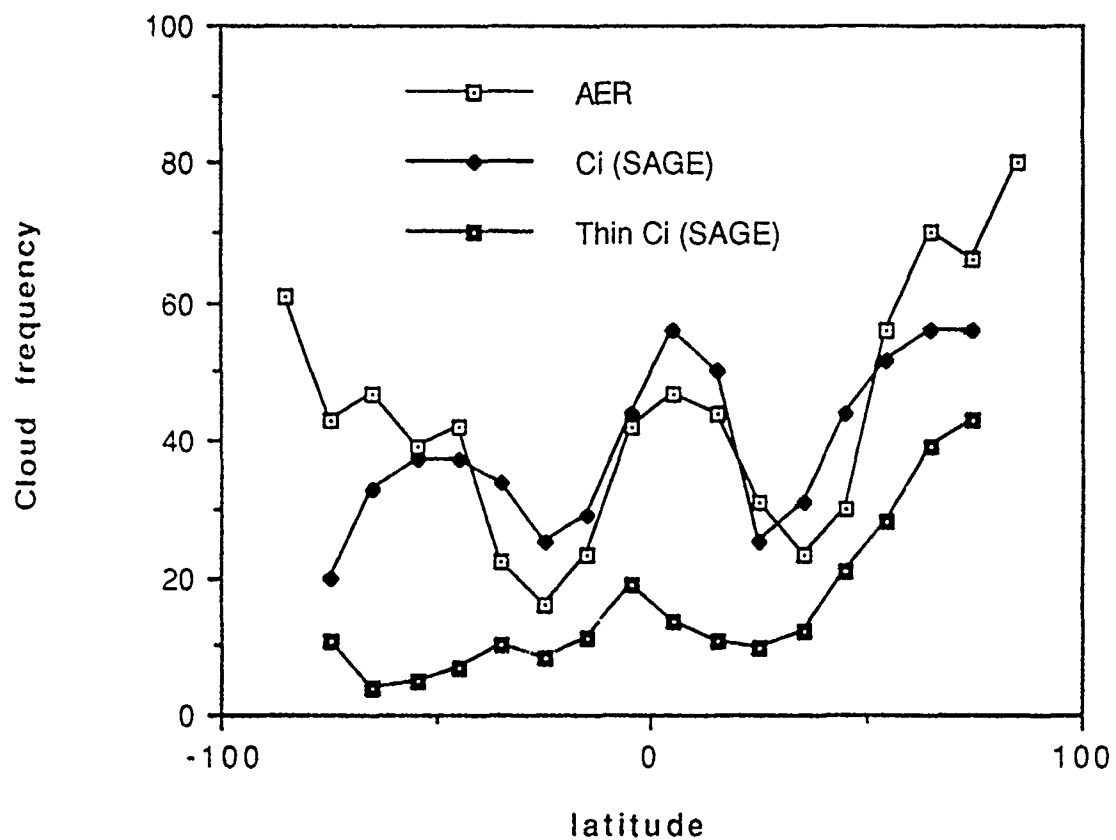


Figure 5. Comparison of cirrus occurrence determined from SAGE data vs. that obtained in current OSSE. SAGE results valid for September, October, November time period. AER results valid for 18 November 1979, 06 UTC.

5.2.3 Marine Aerosol

We have assumed that the marine boundary layer will always contain sufficient aerosol for a lidar measurement. Therefore, any observing location over the unfrozen oceans (sea ice extent is set at November climatology) contains marine aerosol in the boundary layer, which is assumed to be of fixed depth with a top at 850 mb.

5.2.4 Measurement Decision Algorithm

The process whereby the particular geophysical profile at an observing location is analyzed for the levels of viable lidar returns is essentially a decision tree.

After a profile is analyzed for the liquid water cloud fraction (if any) at each level, the profile is integrated downward from the top of the atmosphere (assuming random overlap) to obtain integrated cloud amounts at each level.

Now the profile may be inspected level by level from the top of the atmosphere downward and a return type assigned to each level. Each level is checked in turn for liquid water cloud, cirrus, and then marine aerosol. For the case of cirrus cloud, its presence is sufficient to permit a measurement since no information on cloud fraction or opacity is known. Additionally, cirrus is assumed to be sufficiently non-opaque so that its presence does not preclude returns from lower level water clouds or aerosol. For liquid water clouds and marine aerosols a measurement occurs if the probability that the cloud level or aerosol layer is seen exceeds a critical value. This probability is just the fraction of the layer or level seen from above and is computed directly from the integrated cloudiness profile. These critical value thresholds are important since they affect the efficiency with which partially visible levels yield wind measurements and are inversely proportional to the assumed strength of the backscattered signal. Therefore, during the data simulation critical values for water cloud and aerosol probabilities were set at 0.3 and 0.5, respectively, since cloud water droplets have stronger scattering characteristics at near infrared wavelengths. Table 5 indicates the lidar return type totals by level for one six hour time interval during the assimilation period in which 4044 profiles were processed. In the table the terms warm and cold cirrus refer to cirrus occurring at temperatures above and below -40 degrees C, respectively.

According to Heymsfield and Platt (1984) this temperature corresponds to a sharp change in observed ice crystal size distribution and lidar backscatter regimes. At the lower temperatures the ice particle concentrations are seen to decrease along with lidar backscatter.

Table 5. Lidar Return Totals by Type and Level for 6 Hour Period.

Pressure (mb)	Total Returns	Water Cloud	Warm Cirrus	Cold Cirrus	Marine Aerosol
50.	0	0	0	0	0
70.	0	0	0	0	0
100.	192	0	192	0	0
150.	432	0	432	0	0
200.	457	0	457	0	0
250.	457	0	457	0	0
300.	1287	0	457	830	0
400.	1191	14	564	613	0
500.	1226	211	794	221	0
700.	1229	710	519	0	0
850.	735	735	0	0	0
MBL	1401	0	0	0	1401

Figure 6 shows the location of lidar measurements at 850 mb for the 6 hour period centered at 12 UTC on 19 November. The observations shown correspond to areas of low level cloudiness. Note again that the distribution of observations is far from complete.

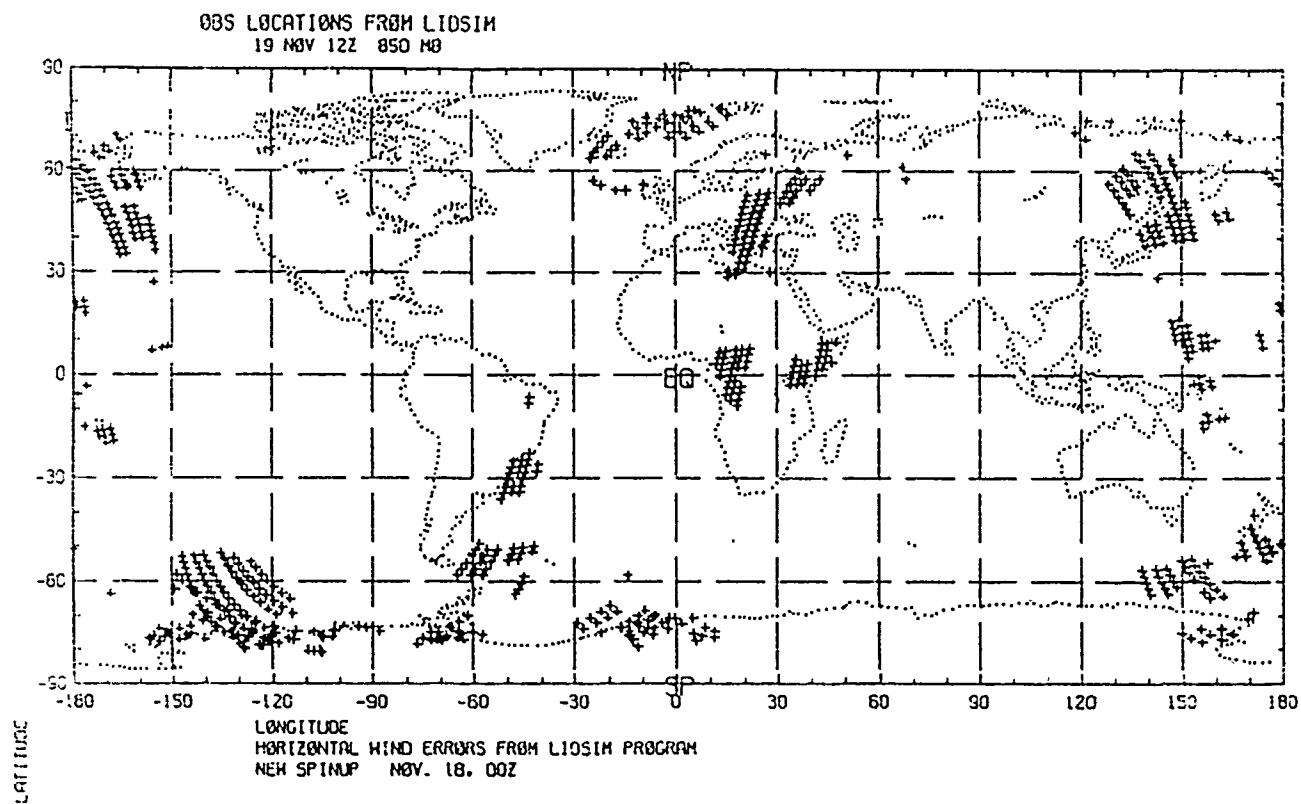


Figure 6. Locations of lidar measurements at 850 mb on 19 November 1979, 12 UTC.

5.3 Measurement Error

Once the return types have been set for each vertical level the data are created by adding an error to the "exact" u and v components at each level found to have a return. The "exact" values are obtained directly from the nature run profile with one exception: the wind in the marine boundary layer is considered to be an average of the wind components at 1000 mb and 850 mb.

5.3.1 Cloud Optical Properties

Cloud optical properties are an important issue because they determine the strength of the backscatter signal received by the sensor and ultimately the accuracy of the measured wind. Specifically, we desire an estimate of the cloud backscatter for various cloud types. For liquid water clouds and boundary layer aerosol we adopted well known models for stratus and stratocumulus drop size distributions and marine boundary layer aerosol distributions. The estimation of cirrus optical properties including extinction and the desired lidar backscatter cross sections was based on the parameterization of the cirrus particle size spectrum by Heymsfield and Platt (1984). This parameterization provides an empirically based relationship between the particle size spectrum of ice clouds and the ambient temperature and ice water content. The ice crystal size distribution over the size range $D > 20 \mu m$ was represented by two power law equations of the form:

$$n(D) = IWC \cdot A_i \cdot D^{B_i} \text{ for } i = 1, 2 \quad (5.2)$$

where n has the dimensions of $m^{-3} \mu m^{-1}$, D is the maximum crystal dimension in μm , and IWC is the ice water content in gm^{-3} . The subscript refers to the break point in the distribution given by a crystal maximum dimension D_o . The constants A_i and B_i are related to the ice concentrations at fixed sizes and the size distribution slopes, respectively. Values of the constants and the ice water content as a function of ambient temperature in the range of -20 to -60 degrees C are given in Table 2 of Heymsfield and Platt (1984). As noted above, one result of their analysis is that an apparent change in ice particle size distribution occurs between -35 and -40 degrees C. This results in a different class of size distributions corresponding to "warm" and "cold" cirrus, respectively. This is consistent with a change in lidar extinction to backscatter ratio noted by Platt and Dille (1981). We have exploited this dependence to simplify our treatment of the temperature dependence of the cirrus backscatter, and, hence, the assignment of simulated wind errors.

To calculate backscatter coefficients we adopt the optical constants for ice from Warren (1984). We have evaluated the backscatter and extinction coefficients corresponding to the temperature dependent size distributions described above using the Mie theory algorithm of Shettle (pers. comm.) Small particle contributions were added to complete the size distribution data. Although Mie theory is strictly applicable to spherical particles, a comparison of asymmetry factors calculated by Takano and Liou (1989) for hexagonal crystals and equivalent ice spheres suggests that, for our purposes, the error is not significant. Figures 7 and 8 illustrate the extinction (km^{-1}) and backscatter ($\text{km}^{-1} \text{ sr}^{-1}$), respectively, which were used in the lidar sounder simulation.

Modeled cirrus backscatter values for "cold" and "warm" cirrus at the lidar wavelength of $2.1 \mu\text{m}$ correspond to about 1.5×10^{-6} and $5.0 \times 10^{-6} \text{m}^{-1} \text{sr}^{-1}$, respectively. The appropriate visible values are approximately three times larger, corresponding to "weak" and "medium" cirrus. Weak cirrus may be visible with sufficient vertical thickness, while medium cirrus will usually be visible.

These cirrus backscatter parameters as well as the appropriate marine aerosol and liquid water cloud models were provided as input to the lidar simulation model at GE AstroSpace Division (D. Hogan, pers. comm.) who performed the line of sight and horizontal wind velocity error calculations. Lidar wind errors were then evaluated based on the nominal system characteristics listed in Table 6.

Table 6. Lidar System Parameters.

Parameter	Value
Wavelength	$2.1 \mu\text{m}$
Sensor altitude	824 km
Scan angle	45 degrees
Scan period	5 s
Pulse energy	1 J
Pulse duration	$.7 \mu\text{s}$
Noise bandwidth	2.2 MHz
Pulse rate	10 Hz
Optics diameter	.5 m
Total efficiency	0.75

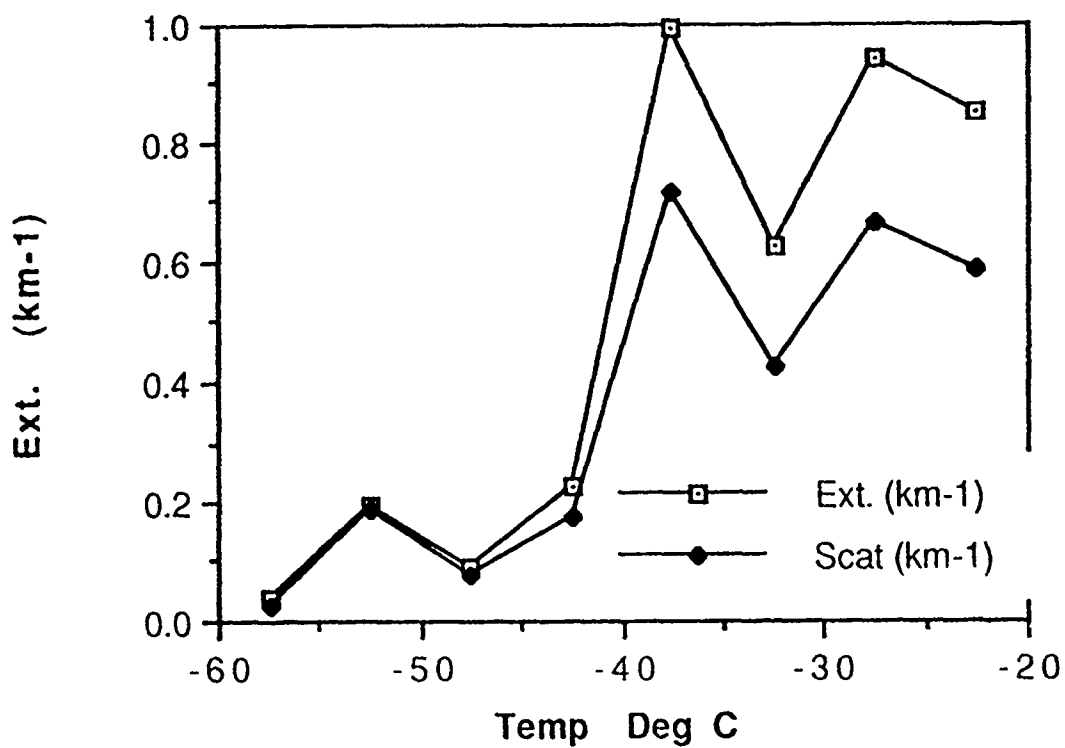


Figure 7. Modeled cirrus extinction (km⁻¹) as a function of temperature.

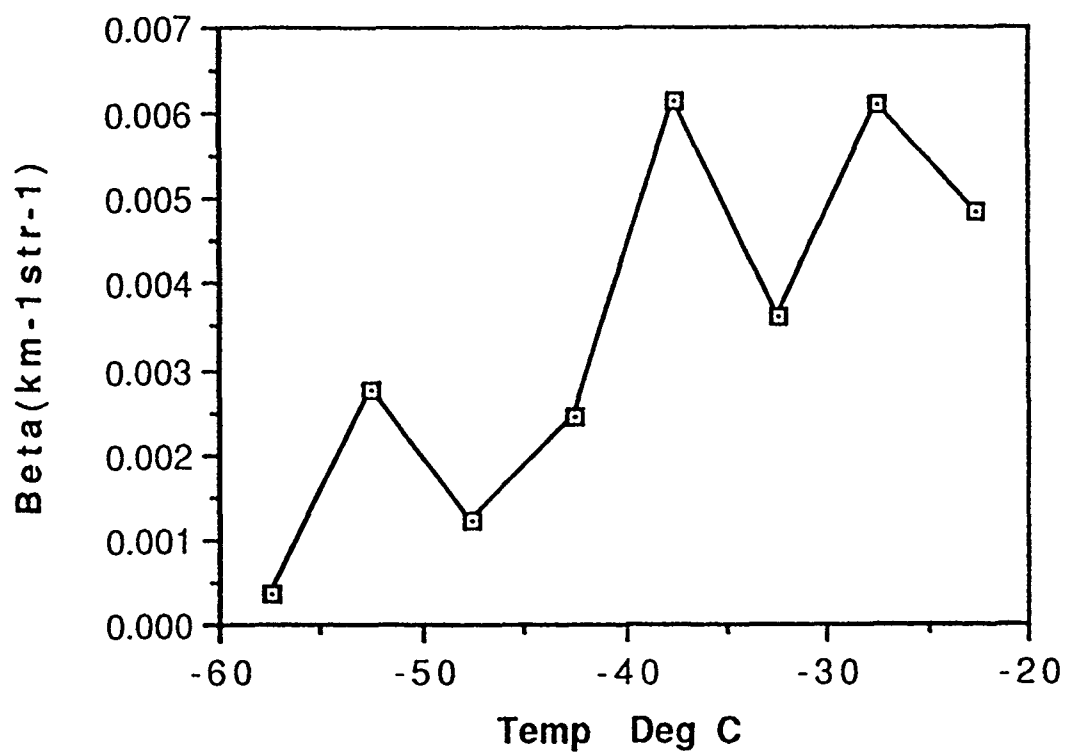


Figure 8. Modeled cirrus backscatter (km⁻¹sr⁻¹) as a function of temperature.

To obtain error estimates for the total measured horizontal wind, shot averaging within a 100 km square area with 1 km vertical resolution was performed, and typical profiles of temperature and relative humidity were assumed. Scenarios considered include clear skies (boundary layer winds only), water cloud only (cloud top winds only), cirrus clouds (upper level winds and boundary layer winds with reduced accuracy), and cirrus cloud over lower clouds (upper level winds and cloud top winds with reduced accuracy). We found that for the range of backscatter considered, in no case did the estimates of horizontal wind velocity error exceed 1 ms^{-1} , and often they were less than this. Therefore, we adopted a conservative approach and assigned a 1 ms^{-1} error to all cloud/aerosol scenarios. However, note that this value is representative of the best portion of the satellite swath whose total width is approximately 1800 km (i.e. halfway between the subtrack and the swath edge); the actual horizontal wind measurement error will increase near both the swath edge and the subtrack, which we discuss below.

5.3.2 Measurement Error as a Function of Distance to Subtrack

Recall that the simulated lidar wind measurements assume a conical scan, as in Figure 9, with a radius r . The lidar only measures wind in the radial direction and two shot averaged measurements are needed, one in the forward direction V_f and one in the backward direction V_b , to define the total wind vector $V (V_{\parallel}, V_{\perp})$. We assume throughout that all measurement errors are unbiased and random with no correlations in the vertical or horizontal. If the measurement error on the radial velocity is δV_r , we wish to find the resulting error in $V (\delta V)$, and its dependence on the distance of the measurement to the subtrack line (d).

Projection of the true wind $(V_{\parallel}, V_{\perp})$ onto the forward and backward measurement direction results in the following transformation:

$$\begin{aligned} V_f &= V_{\parallel} \cos \alpha + V_{\perp} \sin \alpha \\ V_b &= -V_{\parallel} \cos \alpha + V_{\perp} \sin \alpha \end{aligned} \quad (5.3)$$

Solving for V_{\parallel} and V_{\perp} and assuming $\delta V_f = \delta V_b = \delta V_r$, the errors on the components of V are then:

$$\begin{aligned} \delta V_{\parallel} &= \delta V_r / (\sqrt{2} \cos \alpha) \\ \delta V_{\perp} &= \delta V_r / (\sqrt{2} \sin \alpha) \end{aligned} \quad (5.4)$$

The total error is then

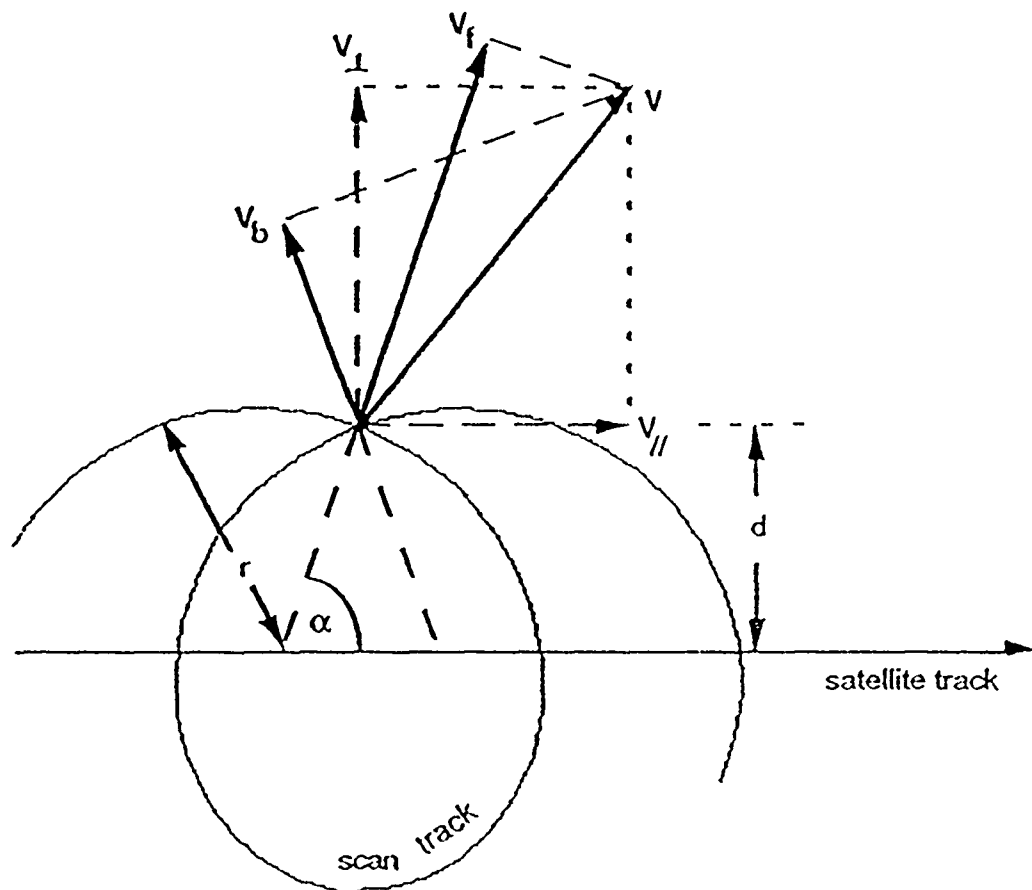


Figure 9. Schematic diagram of lidar wind measurement.

$$\begin{aligned}\delta V &= \sqrt{\delta V_{\parallel}^2 + \delta V_{\perp}^2} = \delta V_r / (\sqrt{2} \sin \alpha \cos \alpha) \\ &= \frac{r^2}{d\sqrt{2(r^2 - d^2)}} \delta V_r\end{aligned}\quad (5.5)$$

The minimum is $\delta V = \sqrt{2}\delta V_r$ at $d = r/\sqrt{2}$, i.e. at 45 degrees. Figure 10 shows the error amplification factor $\delta V/\delta V_r$ in terms of d/r .

We apply this analysis to the specific configuration used in this experiment to obtain values of the relevant parameters. Recall that the 1 ms^{-1} error value previously derived from the lidar simulation model was for the total wind error at the best point in the satellite swath. This corresponds to an error in the radial velocity measurement of $.707 \text{ ms}^{-1}$. Table 7 contains the appropriate parameters for the simple lidar experiment as a function of distance to the satellite subtrack (or alternatively, n , the scan position index). Amp is the error amplification factor for the total measured wind vector, given by $\text{Amp} = (\sqrt{2}\sin \alpha \cos \alpha)^{-1}$. Note that nadir scan data are included but not used during the actual data simulation.

Table 7. Amplification in Radial Wind Error vs. Distance to Subtrack for current OSSE.

Scan Position(n)	d(km)	d/r	α (degrees)	Error Amplification
1	-628.3	-0.70	-44.3	-1.41
2	-375.8	-0.42	-24.7	-1.86
3	-177.9	-0.20	-11.4	-3.65
4	0.	0.	0.	-
5	177.9	0.20	11.4	3.65
6	375.8	0.42	24.7	1.86
7	628.3	0.70	44.3	1.41

As the table indicates, the SSM/T scan positions correspond to data only from the inner half of the satellite swath, with the largest measurement errors occurring for measurements directly on either side of the subtrack line.

The amplification factor shown above affects the measured components of the wind differently at any given point in time depending on the current orientation of the satellite subtrack with respect to lines of latitude and longitude. The magnitude of the errors in the measured along and cross track wind components (eqn. 5.4) depend only on scan position. However, the along and cross track

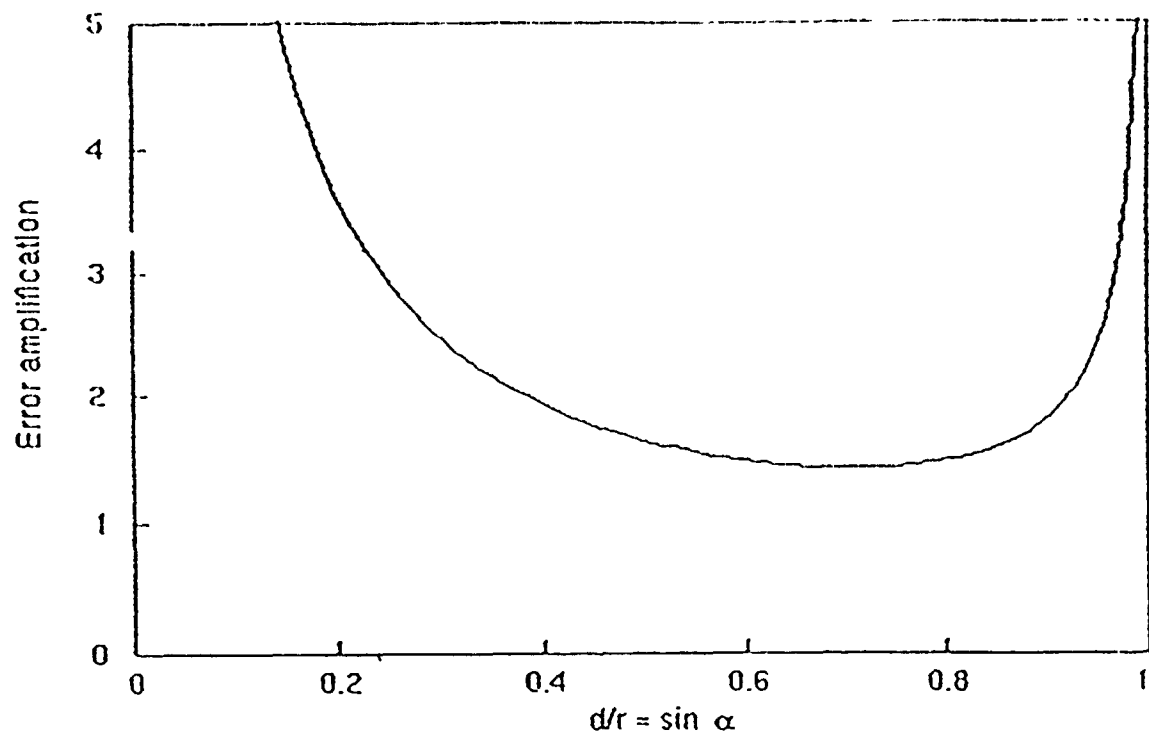


Figure 10. Error amplification factor in terms of distance to satellite subtrack.

direction vectors are constantly updated throughout the satellite orbit to account for the changing satellite path. For example, at lower latitudes the satellite cross track direction will be nearly parallel to latitude lines, while near the poles the cross track direction will be roughly parallel to meridians. Thus, random errors of the proper size for V_{\parallel} and V_{\perp} are generated and then are transformed to u and v measurement errors which are added to the exact components sampled previously from the nature run.

6. IMPACT RESULTS

Evaluation of the OSSE impact results is based on examination of synoptic maps, the time evolution of analysis and forecast error, the vertical distribution of analysis and forecast error, and averaging of forecast error for forecasts initialized at days 3, 5, and 7 of the assimilation period. The meteorological fields which are used in the evaluation include the 500 hPa geopotential height, 850 hPa vector and zonal winds, and the 850 hPa relative humidity. Finally, the scaled down lidar results are compared to our previous WINDSAT results.

6.1 Synoptic Maps

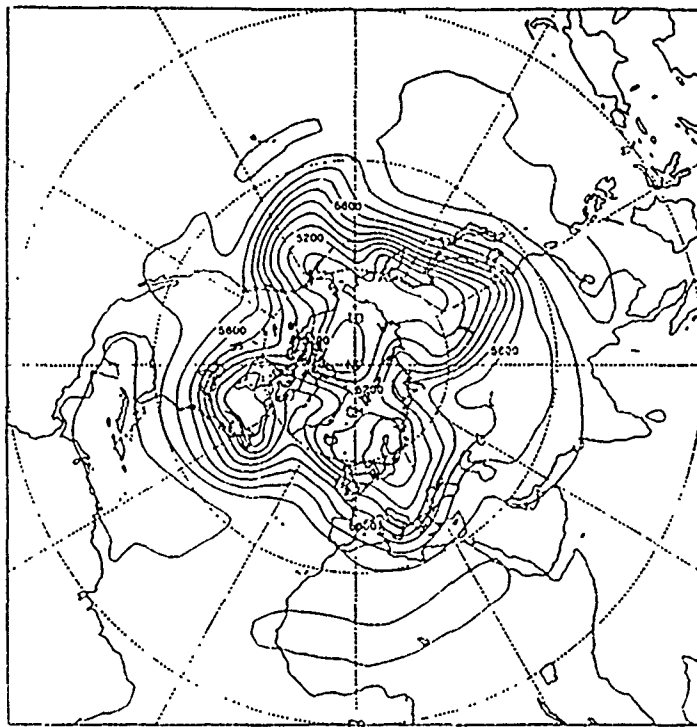
6.1.1 500 hPa Geopotential Height Analysis and Forecast

Figures 12 and 13 contain the height field analysis and analysis error, and the 48 h forecast and forecast error at 500 hPa for both the CONTROL and LIDAR experiments valid at 0000 UTC 23 November 1979. For comparison, the corresponding Nature fields are shown in figure 11.

In the northern hemisphere the analyses are nearly identical, with little impact on the dominant wave number 4 pattern. Error magnitudes are generally less than 40 m for both experiments. One location where the lidar data seems to have had an impact is near 110°W where the negative errors of 780 m in CONTROL are reduced to less than 40 m.

The southern hemisphere shows a much stronger impact of the lidar data, with most impact seen south of 50°S where the jet stream is located. For example, the broad trough between 90°W and 150°W is better analyzed in LIDAR. In this region positive errors are reduced from approximately 120-160 m to 40-80 m, while negative errors are reduced from about 120 m to 40 m. Similarly, the closed low near 90°E , 60°S which is analyzed 160 m too high and that near 30°E , 60°S which is too high by 120 m in CONTROL are both better analyzed in LIDAR, with errors reduced to 40 m and 80 m, respectively.

a.



b.

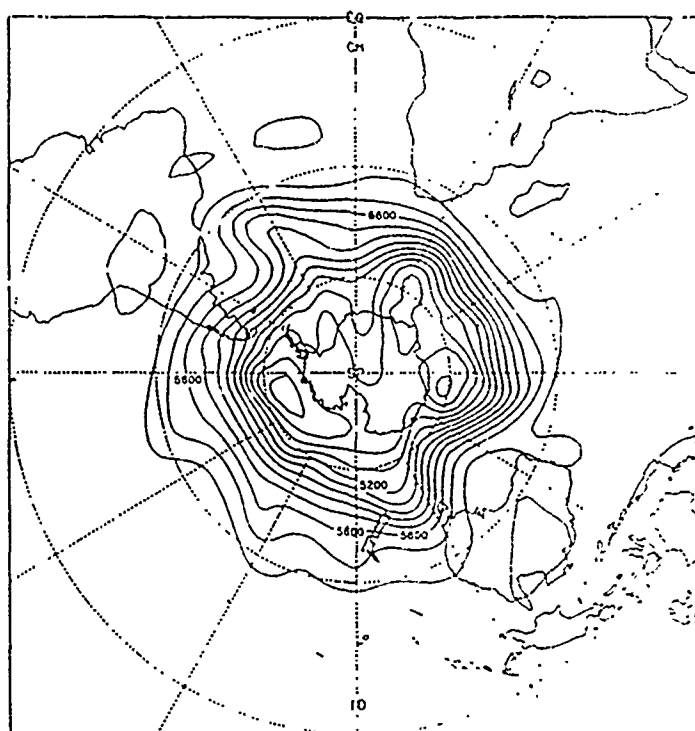
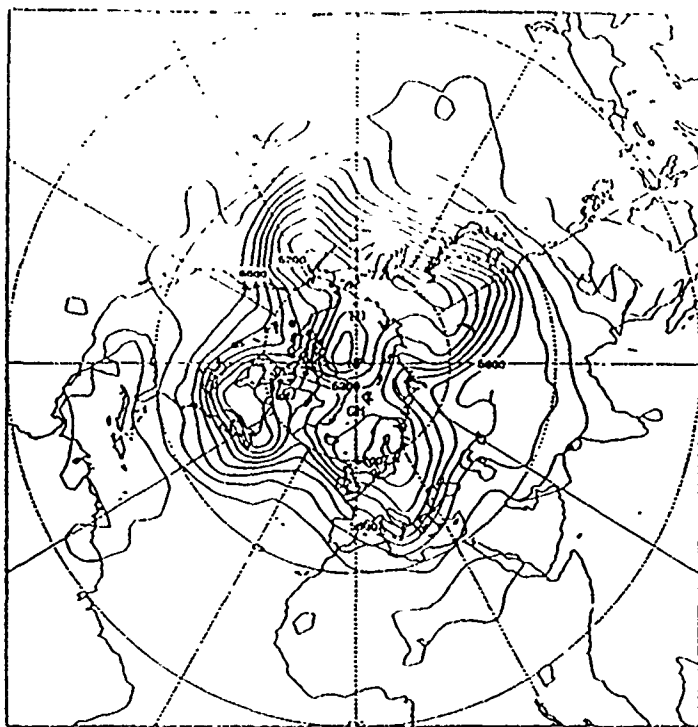


Figure 11. Nature 500 hPa geopotential height valid 00 UTC 23 November 1979.
(a) Northern hemisphere, (b) Southern hemisphere. Contour interval is 80 m.

a.



b.

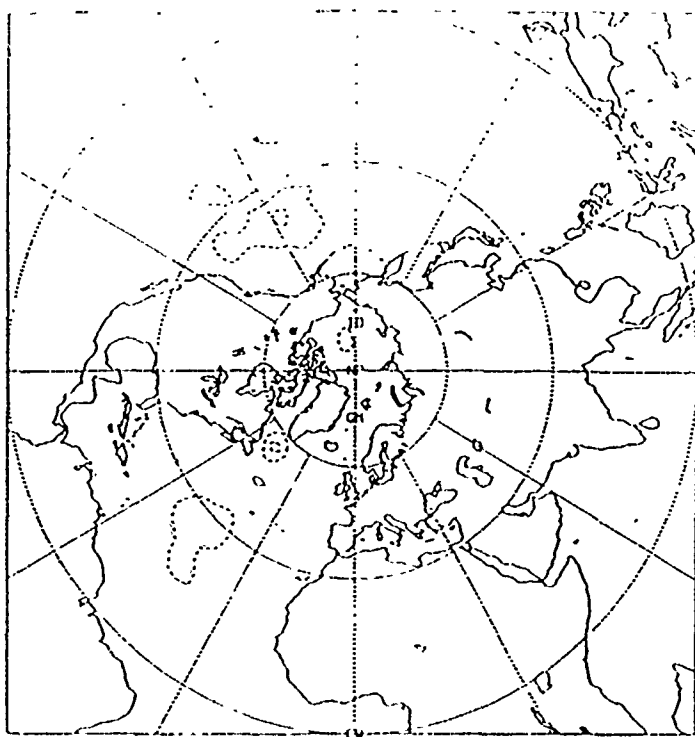
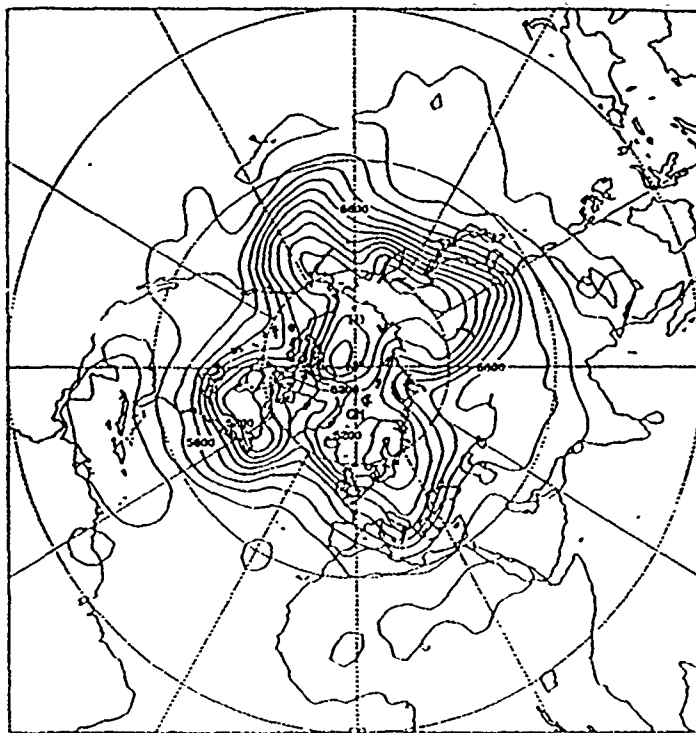


Figure 12 500 hPa geopotential height analysis valid 00 UTC 23 November 1979. (a),(b) CONTROL analysis and analysis error, (c),(d) LIDAR analysis and analysis error for the northern hemisphere. Corresponding southern hemisphere plots are in (e)-(h), respectively. Contour interval is 80 m for analyses, and 40 m for analysis errors. (Continued . . .)

c.



d.

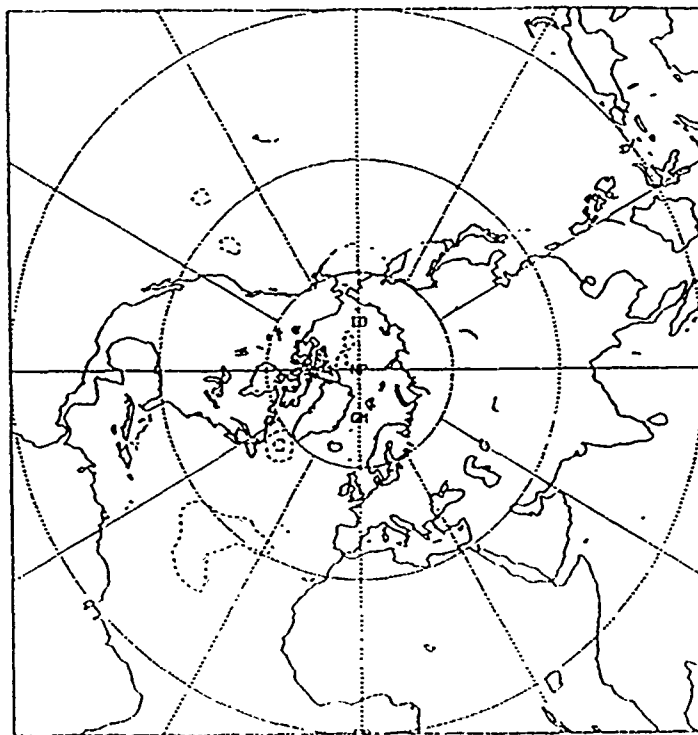


FIGURE 2. 500 hPa geopotential height analysis valid 00 UTC 23 November 1979. (a),(b) CONTROL analysis and analysis error, (c),(d) LIDAR analysis and analysis error for the northern hemisphere. Corresponding southern hemisphere plots are in (e)-(h), respectively. Contour interval is 80 m for analyses, and 40 m for analysis errors. (Continued . . .)

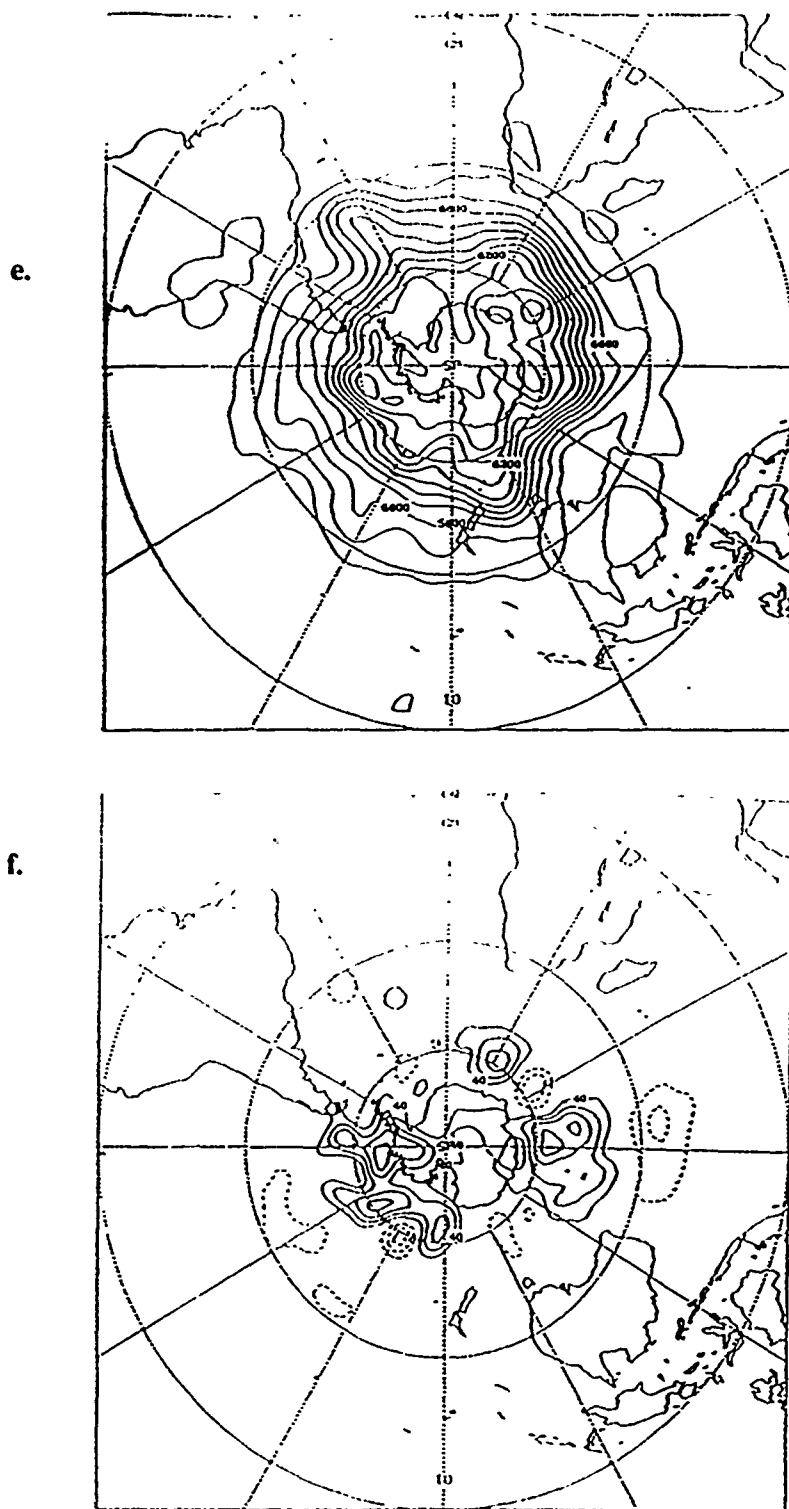
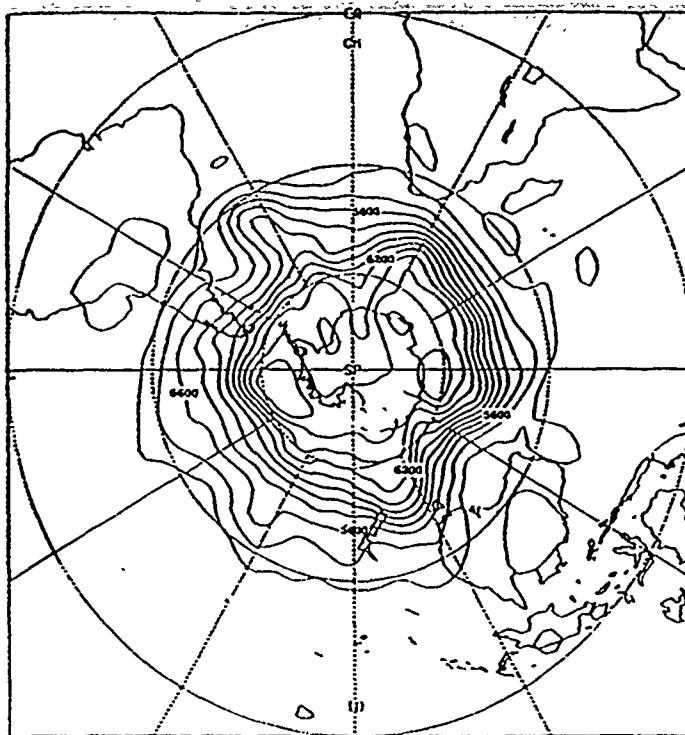


Figure 12. 500 hPa geopotential height analysis valid 00 UTC 23 November 1979. (a),(b) CONTROL analysis and analysis error, (c),(d) LIDAR analysis and analysis error for the northern hemisphere. Corresponding southern hemisphere plots are in (e)-(h), respectively. Contour interval is 80 m for analyses, and 40 m for analysis errors. (Continued . . .)

g.



h.

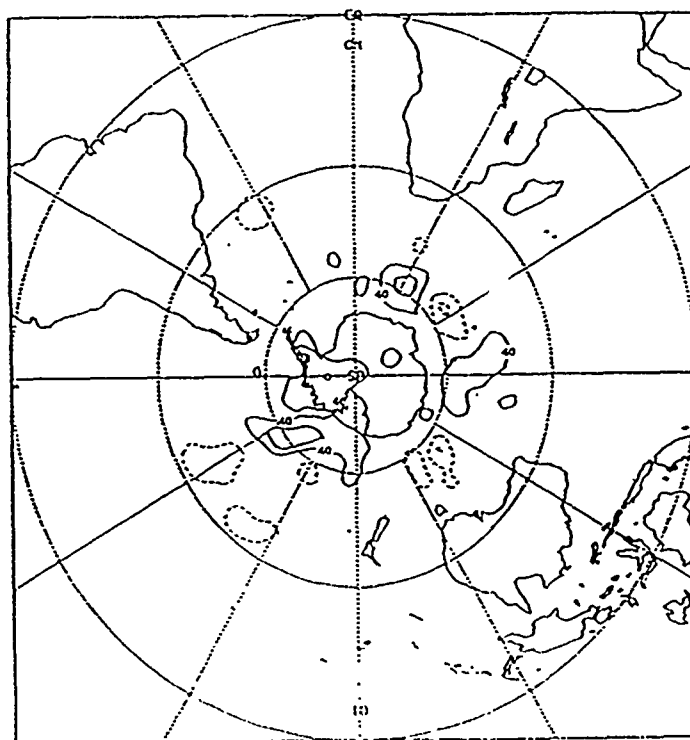
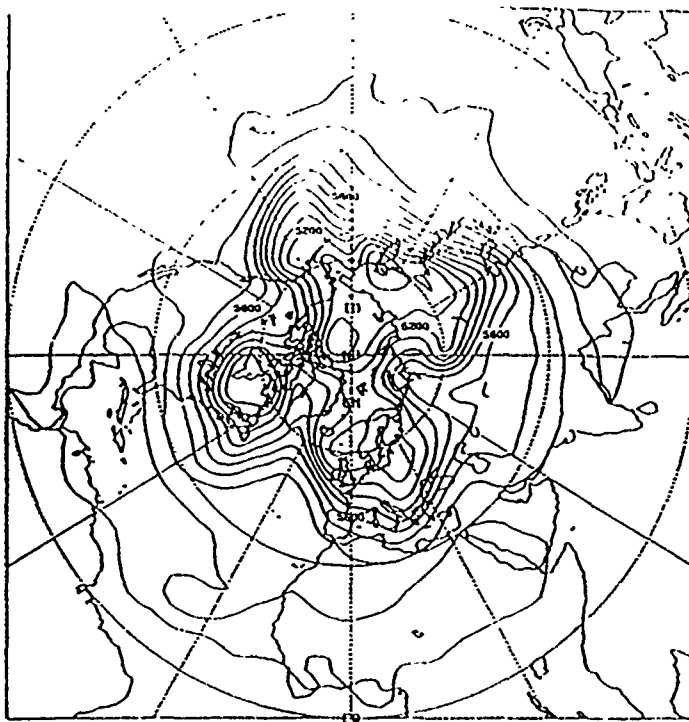


Figure 12. 500 hPa geopotential height analysis valid 00 UTC 23 November 1979. (a),(b) CONTROL analysis and analysis error, (c),(d) LIDAR analysis and analysis error for the northern hemisphere. Corresponding southern hemisphere plots are in (e)-(h), respectively. Contour interval is 80 m for analyses, and 40 m for analysis errors.

a.



b.

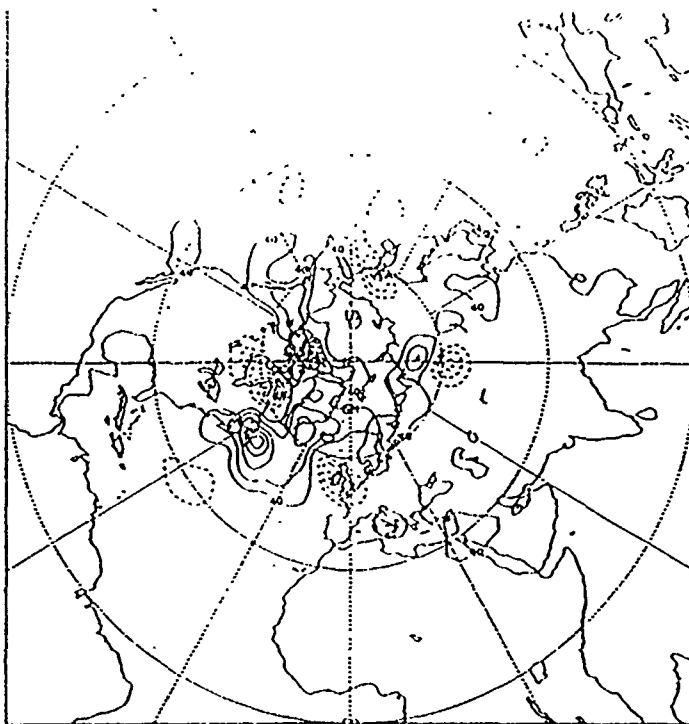
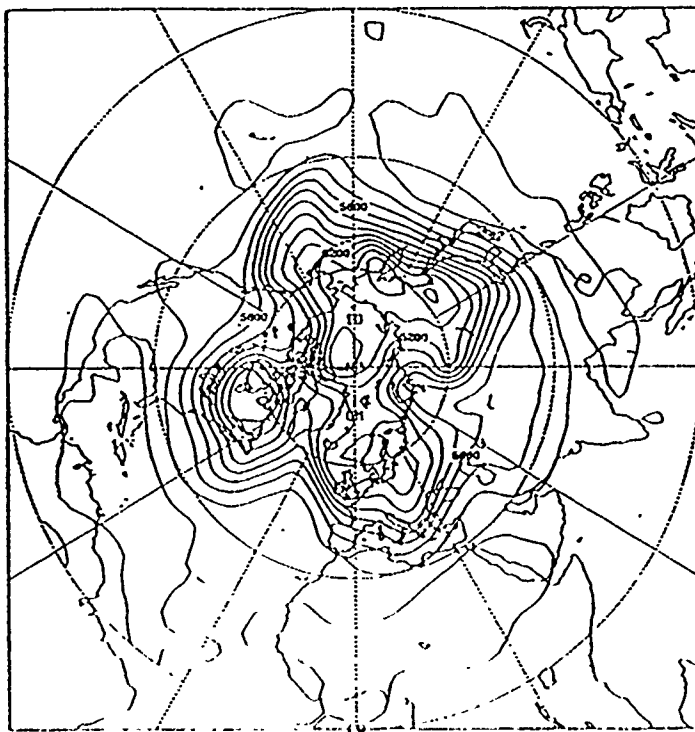


Figure 13. 500 hPa 48 hour geopotential height analysis valid 00 UTC 23 November 1979. (a),(b) CONTROL analysis and analysis error, (c),(d) LIDAR analysis and analysis error for the northern hemisphere. Corresponding southern hemisphere plots are in (e)-(h), respectively. Contour interval is 80 m for analyses, and 40 m for analysis errors. (Continued . . .)

c.



d.

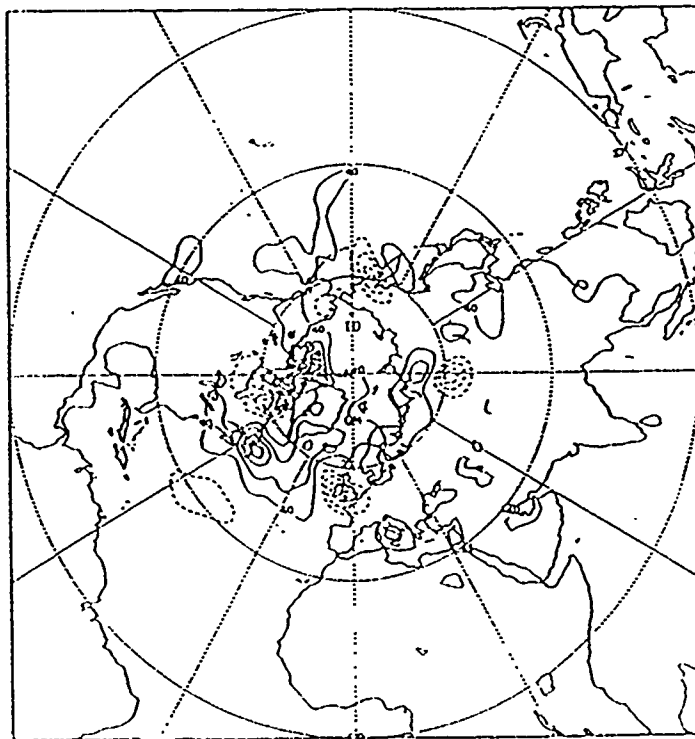
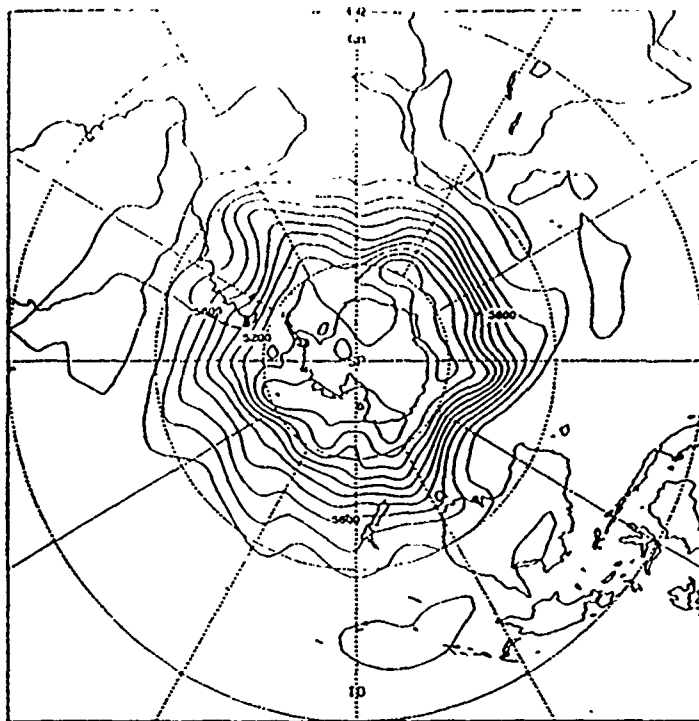


Figure 13. 500 hPa 48 hour geopotential height analysis valid 00 UTC 23 November 1979. (a),(b) CONTROL analysis and analysis error, (c),(d) LIDAR analysis and analysis error for the northern hemisphere. Corresponding southern hemisphere plots are in (e)-(h), respectively. Contour interval is 80 m for analyses, and 40 m for analysis errors. (Continued . . .)

e.



f.

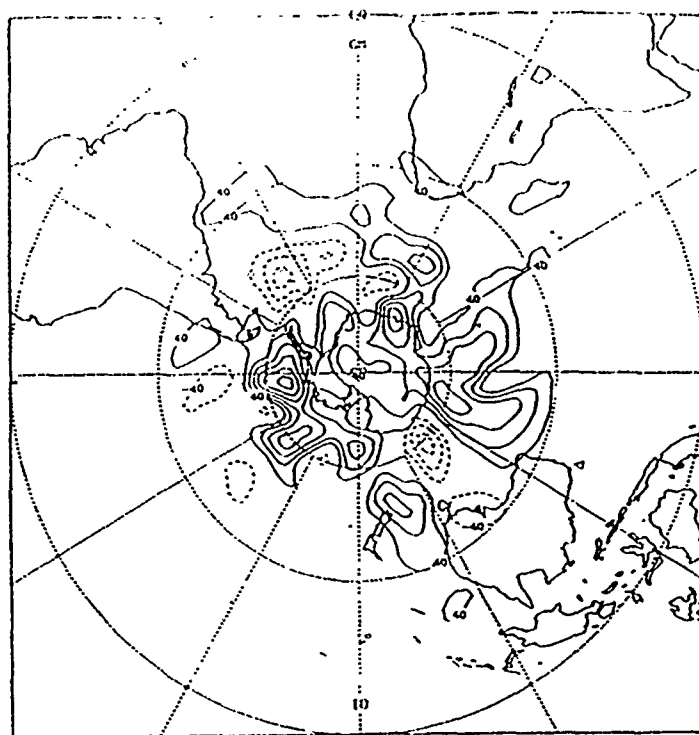
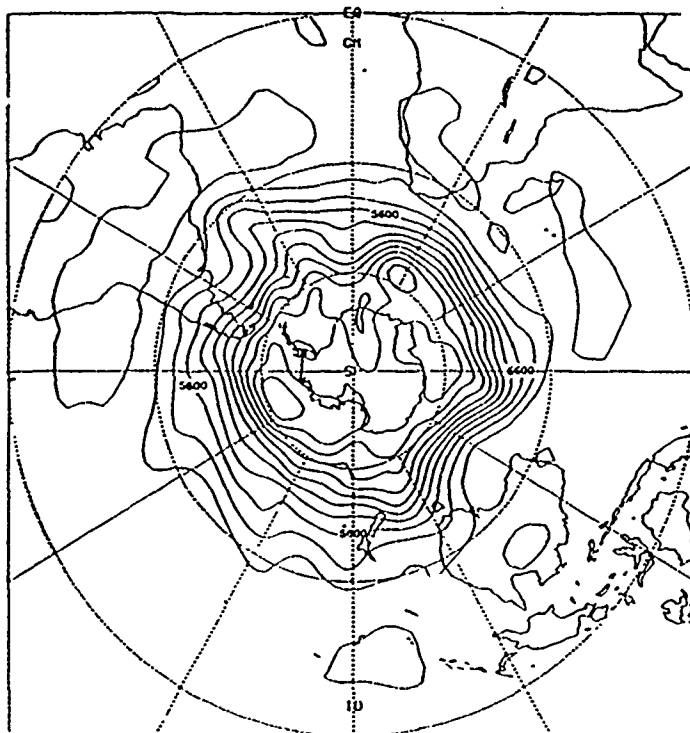


Figure 13. 500 hPa 48 hour geopotential height analysis valid 00 UTC 23 November 1979. (a),(b) CONTROL analysis and analysis error, (c),(d) LIDAR analysis and analysis error for the northern hemisphere. Corresponding southern hemisphere plots are in (e)-(h), respectively. Contour interval is 80 m for analyses, and 40 m for analysis errors. (Continued . . .)

g.



h.

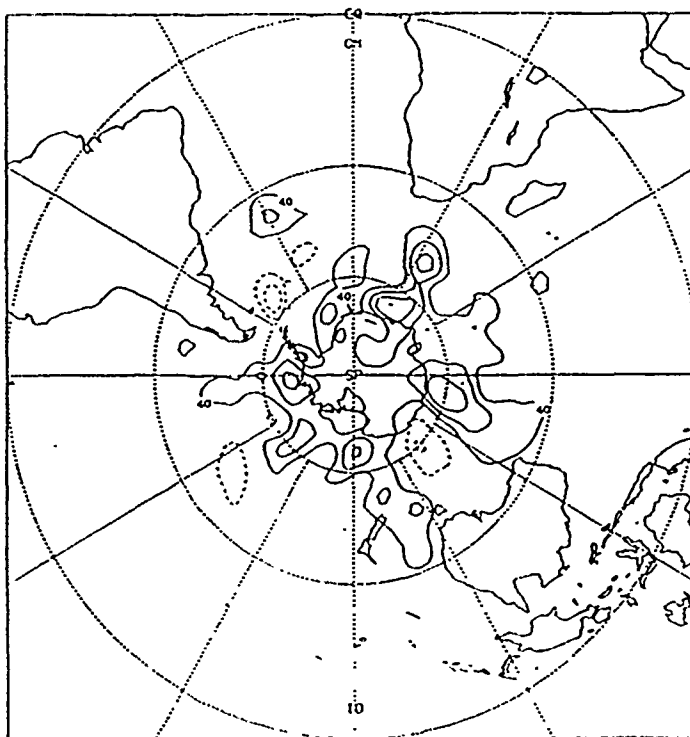


Figure 13. 500 hPa 48 hour geopotential height analysis valid 00 UTC 23 November 1979. (a),(b) CONTROL analysis and analysis error, (c),(d) LIDAR analysis and analysis error for the northern hemisphere. Corresponding southern hemisphere plots are in (e)-(h), respectively. Contour interval is 80 m for analyses, and 40 m for analysis errors.

The forecast fields valid at the same time show that the DWL data has little impact in the northern hemisphere, which reflects the fact that both forecasts started with very similar initial states.

However in the southern hemisphere there is a very noticeable impact poleward of 60°S. In general, errors are reduced in magnitude from about 120-160 m in CONTROL to roughly 40-80 m in LIDAR. It is also noteworthy that addition of the lidar data has not improved phase errors in the forecast since the same positive/negative pattern of errors is retained in both experiments. For example, the trough/ridge sequence south and east of Australia in Nature is moved too slowly in both CONTROL and LIDAR forecasts resulting in a similarly shaped error pattern. Since the same model is used in both forecast runs, errors resulting from inaccuracies in the model physical parameterizations would also be present in both forecasts.

6.1.2 850 hPa Vector Wind Analysis and Forecast

Figure 14 contains the 850 hPa horizontal wind speed analysis and vector wind error magnitudes for analysis and 48 h forecast, while figure 15 contains the actual horizontal wind vector and wind vector error fields for analyses and forecasts valid at the same time, 00 UTC 23 November.

For the analyses most of the data impact is seen in the southern hemisphere, but one area east of Newfoundland associated with a trough over eastern North America also shows an improvement. In this region the vector wind error maximum magnitude is reduced from greater than 30 ms⁻¹ to approximately 20 ms⁻¹.

In the southern hemisphere the impact is more obvious. Large improvements are seen in two large areas, one over the South Pacific Ocean from the dateline to South America near 60°S, the other over the southern Indian Ocean between 30°E and 90°E. In the Pacific much of this improvement is due to the closed cyclonic circulation near 60°S, 90°W which is much better analyzed in LIDAR. In the Indian Ocean an area of strong westerly winds at 850 hPa with some cyclonic curvature is poorly analyzed in CONTROL but much improved in LIDAR. In both instances areas of vector wind errors of 20-30 ms⁻¹ are often reduced to less

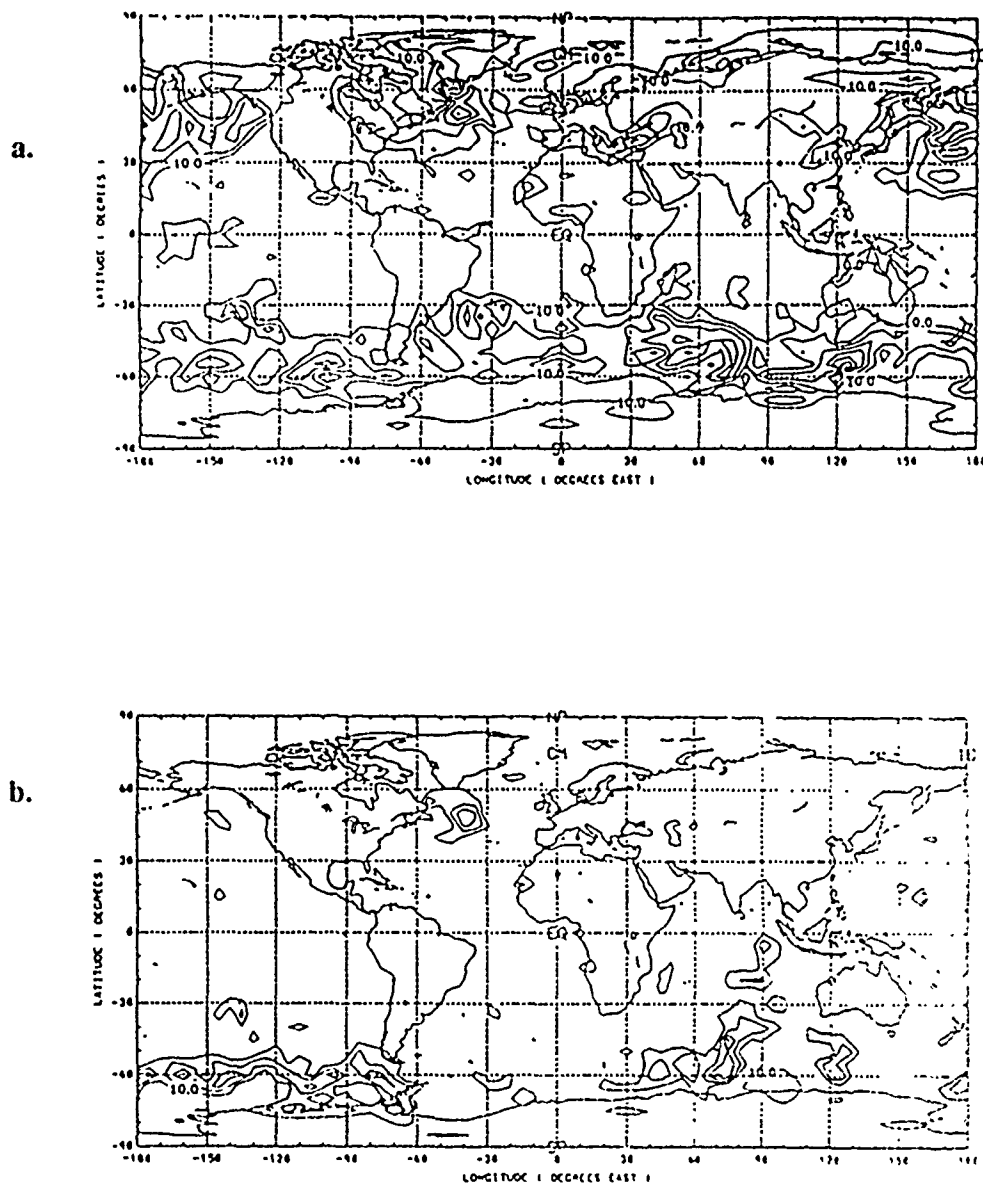


Figure 14. 850 hPa global horizontal wind speed analysis and vector wind error magnitude fields valid 00 UTC 23 November 1979. (a),(b) CONTROL analysis and analysis error, (c),(d) LIDAR analysis and analysis error. Corresponding 48 h forecast maps valid at the same time are in (e)-(h). Contour interval is 5 ms^{-1} starting at 10 ms^{-1} for wind speed, and starting at 5 ms^{-1} for the error maps. (Continued ...)

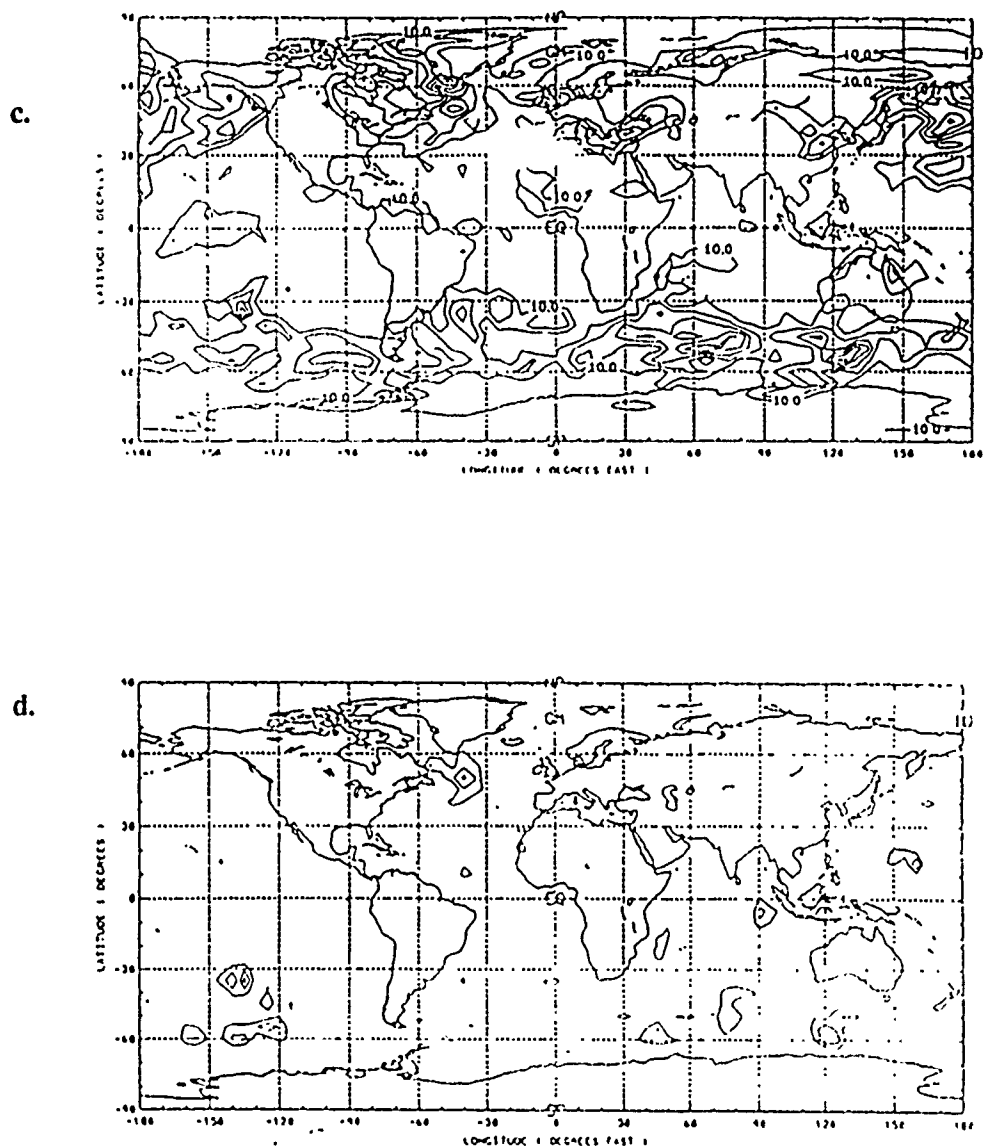


Figure 14. 850 hPa global horizontal wind speed analysis and vector wind error magnitude fields valid 00 UTC 23 November 1979. (a),(b) CONTROL analysis and analysis error, (c),(d) LIDAR analysis and analysis error. Corresponding 48 h forecast maps valid at the same time are in (e)-(h). Contour interval is 5 ms^{-1} starting at 10 ms^{-1} for wind speed, and starting at 5 ms^{-1} for the error maps. (Continued . . .)

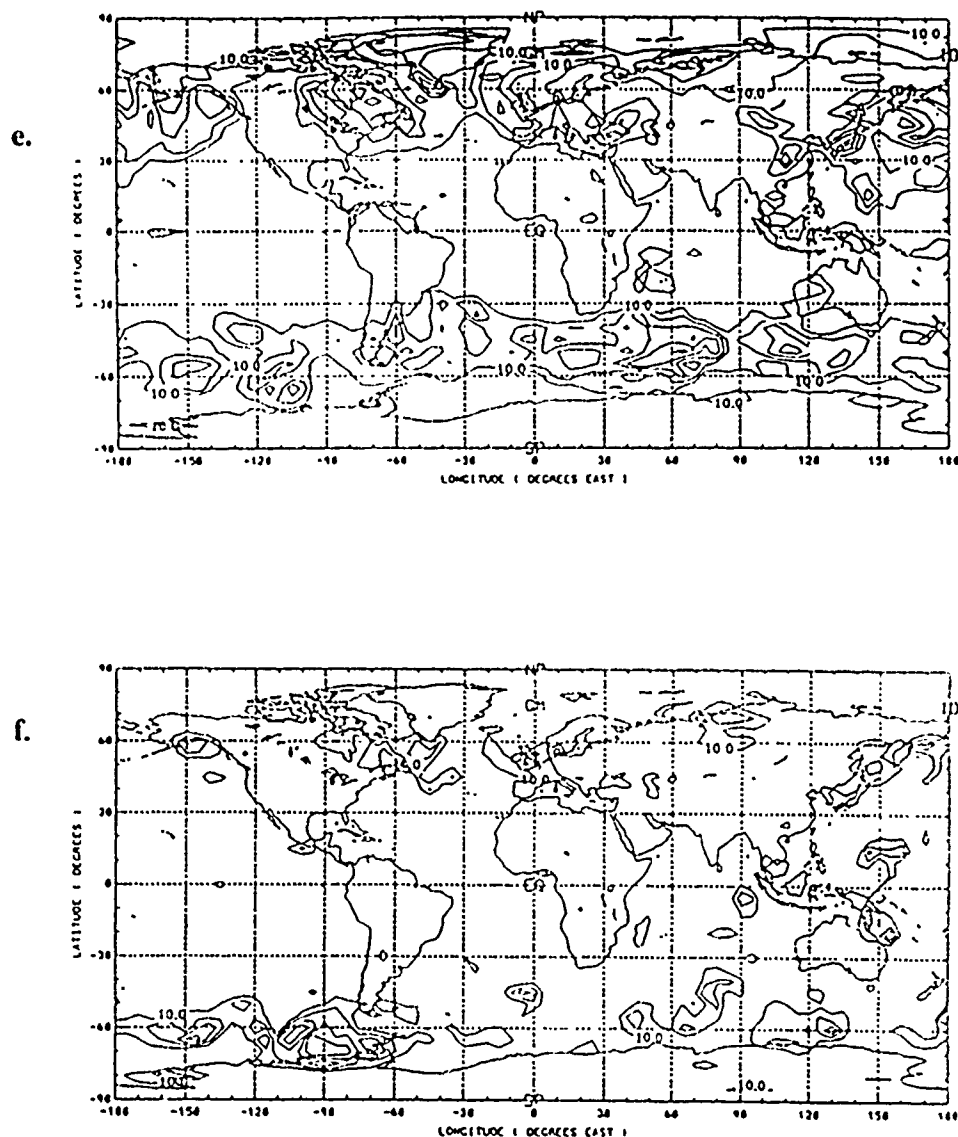


Figure 14. 850 hPa global horizontal wind speed analysis and vector wind error magnitude fields valid 00 UTC 23 November 1979. (a),(b) CONTROL analysis and analysis error, (c),(d) LIDAR analysis and analysis error. Corresponding 48 h forecast maps valid at the same time are in (e)-(h). Contour interval is 5 ms^{-1} starting at 10 ms^{-1} for wind speed, and starting at 5 ms^{-1} for the error maps. (Continued ...)

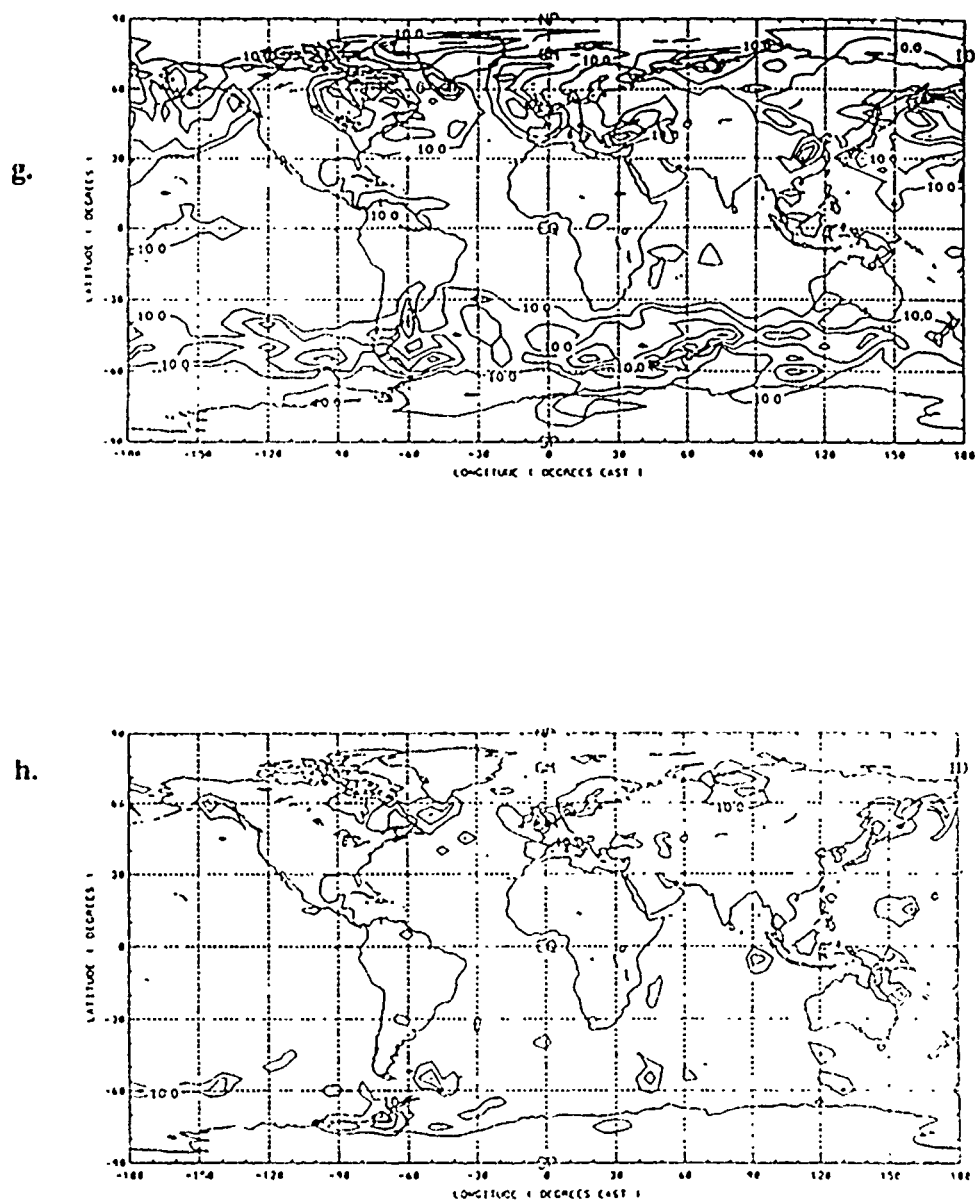


Figure 14 850 hPa global horizontal wind speed analysis and vector wind error magnitude fields valid 00 UTC 23 November 1979 (a),(b) CONTROL analysis and analysis error, (c),(d) LIDAR analysis and analysis error. Corresponding 48 h forecast maps valid at the same time are in (e)-(h). Contour interval is 5 ms^{-1} starting at 10 ms^{-1} for wind speed, and starting at 5 ms^{-1} for the error maps.

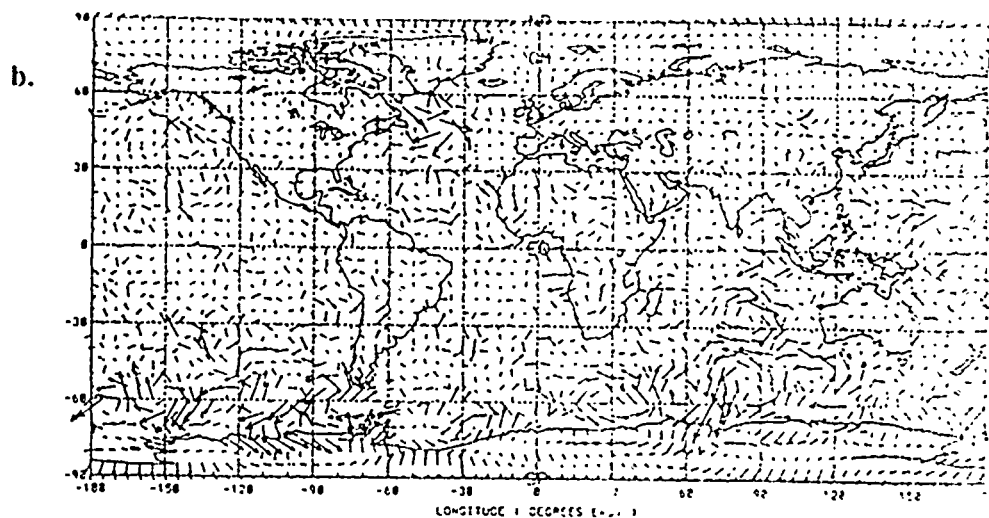
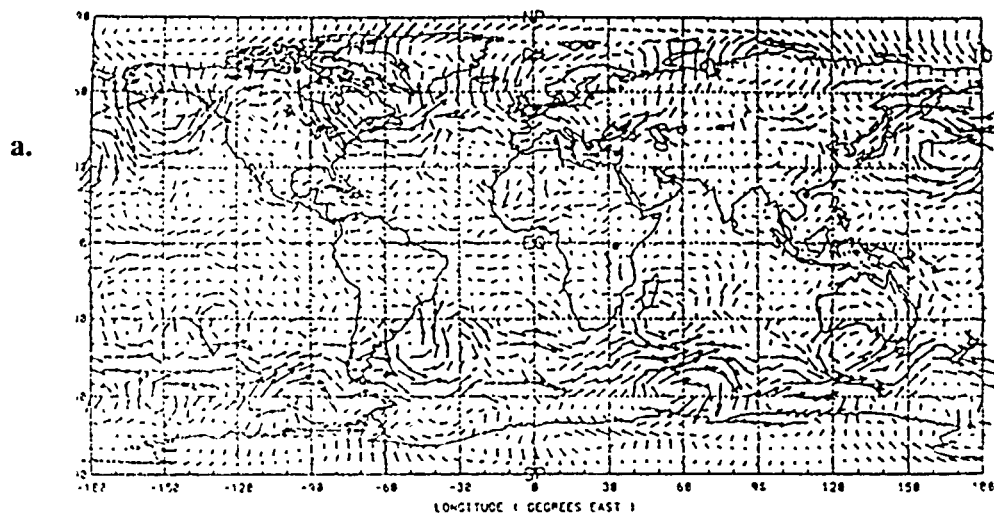


Figure 15. 850 hPa global horizontal wind vector analysis and analysis error valid 00 UTC 23 November 1979. (a),(b) CONTROL analysis and analysis error, (c),(d) LIDAR analysis and analysis error. Corresponding 48 h forecast maps valid at the same time are in (e)-(h). (Continued . . .)

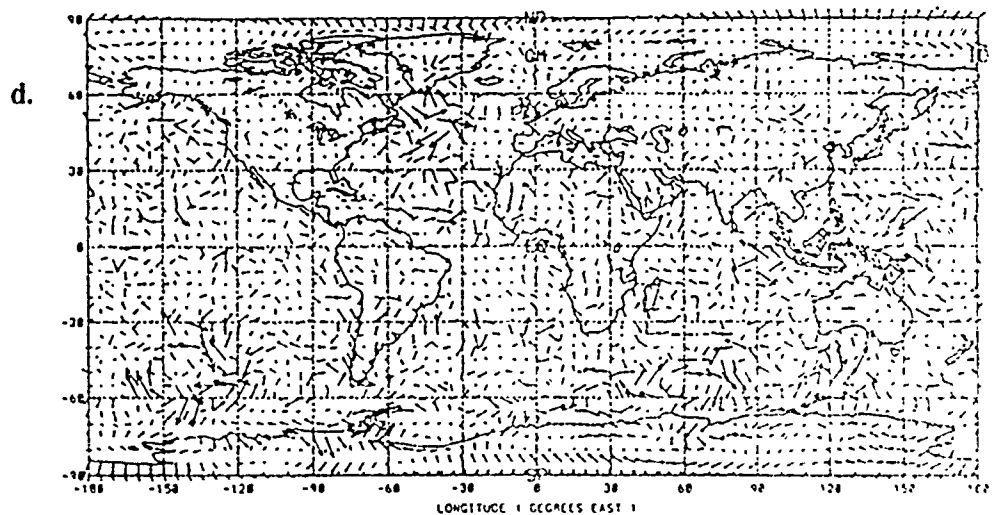
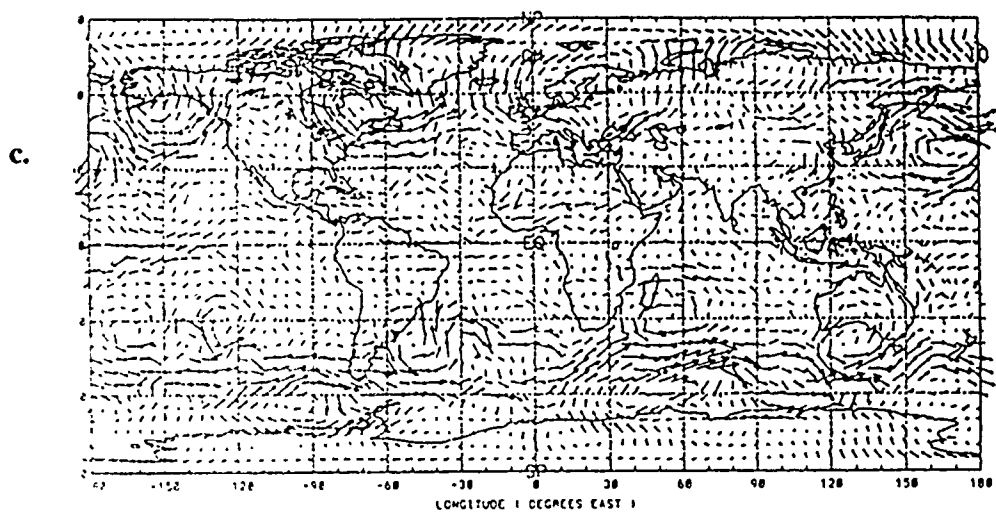


Figure 15 850 hPa global horizontal wind vector analysis and analysis error valid 00 UTC 23 November 1979. (a),(b) CONTROL analysis and analysis error, (c),(d) LIDAR analysis and analysis error. Corresponding 48 h forecast maps valid at the same time are in (e)-(h). (Continued . . .)

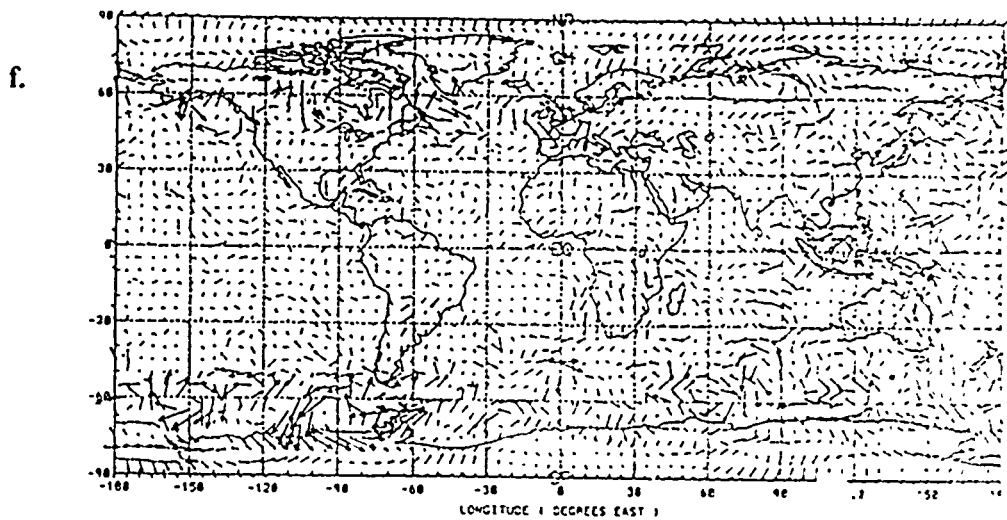
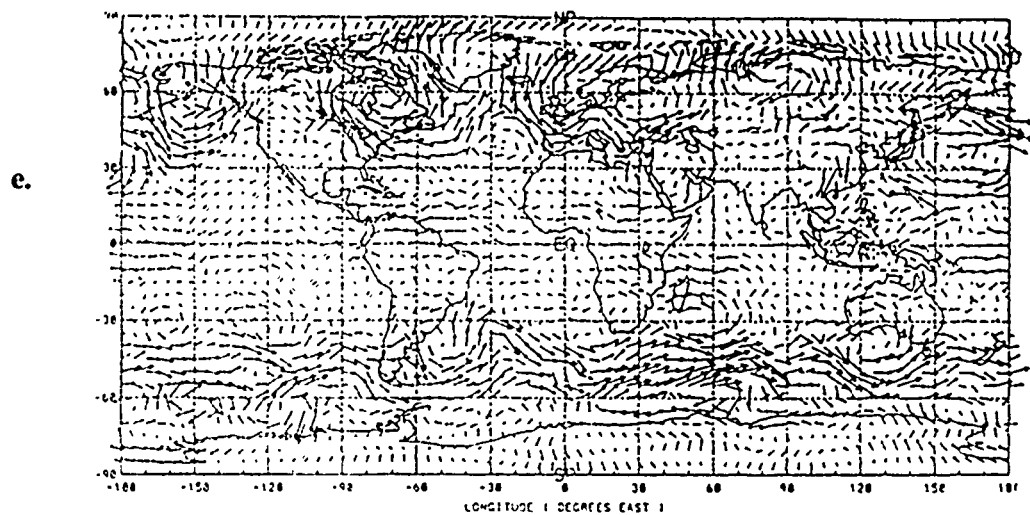


Figure 15. 850 hPa global horizontal wind vector analysis and analysis error valid 00 UTC 23 November 1979 (a),(b) CONTROL analysis and analysis error, (c),(d) LIDAR analysis and analysis error. Corresponding 48 h forecast maps valid at the same time are in (e)-(h). (Continued . . .)

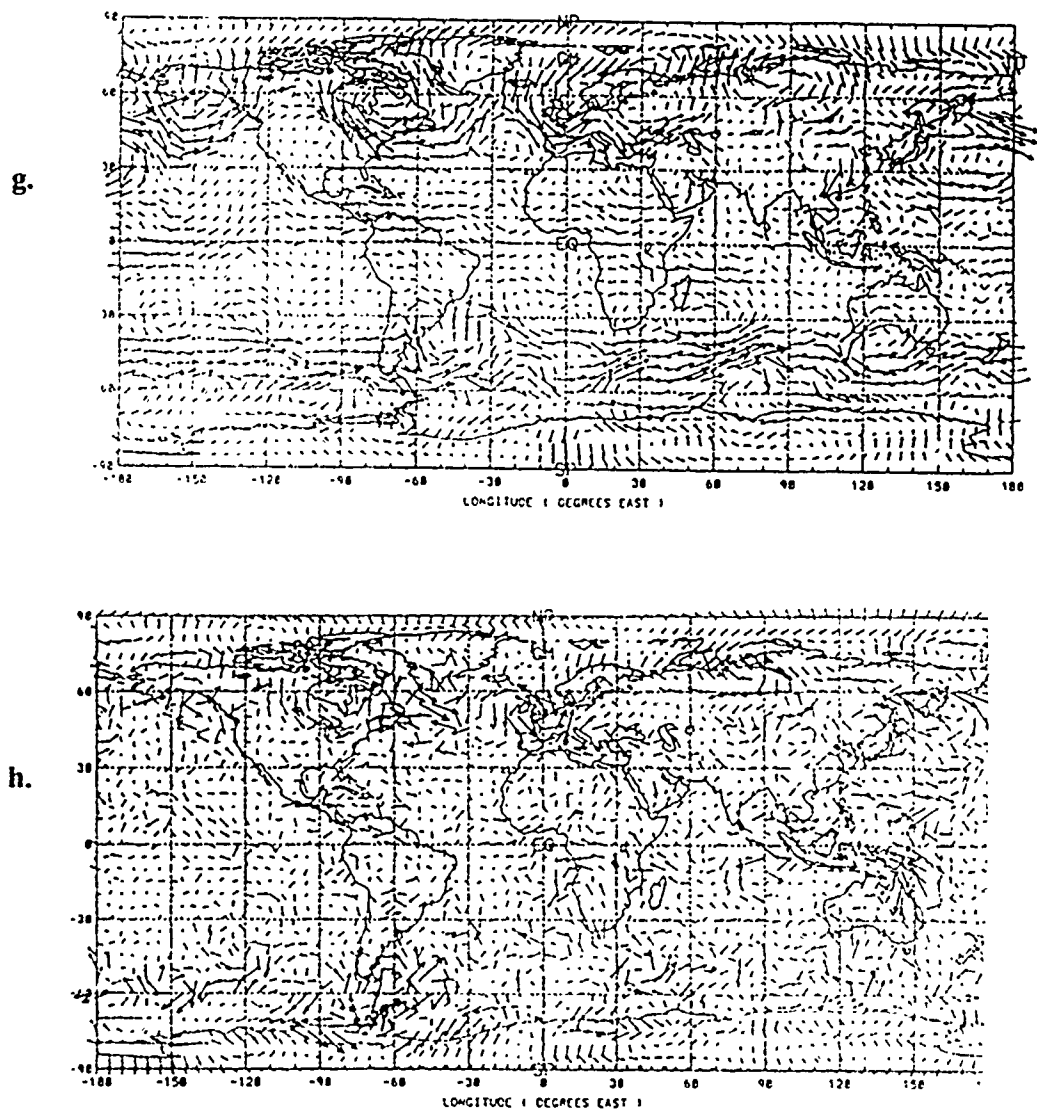


Figure 15 850 hPa global horizontal wind vector analysis and analysis error valid 00 UTC 23 November 1979 (a),(b) CONTROL analysis and analysis error, (c),(d) LIDAR analysis and analysis error. Corresponding 48 h forecast maps valid at the same time are in (e) (h).

than 10 ms^{-1} . Forecast maps show a similar pattern with impact concentrated in the same southern hemisphere locations. Interestingly, the CONTROL 48 h forecast error seen over the Indian Ocean is somewhat smaller in magnitude than that seen in the analysis valid at the same time. This is consistent with the fact that compared to other LIDAR 850 hPa wind forecasts, the error growth rate for the forecast initialized on 21 November is anomalously small, while coincidentally, the analysis error was increasing from 21 to 23 November (see figure 16).

6.1.3 850 hPa Relative Humidity Analysis and Forecast Error

Figure 16 contains the relative humidity analysis and 48 h forecast errors for both CONTROL and LIDAR again valid for 00 UTC 23 November 1979. As in the geopotential height fields, nearly all impact is seen in the southern hemisphere extratropics, south of 30°S . In particular, large areas of negative error in the south Pacific and Atlantic with levels greater than 50 percent are reduced in LIDAR analysis. In both experiments there seems to be a bias toward negative errors rather than positive. This may be a result of surface moisture parameterizations in the GSM physics package.

In the forecast maps, impact is also confined to the southern hemisphere with large improvement seen over the southern oceans and Antarctica. These results for the humidity analyses and forecasts are similar to those obtained in the WINDSAT OSSE and are consistent with the idea that improved specification (or prediction) of the horizontal wind field leads to a better analysis (or forecast) of a passive tracer like water vapor. In essence, the model humidity field quickly adjusts to the fields of mass and motion.

6.2 Analysis and Forecast Error as a Function of Time

6.2.1 500 hPa Geopotential Height rms Error

Figure 17 shows 500 hPa rms height errors of the 7 day analyses and forecasts for several experiments. Errors are shown for the globe as well as the northern hemisphere, southern hemisphere and tropical subregions. The experiments plotted are CONTROL and LIDAR, and for comparative purposes, the previously conducted STATSAT (control) and WINDSAT OSSEs.

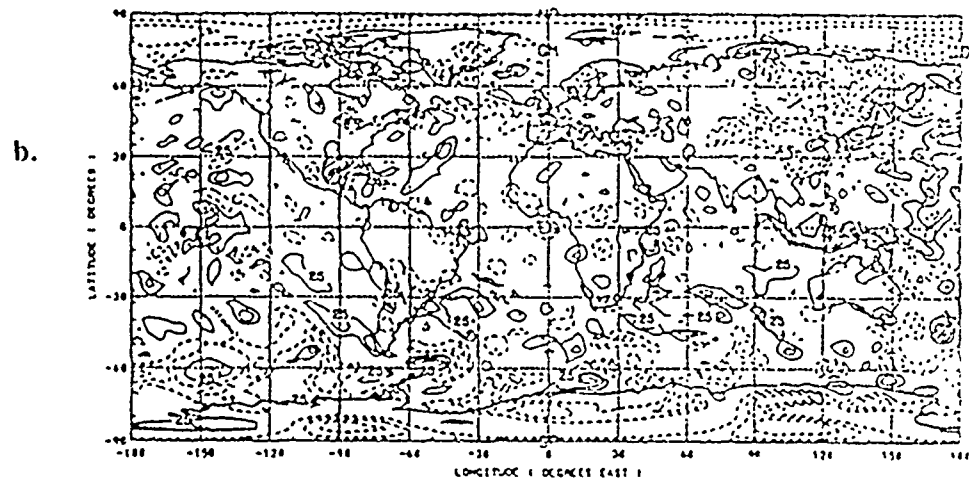
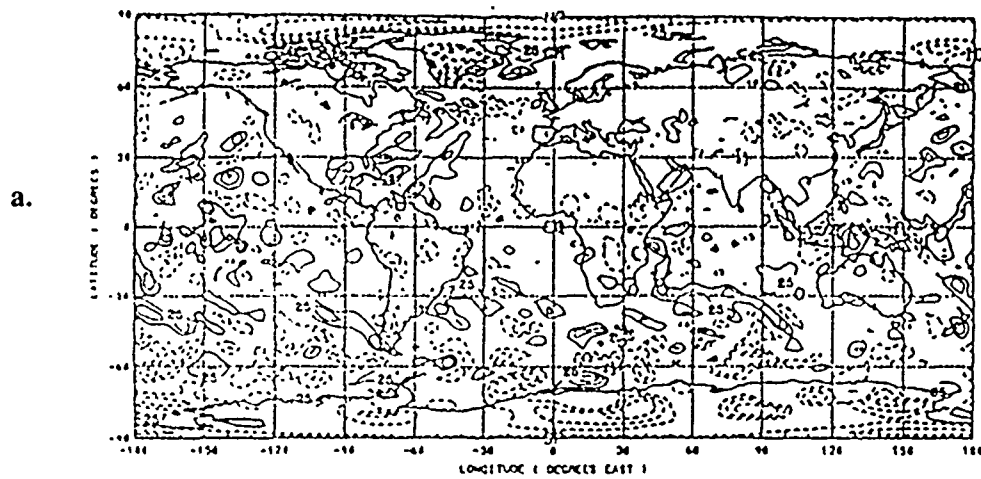
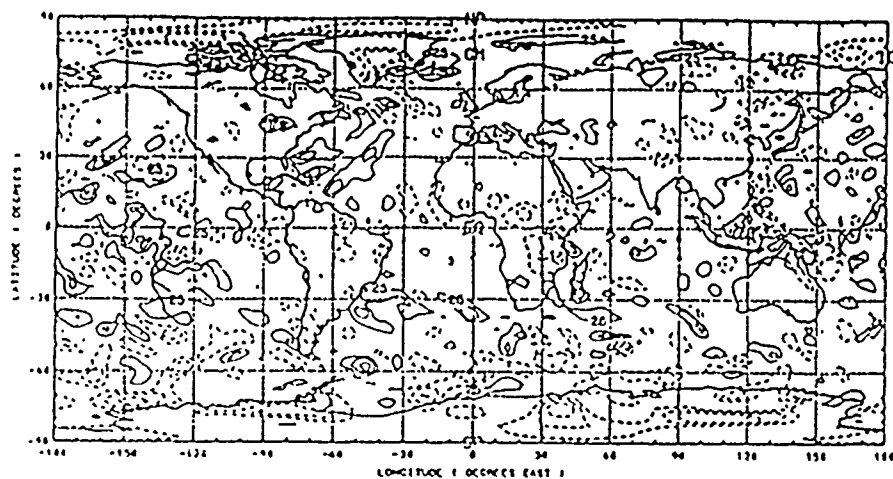


Figure 16. 850 hPa global relative humidity analysis error and 48 h forecast error valid 00 UTC 23 November 1979. (a),(b) CONTROL analysis and forecast error, (c),(d) LIDAR analysis error and forecast error. Contour interval is 25 percent with zero line omitted. Negative values are dashed. (Continued . . .)

c.



d.

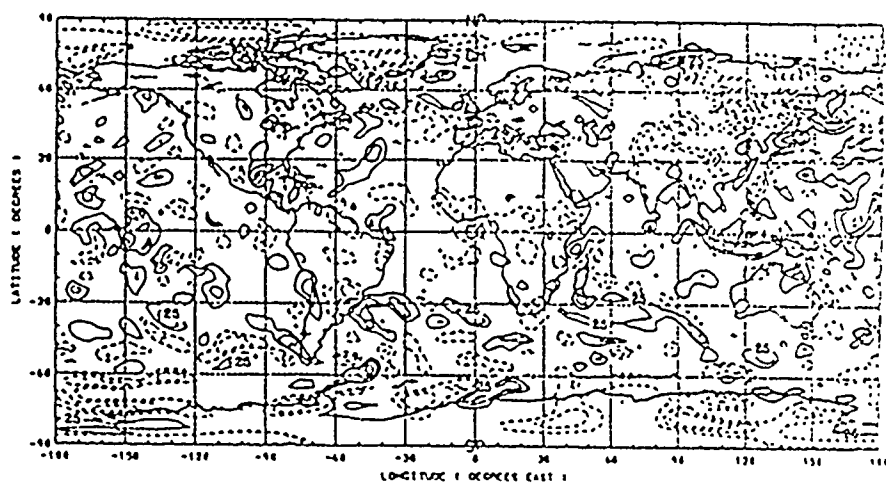
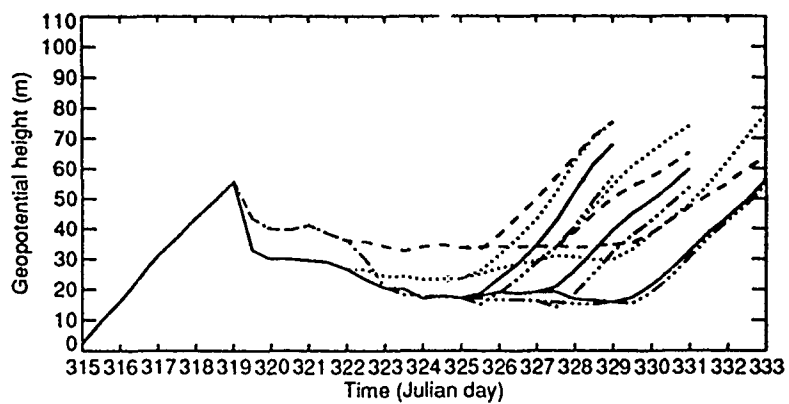


Figure 16. 850 hPa global relative humidity analysis error and 48 h forecast error valid 00 UTC 23 November 1979. (a),(b) CONTROL analysis and forecast error, (c),(d) LIDAR analysis error and forecast error. Contour interval is 25 percent with zero line omitted. Negative values are dashed.

a.



b.

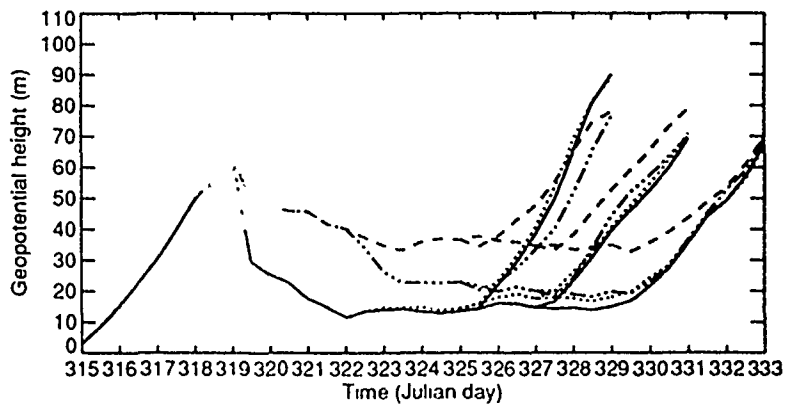
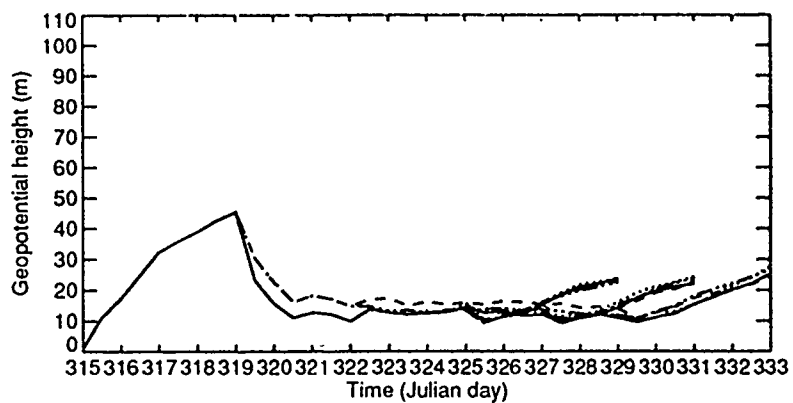


Figure 17. 500 hPa geopotential height analysis and forecast errors averaged horizontally. (a) Global, (b) Northern hemisphere, (c) Tropics, (d) Southern hemisphere. Shown are CONTROL (dot), LIIDAR (solid), STATSAT (dash), and WINDSAT (dash-dot-dot-dot). (Continued . . .)

c.



d.

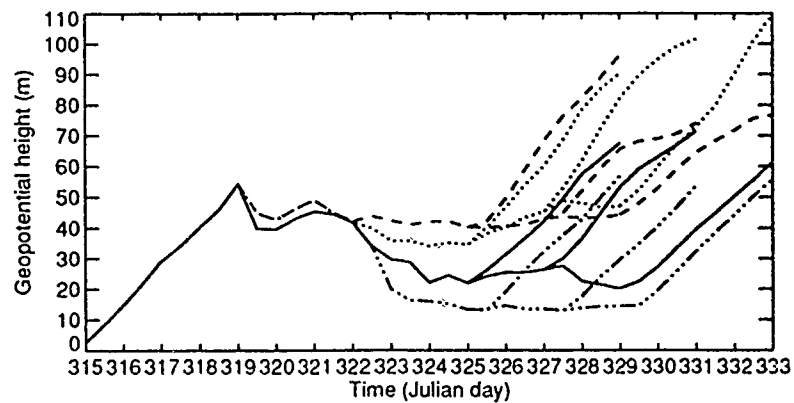


Figure 17. 500 hPa geopotential height analysis and forecast errors averaged horizontally. (a) Global, (b) Northern hemisphere, (c) Tropics, (d) Southern hemisphere. Shown are CONTROL (dot), LIDAR (solid), STATSAT (dash), and WINDSAT (dash-dot-dot-dot).

With the exception of the tropics, where height and wind fields are not geostrophically coupled, we see that, relative to CONTROL, LIDAR reduces height analysis errors substantially. This is most dramatic in the southern hemisphere where the height error is reduced from approximately 45 m to 20-25 m. In the northern hemisphere where the conventional observation network is more extensive the improvement is smaller - from 15-20 m to about 12 m. Globally the reduction is from 25-30 m to roughly 12 m.

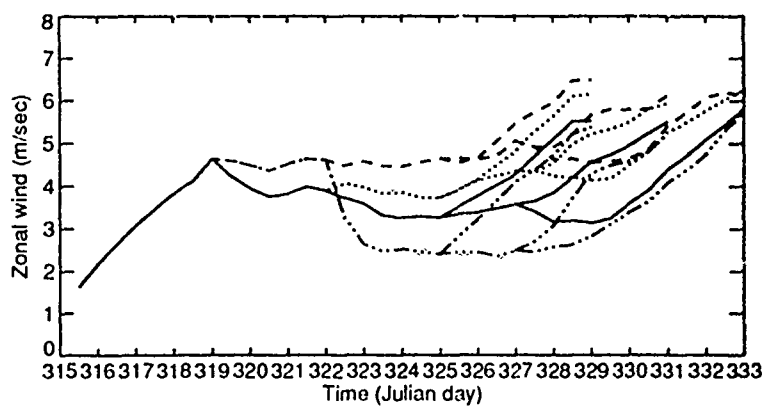
Forecast errors are also reduced. In the southern hemisphere extratropics the accuracy of the day 3 forecast has been improved relative to CONTROL by an equivalent increase in forecast range of 36 hours. Globally, an increase in forecast accuracy relative to CONTROL of 12 hours is seen, however northern hemisphere forecasts are only minimally affected.

Comparing analysis errors for the LIDAR and WINDSAT experiments we see that depending on the region, WINDSAT errors are either smaller or larger than LIDAR. Since each OSSE was run with a different control experiment we can compare the improvement of each experiment *relative* to their respective control runs. This indicates that WINDSAT generally shows a larger relative improvement over STATSAT than does LIDAR vs. CONTROL. For example, the southern hemisphere results show a reduction from approximately 45 m to 12-15 m with WINDSAT, compared with the 45 m to 25 m reduction noted above. In the northern hemisphere the WINDSAT improvement over STATSAT is about 15 m compared to only 5 m in LIDAR. We would expect a larger impact with WINDSAT data since the instrument was assumed to return more complete measurements throughout the clear troposphere. In addition, the CONTROL analysis is generally improved relative to STATSAT, so there is less room for improvement due to the additional lidar wind data.

6.2.2 850 hPa Zonal Wind rms Error

Figure 18 contains the analysis error of the 850 hPa u component wind as a function of time during the assimilation period. Globally the error is reduced from approximately $4\text{--}4.5\text{ ms}^{-1}$ to $3\text{--}3.5\text{ ms}^{-1}$ rms. In terms of region, the northern hemisphere shows only very small improvement over CONTROL, less than $.5\text{ ms}^{-1}$ to $-.3\text{ ms}^{-1}$ rms. In the tropics the reduction in error is also small but increases through the assimilation period so that by days 6 and 7 (julian days 328 and 329), the rms error goes from about 4 ms^{-1} to 3.5 ms^{-1} . Apparently the tropical wind variance is so small that there is little room for improvement,

a.



b.

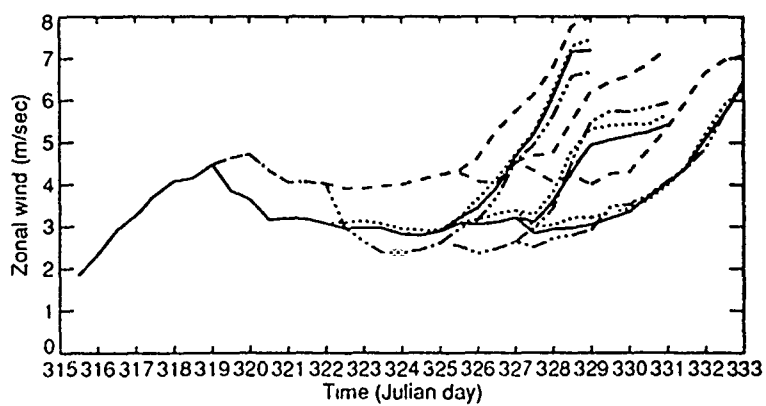
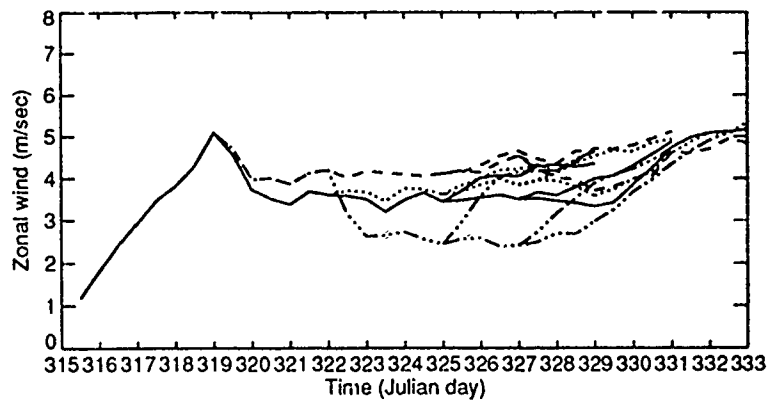


Figure 18. 850 hPa u component wind analysis and forecast errors averaged horizontally. (a) Global, (b) Northern hemisphere, (c) Tropics, (d) Southern hemisphere. Shown are CONTROL (dot), LIDAR (solid), STATSAT (dash), and WINIDSAT (dash-dot-dot-dot). (Continued . . .)

c.



d.

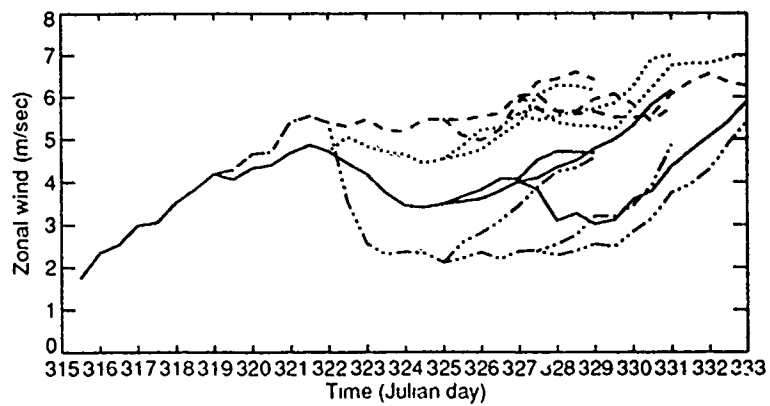


Figure 18. 850 hPa u component wind analysis and forecast errors averaged horizontally. (a) Global, (b) Northern hemisphere, (c) Tropics, (d) Southern hemisphere. Shown are CONTROL (dot), LIDAR (solid), STATSAT (dash), and WINDSAT (dash-dot-dot-dot).

even with relatively high quality wind data. In the southern hemisphere we again find the lidar data impact to be much greater. In CONTROL rms errors are 4.5 and 5.5 ms^{-1} at the start and end of the assimilation period, respectively. But in LIDAR these are reduced to approximately 3.5 and 3 ms^{-1} , respectively. Forecast accuracy is also seen to improve, particularly in the southern hemisphere; increases in predictability are as large as 48 h.

Compared to WINDSAT, improvements are more modest, generally no greater than one half the magnitude of the improvements seen in WINDSAT vs. STAT-SAT. Again, the comparison is somewhat ambiguous since (1) the CDW data were modified to induce horizontal correlations, and (2) the OI had been significantly altered.

6.2.3 200 hPa Zonal Wind rms Error

Errors for the 200 hPa u component wind are in figure 19. Impacts here generally resemble those at 850 hPa. That is, almost no impact in the northern hemisphere, small impact in the tropics ($< .5$ m/s improvement), and larger impact in the southern hemisphere. Here the error is reduced from about 6 m/s rms to approximately 4-5 m/s. Increases in predictability with the DWL data are somewhat smaller than at 850 hPa with improvements in the range 12 to 24 h. Finally, the LIDAR relative impacts are generally smaller than those for WINDSAT.

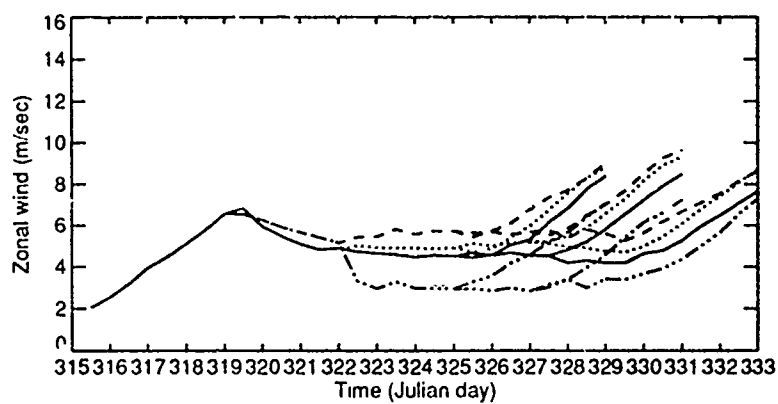
6.2.4 850 hPa Relative Humidity rms Error

Globally, improvement over CONTROL in the analysis error for relative humidity (figure 20) is small. Since both the northern hemisphere and tropics show essentially no impact most of this improvement is concentrated in the southern hemisphere. Here there is a positive impact which varies with time from less than 1 percent at the start of the assimilation period, to roughly 3 percent by day 7. Forecasts in the southern hemisphere are improved with predictability increases of 24 to 72 hours.

6.3 Analysis and Forecast Error as a Function of Pressure

Analysis errors were also averaged over latitude, longitude, and over the last 5 days of the assimilation period to obtain vertical profiles of error for the northern hemisphere, southern hemisphere, and tropical subregions. Plots for geopotential height, vector wind, relative humidity, and temperature are found in figures 21-24, respectively.

a.



b.

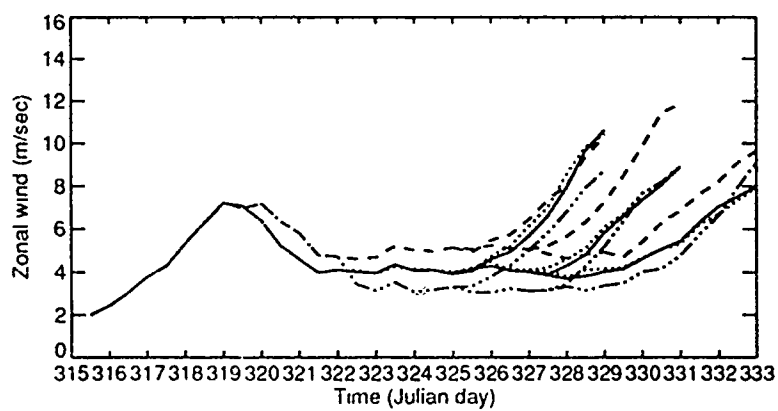
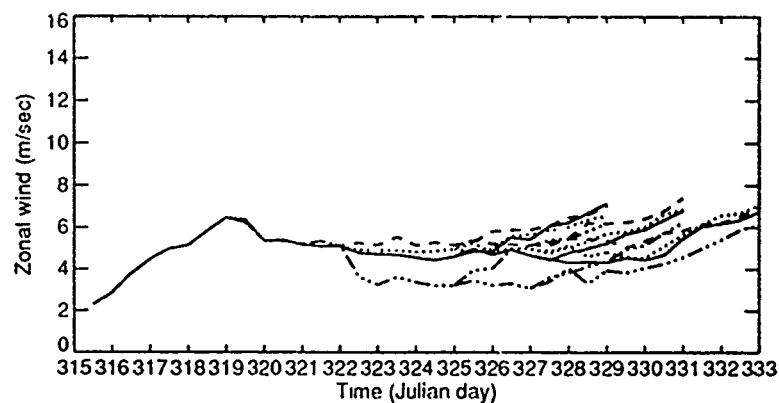


Figure 19. 200 hPa u component wind analysis and forecast errors averaged horizontally. (a) Global, (b) Northern hemisphere, (c) Tropics, (d) Southern hemisphere. Shown are CONTROL (dot), LIDAR (solid), STATSAT (dash), and WINDSAT (dash dot-dot dot). (Continued . . .)

c.



d.

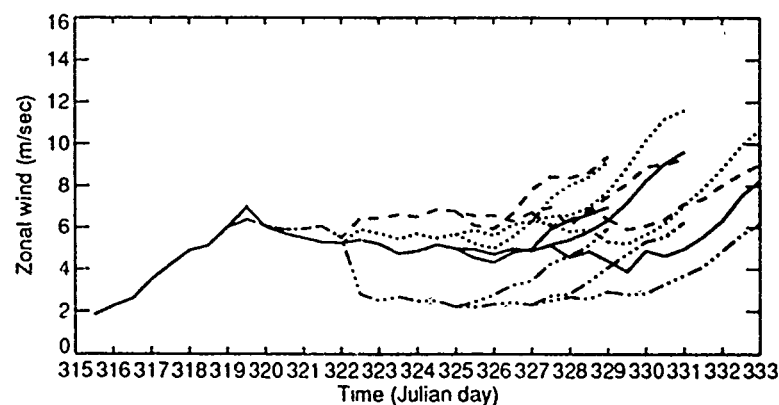


Figure 19. 200 hPa u component wind analysis and forecast errors averaged horizontally. (a) Global, (b) Northern hemisphere, (c) Tropics, (d) Southern hemisphere. Shown are CONTROL (dot), LIDAR (solid), STATSAT (dash), and WINDSAT (dash-dot-dot-dot).

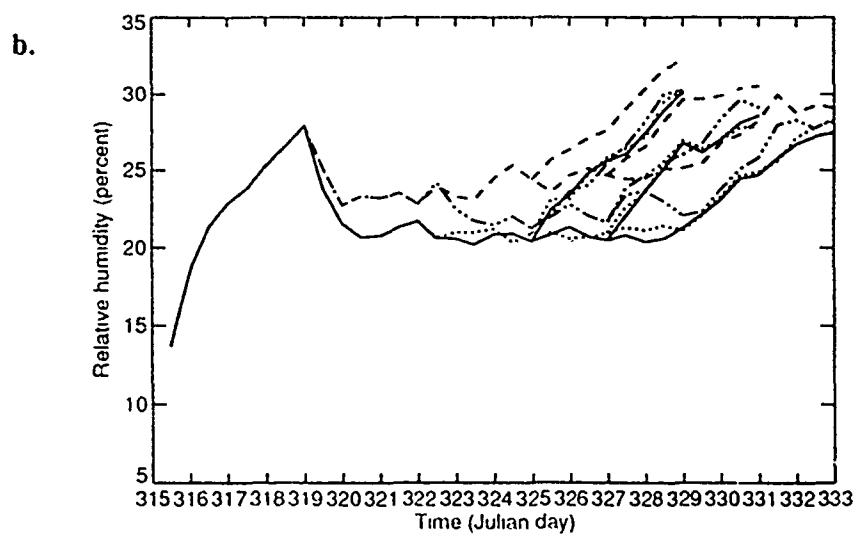
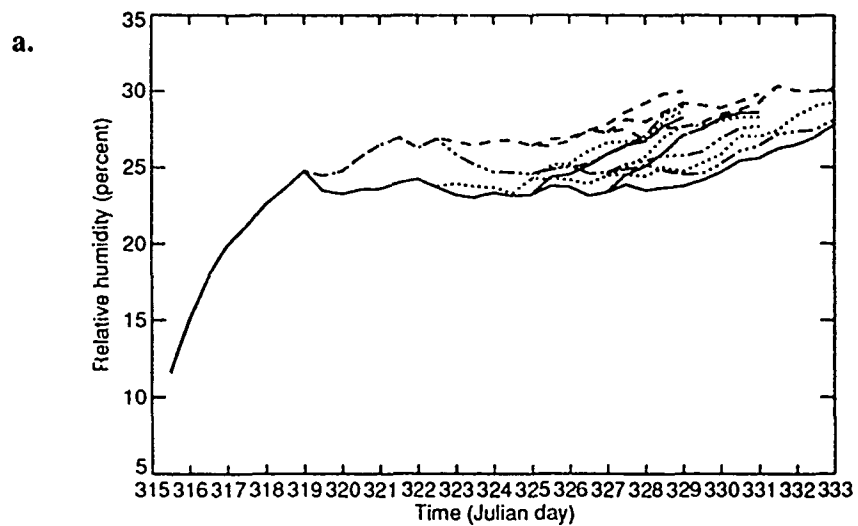


Figure 20. 850 hPa relative humidity analysis and forecast errors averaged horizontally. (a) Global, (b) Northern hemisphere, (c) Tropics, (d) Southern hemisphere. Shown are CONTROL (dot), LIDAR (solid), STATSAT (dash), and WINDSAT (dash-dot-dot dot). (Continued . . .)

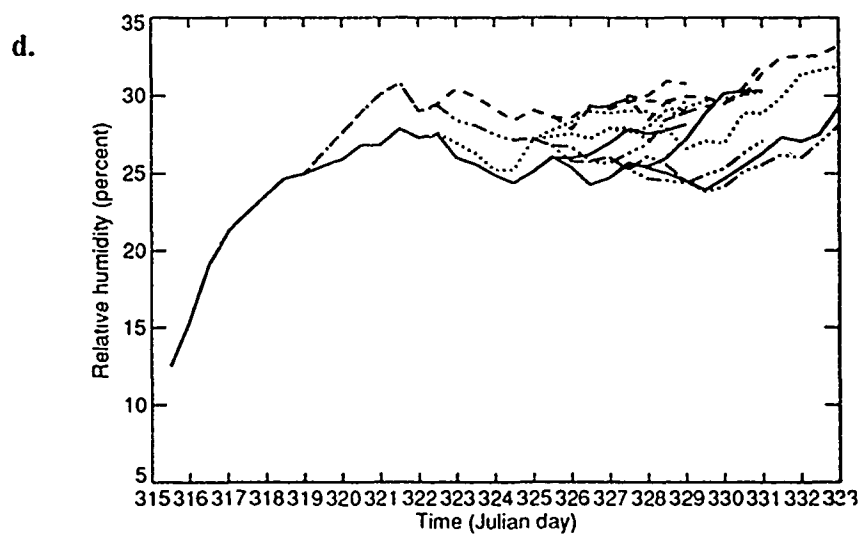
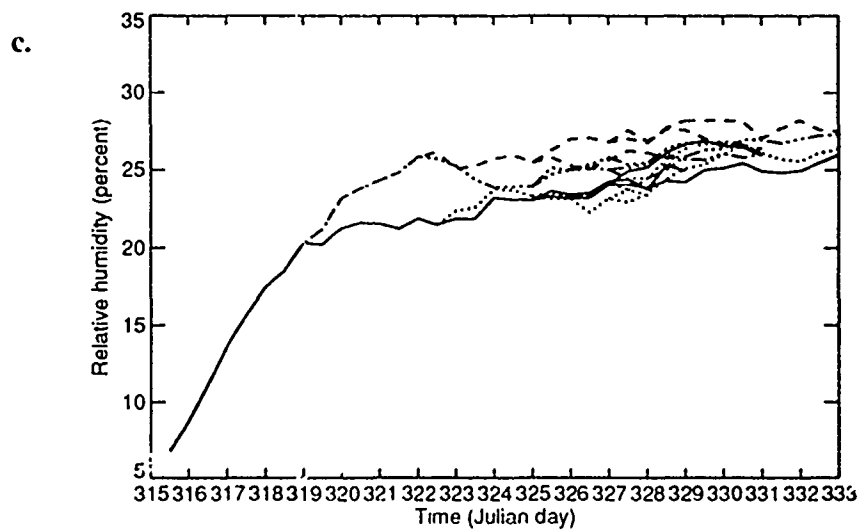


Figure 20. 850 hPa relative humidity analysis and forecast errors averaged horizontally. (a) Global, (b) Northern hemisphere, (c) Tropics, (d) Southern hemisphere. Shown are CONTROL (dot), LIIDAR (solid), STATSAT (dash), and WINDSAT (dash-dot-dot-dot).

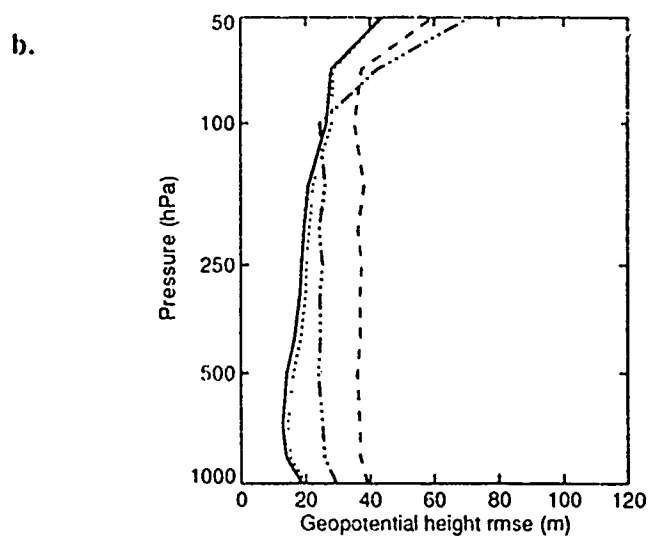
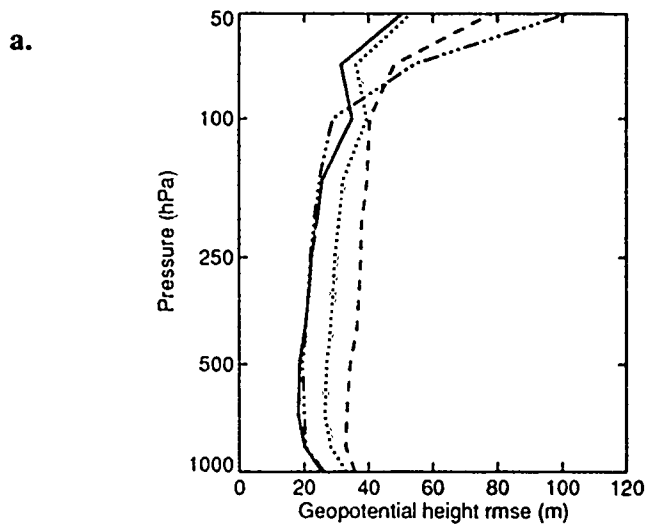
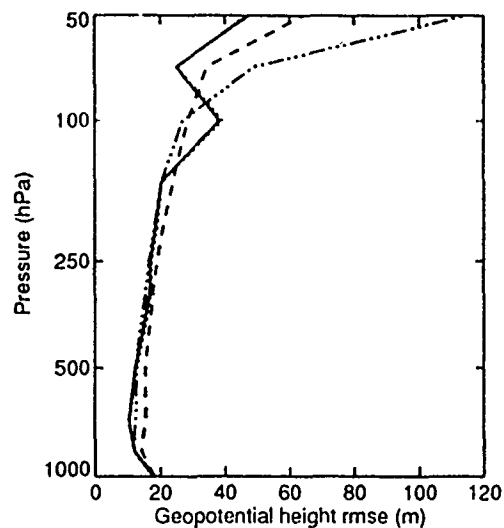


Figure 21. Geopotential height analysis error vs. pressure averaged horizontally and over the last 5 days of the assimilation period. (a) Global, (b) Northern hemisphere, (c) Tropics, (d) Southern hemisphere. Shown are CONTROL (dot), LIDAR (solid), STATSAT (dash), and WINDSAT (dash-dot-dot-dot). (Continued . . .)

c.



d.

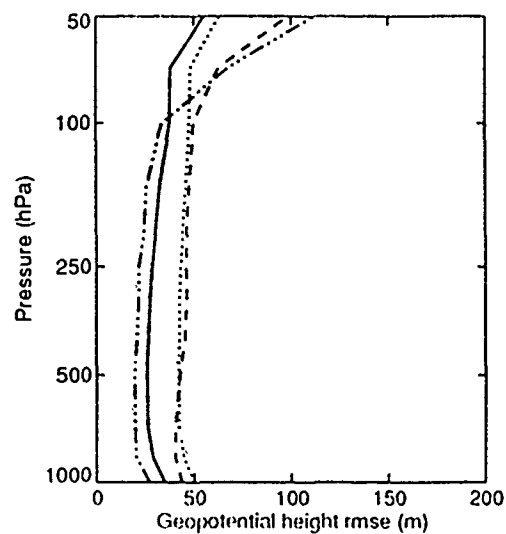


Figure 21. Geopotential height analysis error vs. pressure averaged horizontally and over the last 5 days of the assimilation period. (a) Global, (b) Northern hemisphere, (c) Tropics, (d) Southern hemisphere. Shown are CONTROL (dot), LIDAR (solid), STATSAT (dash), and WINDSAT (dash-dot-dot-dot).

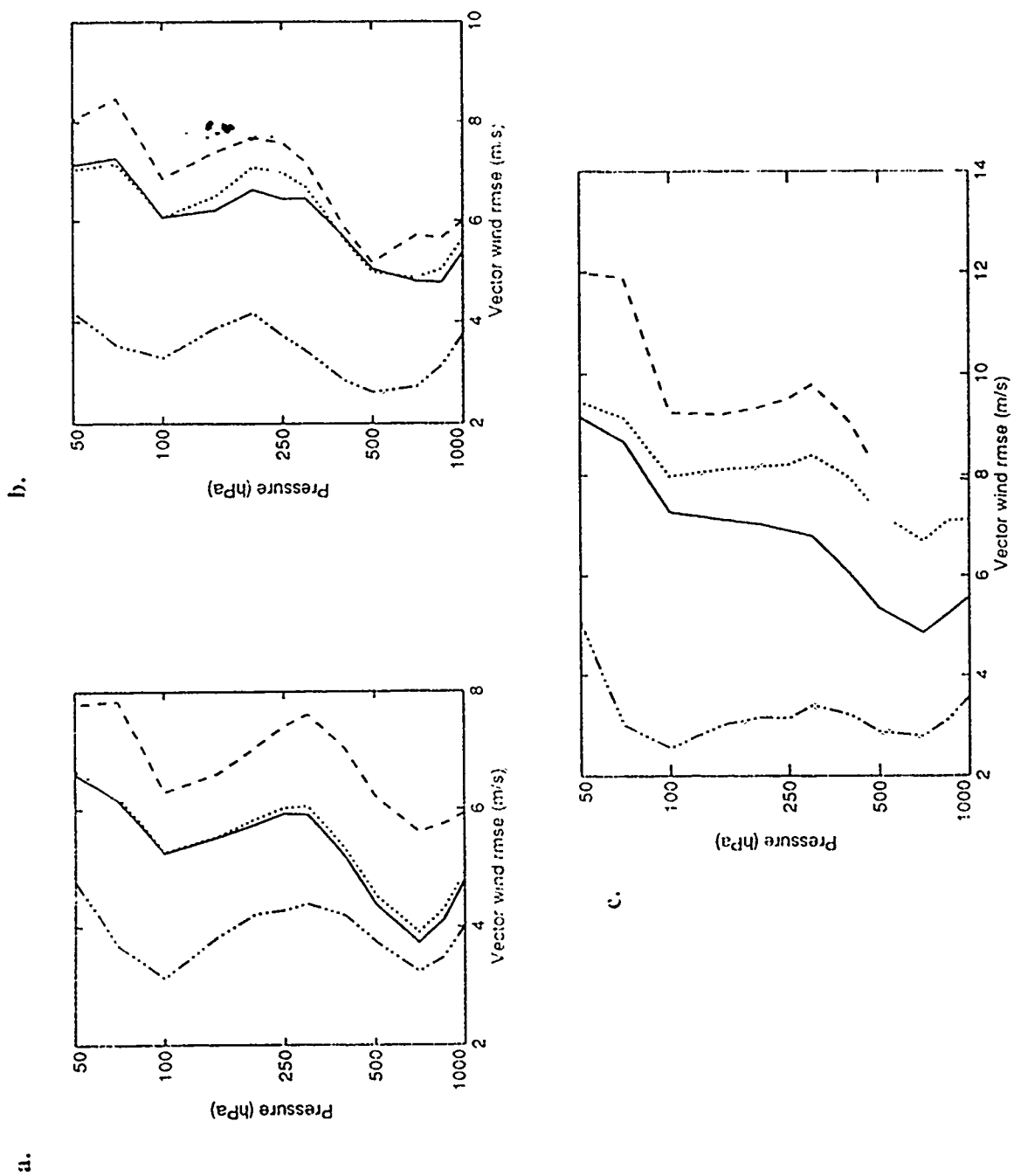
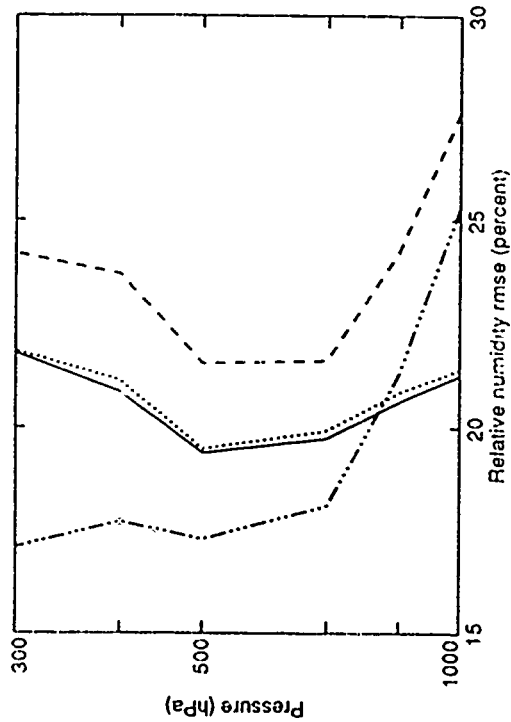
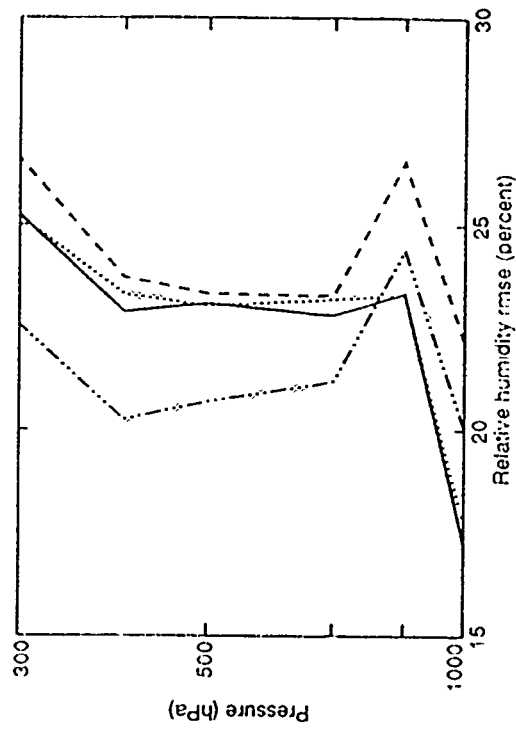


Figure 22. Vector wind analysis error vs. pressure averaged horizontally and over the last 5 days of the assimilation period. (a) Northern hemisphere, (b) Tropics, (c) Southern hemisphere. Shown are CONTROL (dot), Lf/AR (solid), STATSAT (dash), and WINDSAT (dash-dot-dot).

a.



b.



67

c.

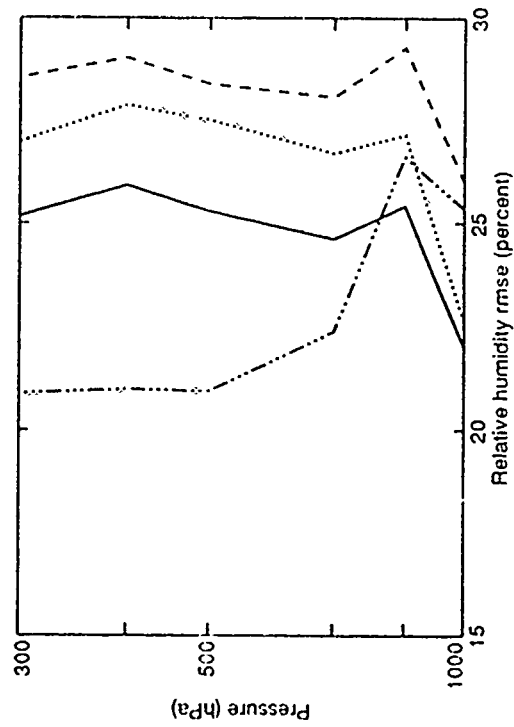


Figure 23. Relative humidity analysis error vs. pressure averaged horizontally and over the last 5 days of the assimilation period. (a) Northern hemisphere, (b) Tropics, (c) Southern hemisphere. Shown are CONTROL (solid), LIDAR (dotted), STATSAT (dashed), and WINDSAT (dash-dot-dot-dot).

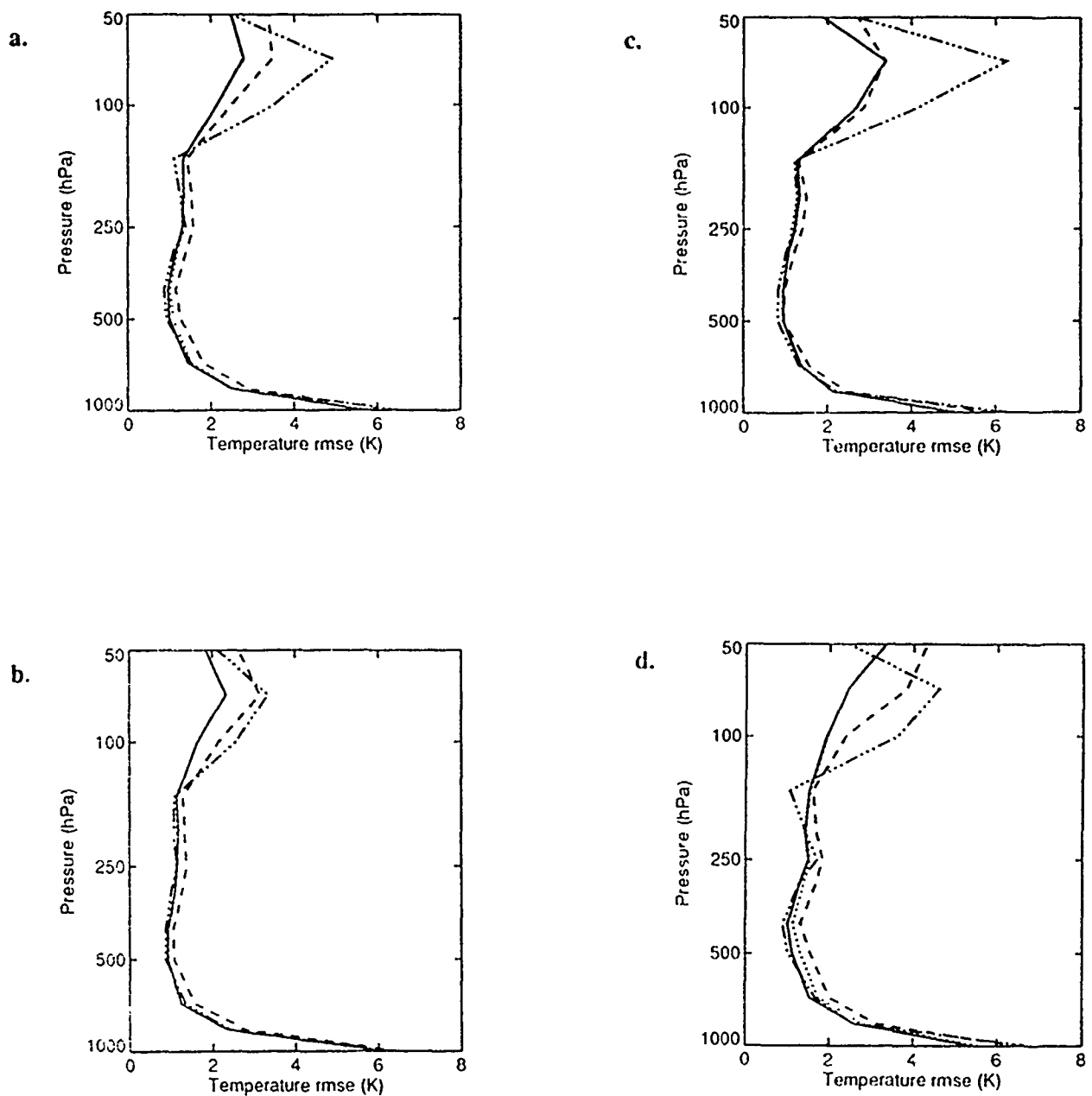


Figure 24. Temperature analysis error vs. pressure averaged horizontally and over the last 5 days of the assimilation period. (a) Global, (b) Northern hemisphere, (c) Tropics, (d) Southern hemisphere. Shown are CONTROL (dot), LIDAR (solid), STATSAT (dash), and WINDSAT (dash-dot-dot-dot).

6.3.1 Geopotential Height

As seen in the spatially averaged analysis errors of section 6.2 the largest impact is found in the southern hemisphere. Here errors are reduced from about 40-50 m in CONTROL to roughly 30 m between 1000 and 100 hPa. Compared to WINDSAT the impact in LIDAR is smaller, even accounting for the improved analysis system. The one exception to this is above 100 hPa where both CONTROL and LIDAR generally have smaller errors than either STATSAT or WINDSAT.

Vertical profiles of the height analysis errors show the improvement of LIDAR over CONTROL to be relatively constant with pressure. This indicates that most of the improvement to the height analyses is barotropic (i.e. layer thicknesses are not improved) and that most of the impact is a reflection of an improvement in the surface pressure analysis, which affects all levels equally.

6.3.2 Vector Wind

Similar to the earlier wind analysis results, the strongest effect of the DWL data is seen in the southern hemisphere where the rms vector wind error is reduced from 6.5-9.5 ms^{-1} to about 5-9 ms^{-1} , depending on level. In other regions the impact is no greater than roughly 1 ms^{-1} . Again it appears that WINDSAT impacts are larger with rms errors falling to 3-4.5 ms^{-1} .

6.3.3 Relative Humidity

These plots indicate that in all regions of the globe which were examined, specification of the relative humidity field is improved relative to CONTROL. The smallest positive impact is seen in the northern hemisphere and tropics where the LIDAR analysis error is generally smaller than CONTROL by less than 1 percent. In the southern hemisphere the observed impact is much larger. At and above 850 hPa the rms analysis error is reduced 2.5 to 3 percent, while at 1000 hPa the reduction falls to .5 percent. Between 700 and 300 hPa WINDSAT still appears to have a much larger impact in all regions reducing the rms error to about 17 percent in the northern hemisphere and 20-22 percent in the southern hemisphere. These results are consistent with those seen in the horizontally averaged statistics and in the synoptic plots above.

6.3.4 Temperature

Impacts upon the tropospheric temperature analyses are small for all experiments. Below 150 hPa most differences are less than .5 K. with the largest impacts seen in the southern hemisphere. However as seen in the height analysis errors, both CONTROL and LIDAR are superior to STATSAT and WINDSAT above 150 hPa, with typical reductions of error on the order of 1 to 4 K. This might be a reflection of improvements made in the handling of raob height data in the OI, which tend to affect both the height analyses and the temperature analyses.

6.4 Averaged Forecast Errors

Errors associated with the day 3, 5, and 7 forecasts were combined to produce a single averaged rms forecast error curve for each experiment and forecast variable. Results for 500 hPa, 200 hPa zonal wind, 850 hPa zonal wind, and 850 hPa relative humidity are found in figures 26 to 29, respectively.

In general, the averaged errors corroborate the features of individual forecast errors discussed in the earlier section: forecast impacts are largest in the southern hemisphere and negligible in the northern hemisphere. In the case of the 500 hPa height forecast errors the averaged improvement of LIDAR vs. CONTROL is of the order 2-2.5 days in the southern hemisphere and about 1 day globally. WINDSAT errors are better still by 1 day in the southern hemisphere and about 12 h globally. Zonal wind forecast errors also show the greatest impact of the DWL data to be in the south. Here the averaged improvement in forecast accuracy is 1-1.5 days at 200 hPa and roughly 2 days at 850 hPa. Globally the corresponding improvements are .5 and 1 day, respectively. WINDSAT still yields superior forecasts, improving over LIDAR in the southern hemisphere by about 1.5 days. Finally, relative humidity forecasts in LIDAR are better than CONTROL by 1-1.5 days in the southern hemisphere, and WINDSAT errors, which are initially larger than LIDAR in the south eventually become smaller than LIDAR by approximately 12 h. In the tropics and northern hemisphere LIDAR does not improve forecast errors relative to CONTROL and WINDSAT errors in this region are actually larger than either CONTROL or LIDAR.

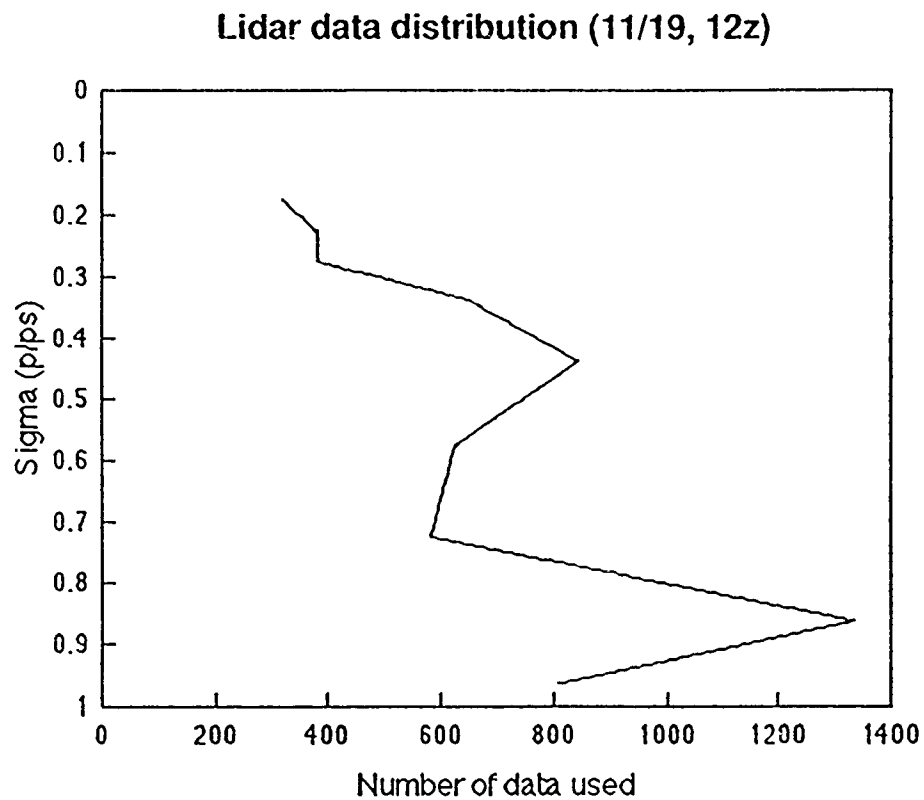


Figure 25. Number of lidar returns as a function of model sigma level for 12 UTC 19 November 1979. A sigma value of 1 corresponds to the surface level.

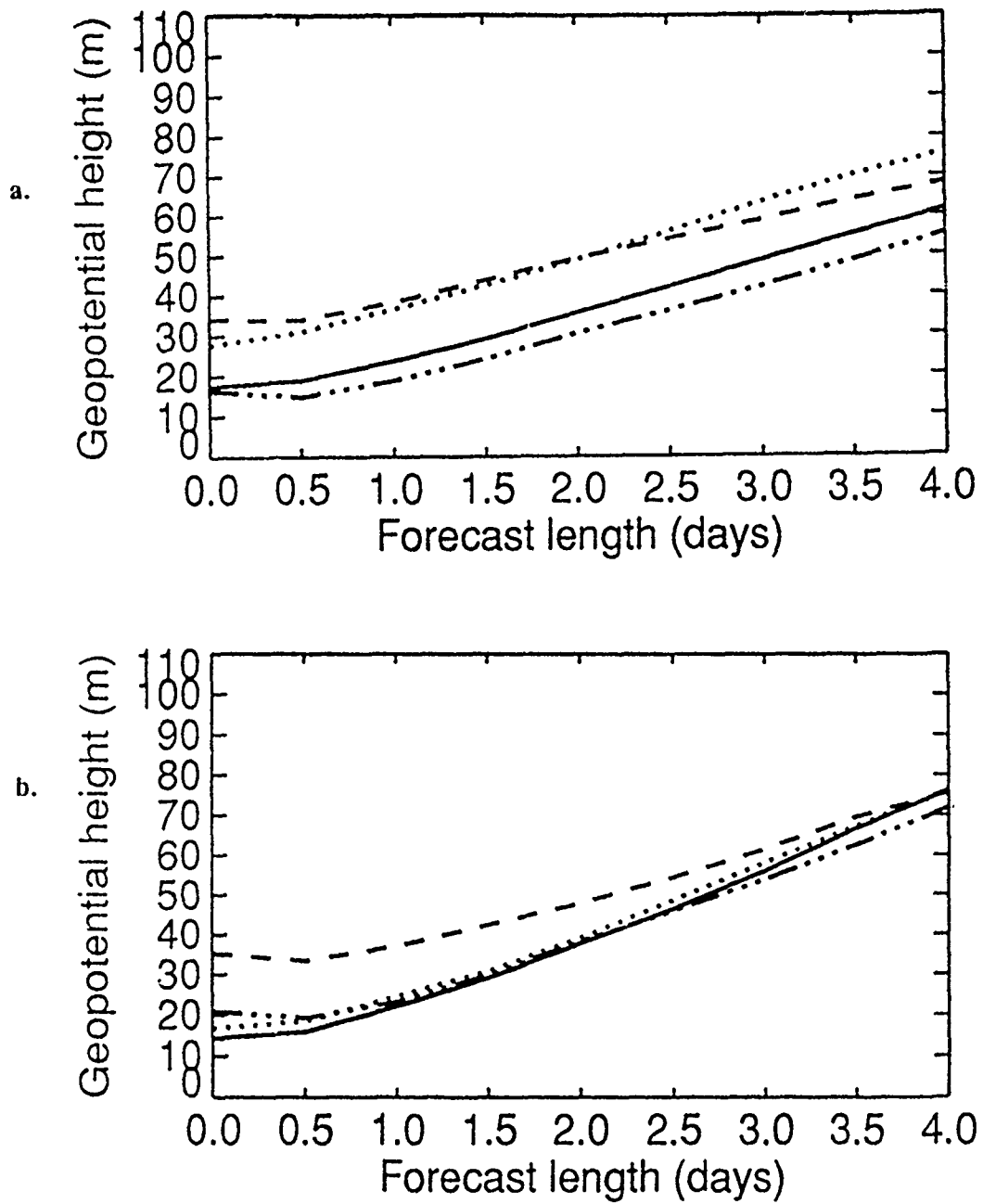


Figure 26. 500 hPa height forecast errors as a function of time averaged over the day
 3, 5, and 7 forecasts (a) Global, (b) Northern Hemisphere, (c) Tropics, (d) Southern
 Hemisphere. Experiments shown are LIDAR (solid), CONTROL (dot), STATSAT (dash), and
 WINDSAT (dash-dot-dot-dot). Figs. 27 through 29 have the same format. (Continued ...)

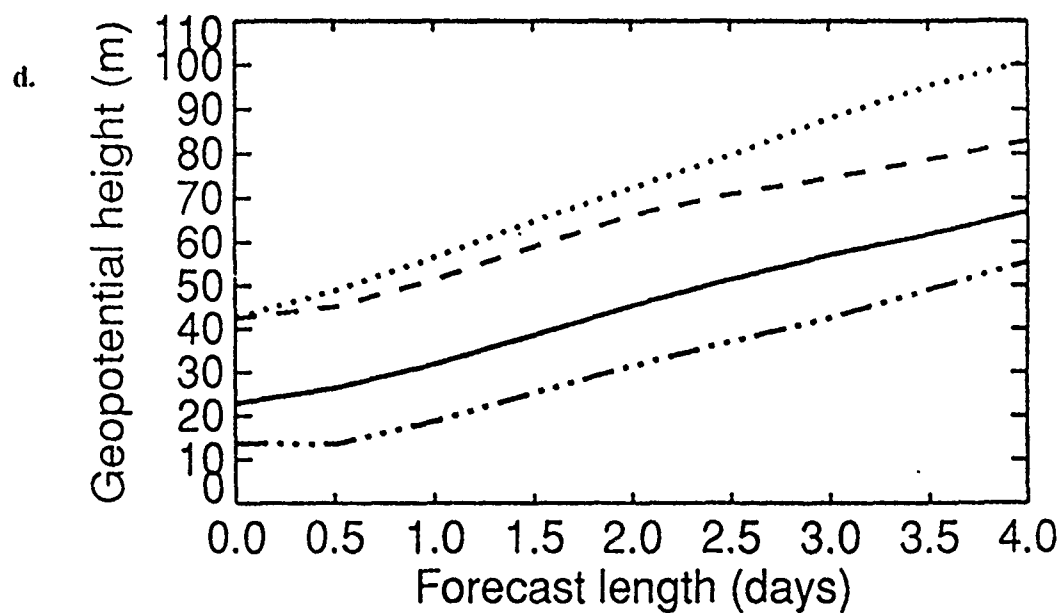
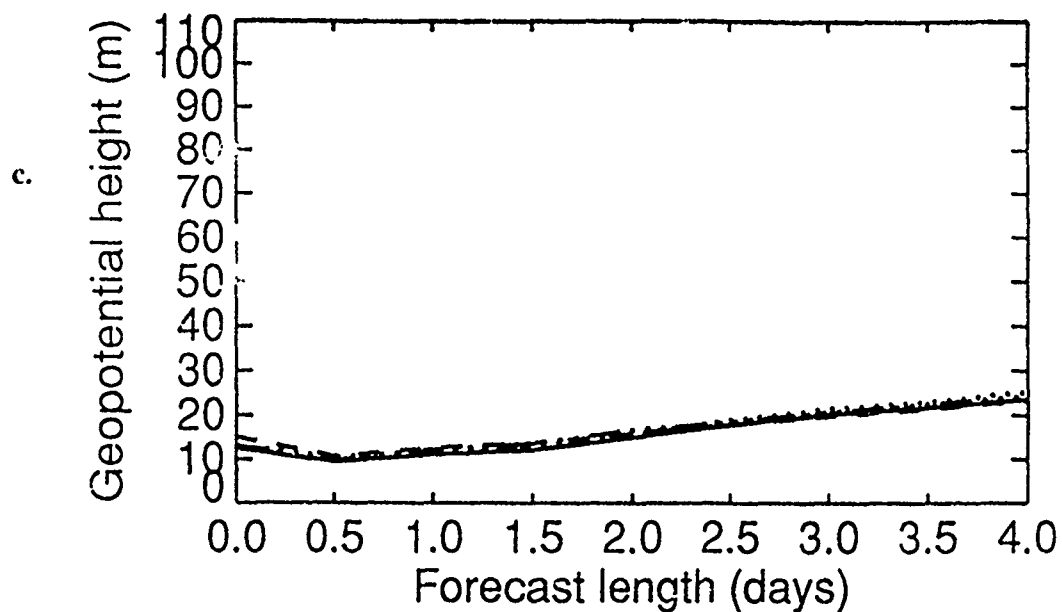


Figure 26. 500 hPa height forecast errors as a function of time averaged over the day 3, 5, and 7 forecasts. (a) Global, (b) Northern Hemisphere, (c) Tropics, (d) Southern Hemisphere. Experiments shown are LIDAR (solid), CONTROL (dot), STATSAT (dash), and WINDSAT (dash-dot-dot-dot). Figs. 27 through 29 have the same format.

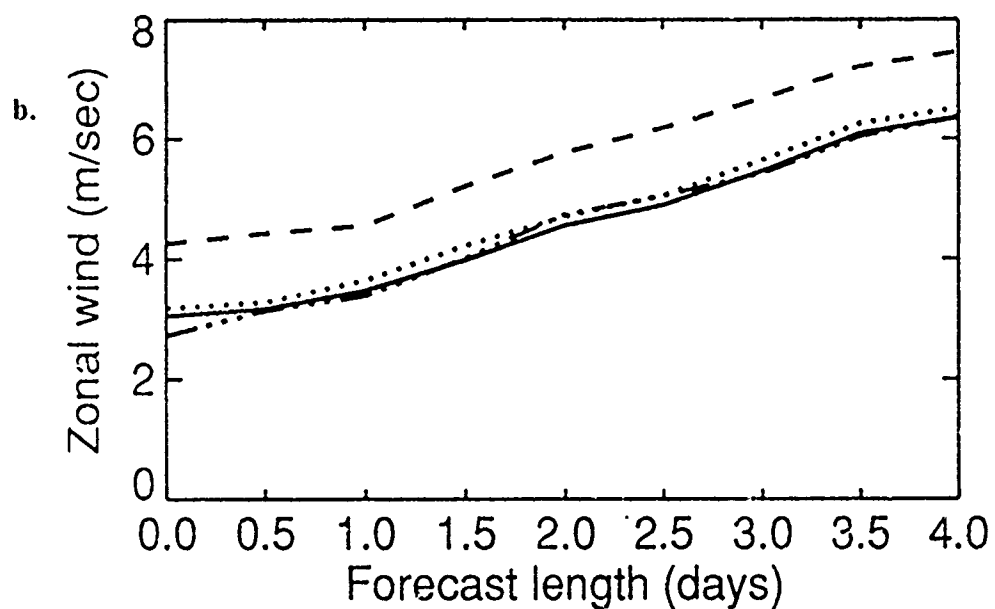
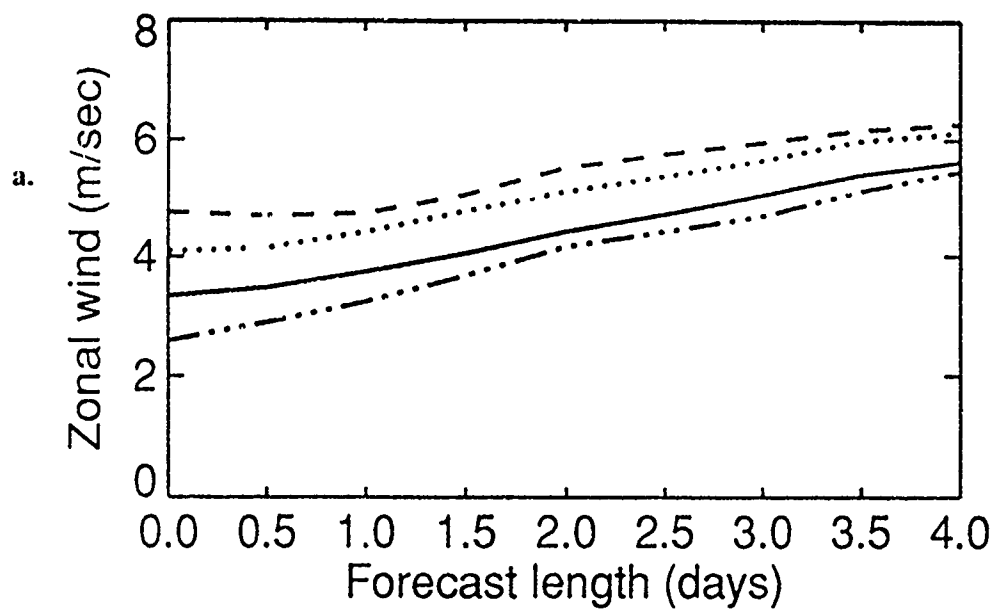


Figure 27. 850 hPa zonal wind forecast errors as a function of time averaged over the day 3, 5, and 7 forecasts. See fig. 26 for format and labelling. (Continued ...)

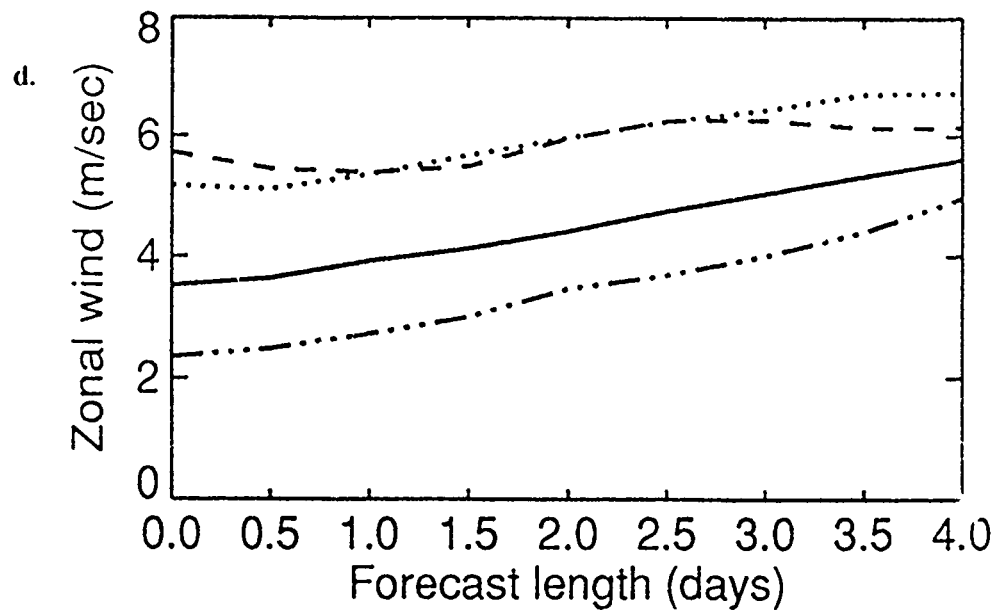
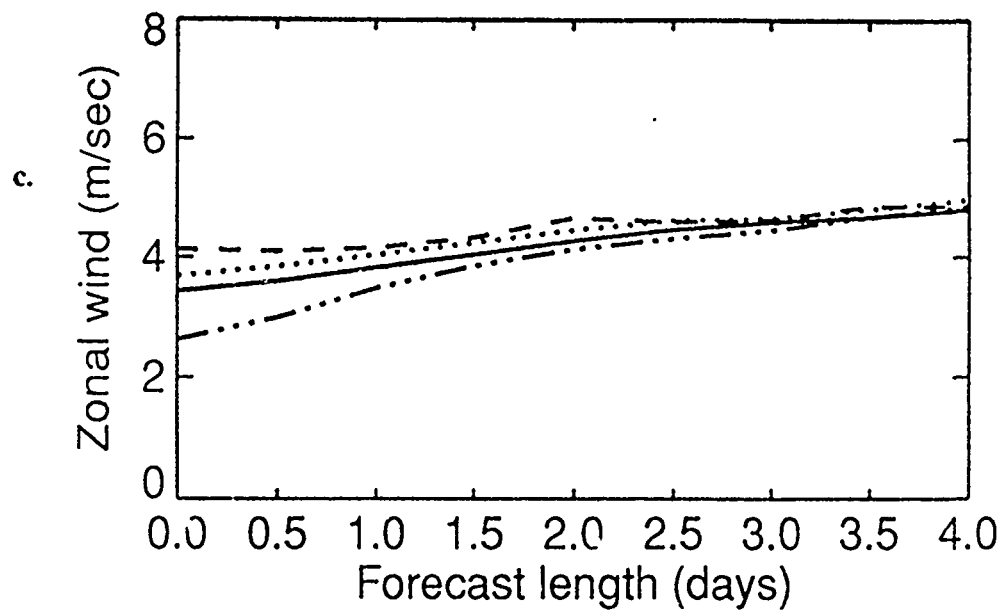


Figure 27. 850 hPa zonal wind forecast errors as a function of time averaged over the day 3, 5, and 7 forecasts. See fig. 26 for format and labelling.

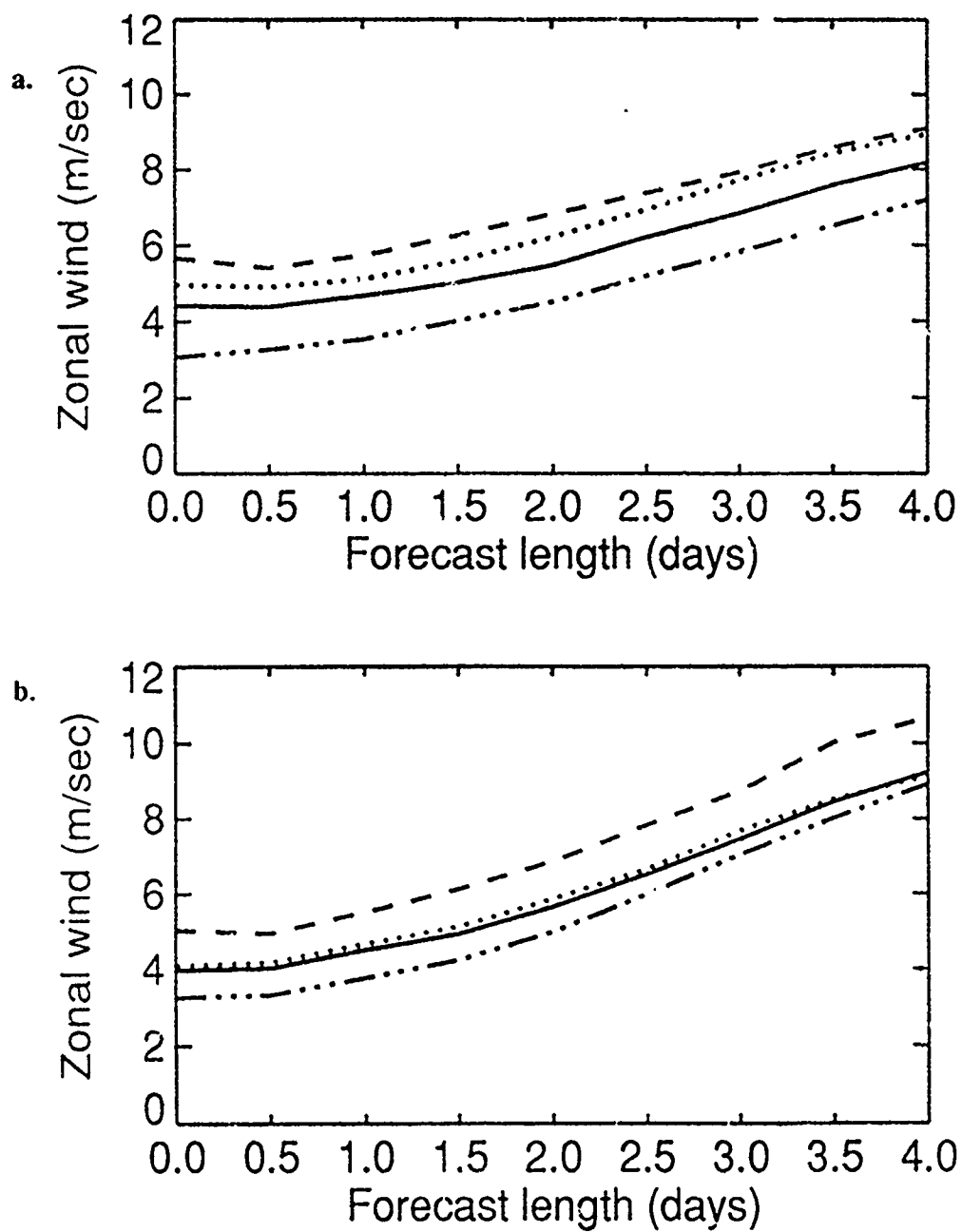


Figure 28. 200 hPa zonal wind forecast errors as a function of time averaged over the day 3, 5, and 7 forecasts. See fig. 26 for format and labelling. (Continued . . .)

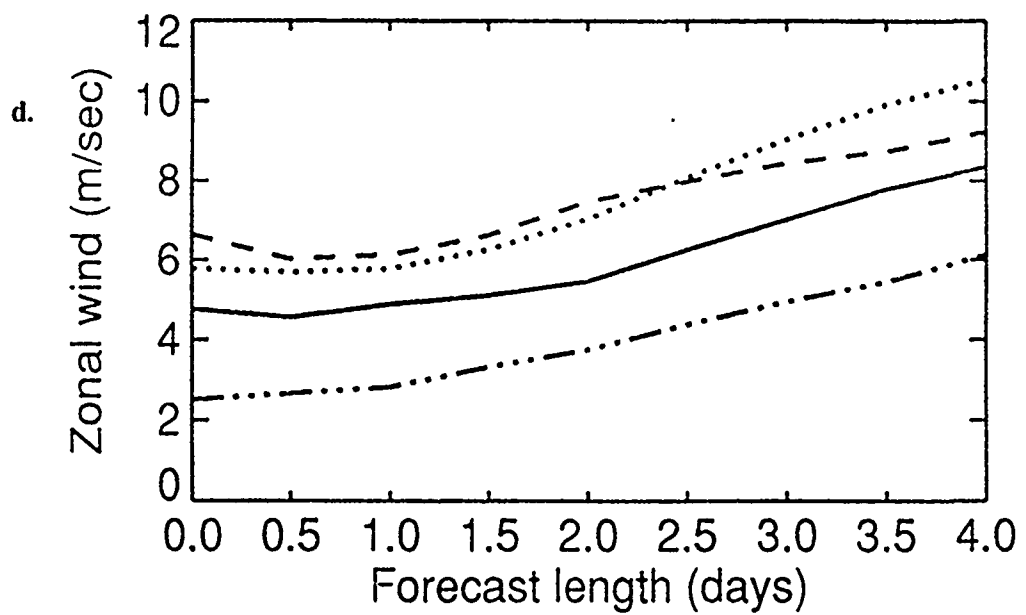
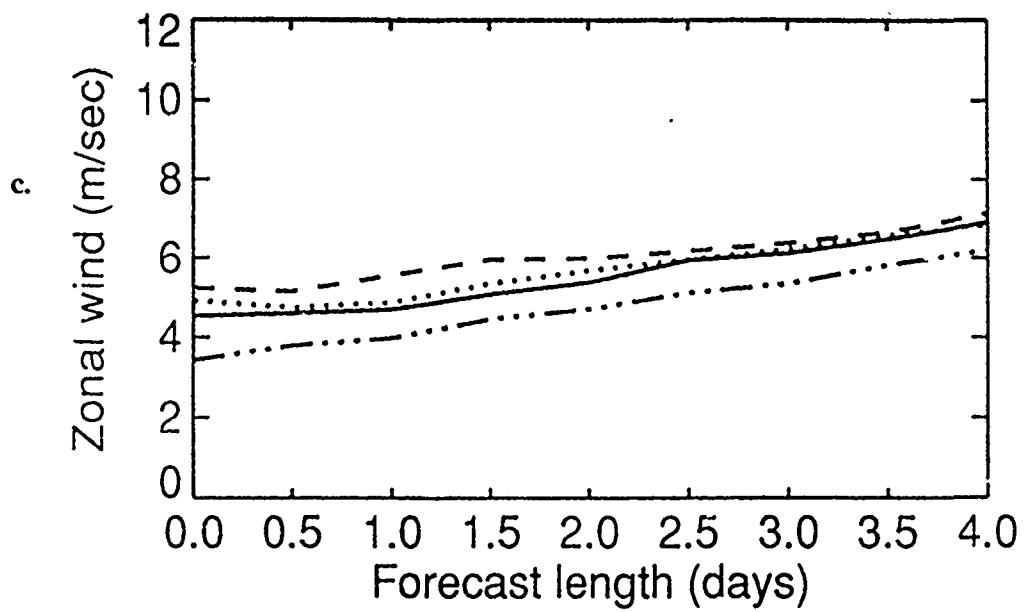


Figure 28. 200 hPa zonal wind forecast errors as a function of time averaged over the day 3, 5, and 7 forecasts. See fig. 26 for format and labelling.

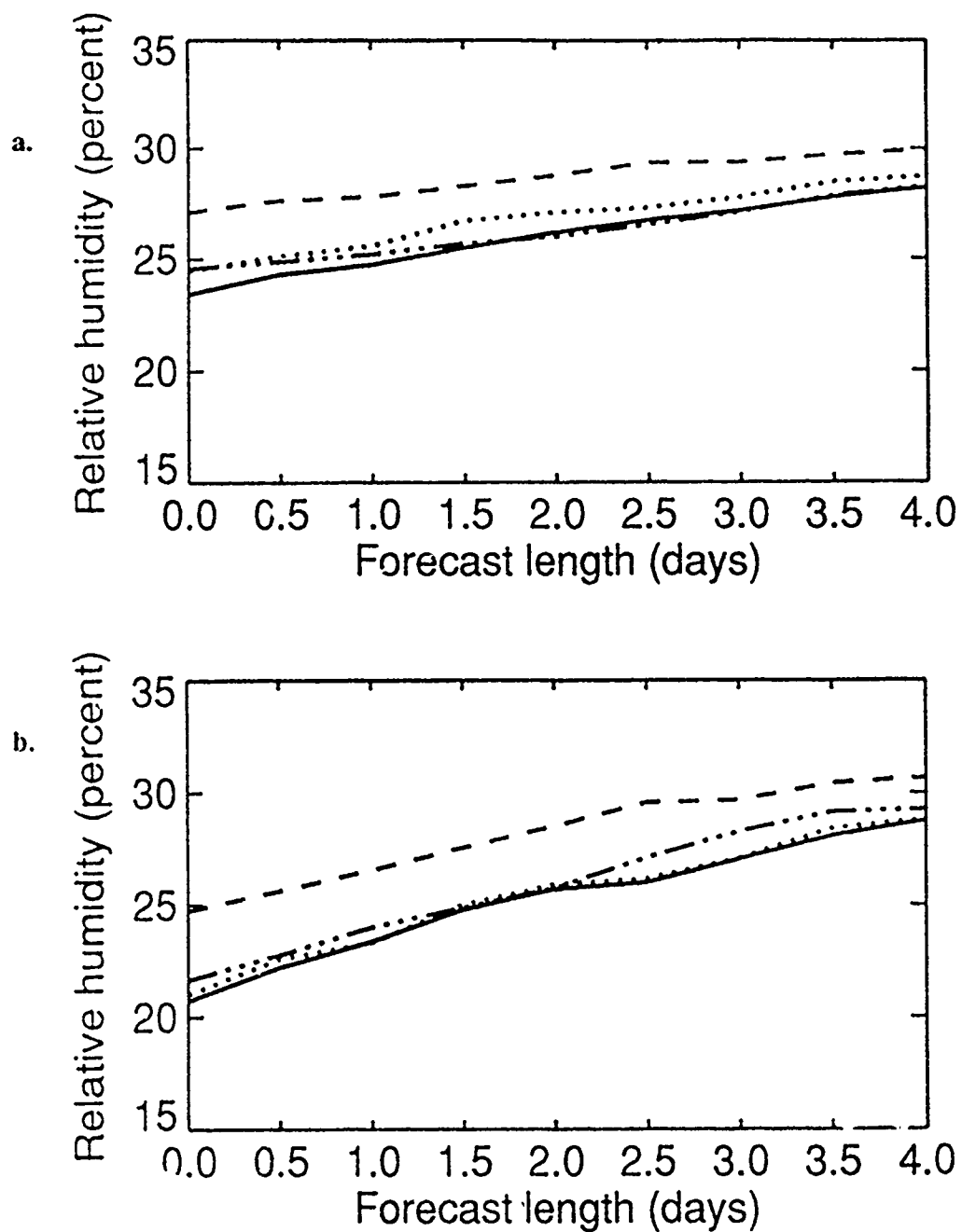


Figure 29. 850 hPa relative humidity forecast errors as a function of time averaged over the day 3, 5, and 7 forecasts. See fig. 26 for format and labelling. (Continued . . .)

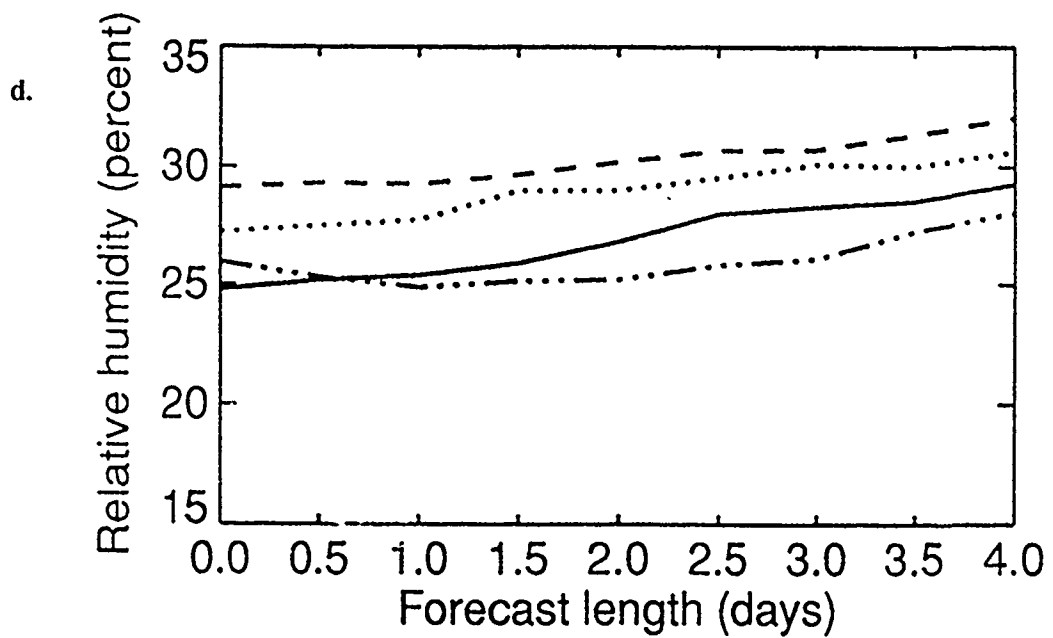
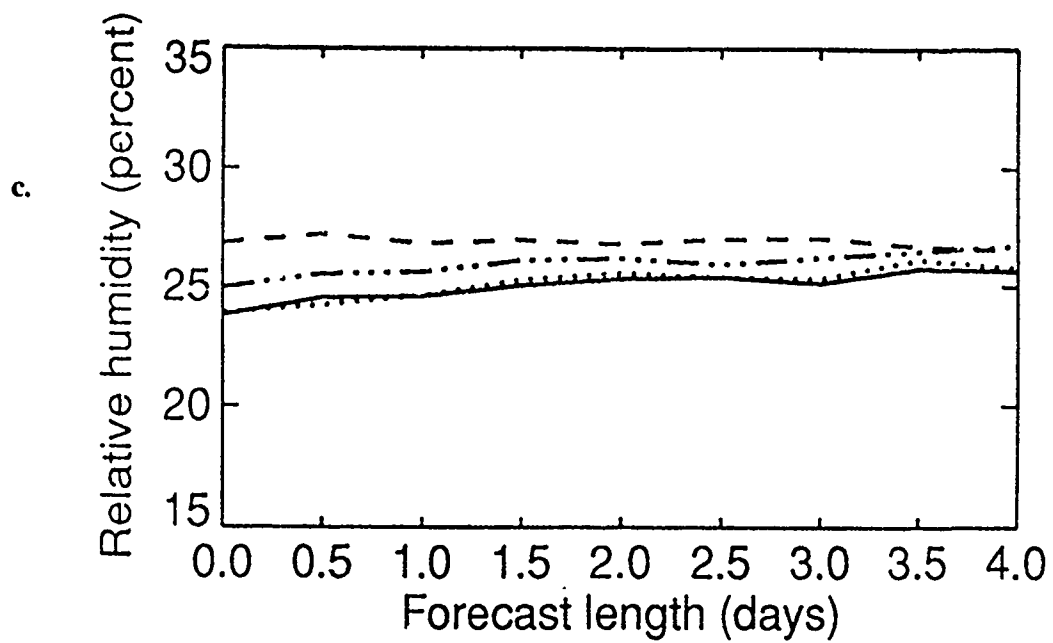


Figure 29. 850 hPa relative humidity forecast errors as a function of time averaged over the day 3, 5, and 7 forecasts. See fig. 26 for format and labelling.

6.5 Comparison with WINDSAT

Because WINDSAT and LIDAR were run using different analysis systems, gauging relative data impact is rather difficult. The control experiment corresponding to WINDSAT (i.e. STATSAT) had substantially larger errors in the northern hemisphere than the control experiment using the new analysis system (CONTROL) - the difference in northern hemisphere 500 hPa height errors between CONTROL and STATSAT were larger than the WINDSAT impact using the old OI. Thus, although the northern hemisphere LIDAR impact was negligible and the WINDSAT impact was large and positive, no definitive conclusions can be drawn about the relative impact of the two lidar sounders in the northern hemisphere, since the WINDSAT impact is certain to be much reduced for the new analysis system. The overestimate of the WINDSAT impact in the northern hemisphere is due to the fact that in the old analysis system the WINDSAT data provided the only information about the surface pressure gradient.

In the tropics and southern hemisphere the differences between CONTROL and STATSAT are smaller, allowing a more meaningful comparison between the two impact experiments. The zonal wind impact in the tropics was essentially zero for LIDAR, but it was large and positive in WINDSAT. The new analysis system also reduced errors compared to STATSAT, but by much less than WINDSAT, so that the WINDSAT impact can reasonably be expected to remain positive even for the improved analysis. In the southern hemisphere, both the height and zonal wind errors were little affected by the new analysis system, so that WINDSAT and LIDAR impacts can be directly compared. In terms of 500 hPa heights, the reduction in analysis error in LIDAR is between 1/2 and 3/4 that of WINDSAT, and the LIDAR increase in predictability of 1.5 to 2 days is about 1 day less than that of WINDSAT. The zonal wind rmse at 850 hPa show a LIDAR impact that is half the magnitude as that seen in WINDSAT, whereas it is slightly smaller, both in absolute and relative terms, at 200 mb. This may be a direct reflection of the data distribution in the two systems: the LIDAR sounder only has data at 200 hPa if there is cirrus present at that level, whereas marine boundary layer winds were assumed available everywhere where the return signal was not blocked by intervening cloud layers. For example, figure 25 shows the vertical distribution of lidar data for 1200 UTC on 19 November indicating a sharp peak near $\sigma=0.9$, and much fewer observations at $\sigma=0.2-0.3$. Since this pattern suggests that, to some extent, differences in impact between LIDAR and WINDSAT are a function of data availability or volume, it may be reasonable to consider the use of two simultaneous DWL-bearing satellites, each of which can fill in the gaps in horizontal coverage left by the other. Relative humidity

impacts were primarily limited to the southern hemisphere for LIDAR, unlike WINDSAT which also improved the specification in the northern hemisphere. But again, WINDSAT impacts may be overstated in the north because of the analysis system used. It is likely that, run with the updated OI, WINDSAT would yield impacts similar to LIDAR.

7. CONCLUSIONS

We have conducted an OSSE to determine the potential impact of a simple low energy DWL sensor on a global assimilation and forecast system. Measurements were simulated assuming that returns would mainly be available at or near cloud tops and in the marine boundary layer. This can be contrasted with measurements from LAWS which are expected to be more complete with measurements throughout the clear troposphere.

We have found that measurements from such a scaled down DWL have a positive impact on analyses and forecasts. Analyses errors for geopotential height are reduced in both northern and southern hemisphere extratropics, but especially in the south where conventional observations are few. Analyses of horizontal wind are improved in all regions, with the largest impact again seen in the southern hemisphere. Improvements in forecasts initialized with the new analyses are also found. In some cases rms forecast errors of height are improved an equivalent of 24-36 hours in forecast time relative to control cases.

The major results of the OSSE are summarized by these specific findings:

1. Synoptic maps:
 - Reduction in analysis and forecast errors of 500 hPa geopotential height in the southern hemisphere by factors of 2-3;
 - Most of the data impact on vector wind analyses and forecasts is in the southern hemisphere with wind vector errors of $20-30 \text{ m s}^{-1}$ reduced to 10 m s^{-1} ;
 - For relative humidity, most impact also in the southern extratropics with large areas of errors greater than 50% in the CONTROL experiment reduced in the LIDAR analysis. Similar results for humidity forecasts with improved specification of the horizontal motion field leading to a better moisture forecast.
2. Time evolution of forecast and analysis error:
 - Global reduction of the 500 hPa height analysis error by a factor of two (from 25 m to 12 m), most dramatic in the southern hemisphere. A global

increase in accuracy for a day 3 forecast by the equivalent of 12 h relative to CONTROL (36 h in the southern hemisphere extratropics);

- A thirty percent reduction in the error of the 850 hPa zonal wind component with a forecast predictability improvement in the southern hemisphere of up to 48 h;
- Consistent positive impact on the analysis of 850 hPa relative humidity in the southern hemisphere with forecast predictability increases of 24 to 72 h compared to CONTROL.

3. Averaged forecast error:

- Global improvement of the 500 hPa height forecast (compared to CONTROL) by 1 day (2–2.5 days in the southern hemisphere);
- Global zonal wind forecast error improvements of 0.5 and 1 day at 850 hPa and 200 hPa, respectively. (1–1.5 days and 2 days, respectively, in the southern hemisphere);
- Improvements in the 850 hPa humidity forecasts by 1–1.5 days.

We have also performed an OSSE to evaluate the impact of a WINDSAT type instrument (Hoffman *et al.*, 1990). In the examination of southern hemisphere results, a meaningful comparison of WINDSAT and LIDAR results can be made. The scaled down DWL system reduces 500 hPa geopotential analysis errors by 1/2 to 3/4 that of the WINDSAT system. Predictability increases for LIDAR are about one day less than WINDSAT. Zonal wind improvements are about 1/2 of WINDSAT. However, deficiencies in the analysis system used in WINDSAT tend to exaggerate the positive impact of a WINDSAT instrument relative to LIDAR (which was run with an enhanced analysis system) in the northern hemisphere, making intercomparison in this region more difficult.

To a large degree, results obtained here substantiate previous data impact studies which used simulated DWL data. What this study has attempted to do is show that a low energy DWL, which may be viewed as a lower cost alternative to proposed instruments such as LAWS, might also improve the global analysis and prediction of mass and motion fields. To the extent that the results we have shown are valid, such a scaled down DWL should receive serious consideration by the remote sensing and atmospheric sciences community in any discussion of future space-based observing systems.

These results represent a first attempt to assess the viability of a simple DWL concept for NWP. As such, we would suggest that follow up studies would help extend and validate the results shown here. For example, we might wish to determine impact sensitivity to various orbital inclinations. Results which show a

larger impact in the southern hemisphere would seem to argue for a more highly inclined orbit. Additionally, as with all OSSEs, the issue of simulated errors is critical. Our measurements assumed unbiased -1 m s^{-1} rms errors. Further off-line studies using radiative transfer calculations would help determine whether the level of accuracy might be more dependent upon cloud microphysical properties. Additional consideration is also needed of whether some cloud and aerosol regimes might lead to horizontally correlated errors.

REFERENCES

- C. P. Arnold, C. H. Dey, and W. J. Bostelman. Results of an observing system simulation experiment based on the proposed WINDSAT instrument. In W. E. Baker and R. J. Curran, editors, *Global Wind Measurements*, pages 81–88. A. Deepak Publishing, Hampton, VA, 1985.
- R. Atlas, E. Kalnay, W. E. Baker, J. Susskind, D. Reuter, and M. Halem. Observing systems simulation experiments at GSFC. In W. E. Baker and R. J. Curran, editors, *Global Wind Measurements*, pages 65–71. A. Deepak Publishing, Hampton, VA, 1985.
- W. E. Baker and R. J. Curran, editors. *Report of the NASA Workshop on Global Wind Measurements*. A. Deepak Publishing, Hampton, VA, 1985.
- B. Ballish. *Initialization, theory and application to the NMC spectral model*. PhD thesis, Department of Meteorology, University of Maryland, College Park, MD, 1980.
- L. Bengtsson, M. Kanamitsu, P. Källberg, and S. Uppala. FGGE 4-dimensional data assimilation at ECMWF. *Bulletin of the American Meteorological Society*, 63:29–43, 1982.
- K. H. Bergman. Multivariate analysis of temperature and winds using optimum interpolation. *Monthly Weather Review*, 107:1423–1444, 1979.
- S. Brenner, C.-H. Yang, and S. Y. K. Yee. The AFGL spectral model of the moist global atmosphere: Documentation of the baseline version. Technical Report 82-0393, Air Force Geophysics Laboratory, Hanscom AFB, MA, 1982. [NTIS ADA129283].
- S. Brenner, C.-H. Yang, and K. Mitchell. The AFGL global spectral model: Expanded resolution baseline version. Technical Report 84-0308, Air Force Geophysics Laboratory, Hanscom AFB, MA, 1984. [NTIS ADA160370].
- R. J. Curran et al. LAWS instrument panel report. Technical report, NASA, Washington, DC, 1988.
- R. J. Curran. NASA's plans to observe the Earth's atmosphere with lidar. *IEEE Transactions on Geoscience and Remote Sensing*, 27:154–163, 1989.

- C. H. Dey and L. L. Morone. Evolution of the National Meteorological Center Global Data Assimilation System: January 1982-December 1983. *Monthly Weather Review*, 113:304-318, 1985.
- C. Dey, C. P. Arnold, and W. Bostelman. Design of a WINDSAT observing system simulation experiment. In W. E. Baker and R. J. Curran, editors, *Global Wind Measurements*, pages 73-79. A. Deepak Publishing, Hampton, VA, 1985.
- A. J. Heymsfield and C. M. R. Platt. A preliminary parameterization of the particle size spectrum of cirrus clouds in terms of the cloud temperature and liquid water content. *Journal of the Atmospheric Sciences*, 41:846-855, 1984.
- R. N. Hoffman, C. Grassotti, R. G. Isaacs, J.-F. Louis, T. Nehr Korn, and D. C. Norquist. Assessment of the impact of simulated satellite lidar wind and retrieved 183 GHz water vapor observations on a global data assimilation system. *Monthly Weather Review*, 118:2513-2542, 1990.
- A. Hollingsworth, K. Arpe, M. Tiedtke, M. Capaldo, and H. Savijärvi. The performance of a medium range forecast model in winter - impact of physical parameterization. *Monthly Weather Review*, 108:1736-1773, 1980.
- R. G. Isaacs, G. Deblonde, R. D. Worsham, and M. Livshits. Millimeterwave moisture sounder feasibility study: The effect of cloud and precipitation on moisture retrievals. Technical Report 85-0040, Air Force Geophysics Laboratory, Hanscom AFB, MA, 1985. ADA162231
- Steven E. Koch, Mary DesJardins, and Paul J. Kocin. An interactive Barnes objective map analysis scheme for use with satellite and conventional data. *Journal of Climate and Applied Meteorology*, 22:1487-1503, 1983.
- J.-F. Louis, R. N. Hoffman, T. Nehr Korn, and D. Norquist. Observing systems experiments using the AFGL four-dimensional data assimilation system. *Monthly Weather Review*, 117:2186-2203, 1989.
- R. D. McPherson, K. H. Bergman, R. E. Kistler, G. E. Rasch, and D. S. Gordon. The NMC operational global data assimilation system. *Monthly Weather Review*, 107:1445-1461, 1979.
- R. D. McPherson. Cloud drift wind estimates during FGGE. Office Note 288, NMC, Washington, DC, 1984.
- D. C. Norquist. Alternative forms of moisture information in 4-D data assimilation. Technical Report 86-0194, Air Force Geophysics Laboratory, Hanscom AFB, MA, 1986. [NTIS ADA179792].
- D. C. Norquist. Alternate forms of humidity information in global data assimilation. *Monthly Weather Review*, 116:452-471, 1988.

- C. M. R. Platt and A. C. Dilley. Remote sensing of high clouds IV: Observed temperature variations in cirrus optical properties. *Journal of the Atmospheric Sciences*, 38:1069-1082, 1981.
- G. Salvetti. Spaceborne doppler wind lidars. *ESA Journal*, 11-12:19-36, 1987.
- J. G. Sela. Spectral modeling at the National Meteorological Center. *Monthly Weather Review*, 108:1279-1292, 1980.
- Y. Takano and K. N. Liou. Solar radiative transfer in cirrus clouds. part 1: Single-scattering and optical properties of hexagonal ice crystals. *Journal of the Atmospheric Sciences*, 46:3-19, 1989.
- M. Tiedtke, J.-F. Geleyn, A. Hollingsworth, and J.-F. Louis. ECMWF model parameterisation of subgrid scale processes. Technical Report 10. ECMWF, Reading, U.K., 1979.
- S. G. Warren. Optical constants of ice from the ultraviolet to the microwave. *Applied Optics*, 23:1206-1225, 1984.
- G. E. Woodbury and M. P. McCormick. Zonal and geographical distributions of cirrus clouds determined from SAGE data. *Journal of Geophysical Research*, 91:2775-2785, 1986.